Assessing and Correcting Bias in Gridded Reference Evapotranspiration over Agricultural Lands Across the Contiguous United States

John M. Volk [a1], Christian Dunkerly [a], Sayantan Majumdar [a], Justin L. Huntington [a], Blake A. Minor [a], Yeonuk Kim [a], Charles G. Morton [a], Peter ReVelle [a], Ayse Kilic [b], Forrest Melton [c], Richard G. Allen [e], Christopher Pearson [a], Adam J. Purdy [c, d], Todd G. Caldwell [a]

[a] Desert Research Institute, Reno, NV, USA
[b] University of Nebraska-Lincoln, Lincoln, NE, USA
[c] NASA Ames Research Center, Moffett Field, CA, USA
[d] California State University, Monterey Bay, Seaside, CA, USA
[e] (ret) University of Idaho, Kimberly, ID, USA

Abstract

Gridded reference evapotranspiration (ETo) data are widely used for agricultural water management and remote sensing ET (RSET) models, but biases can arise in agricultural regions where coarse-resolution meteorological inputs fail to capture local microclimates. We investigated biases in the gridMET ETo product across irrigated agricultural areas of the contiguous United States (CONUS) by comparing gridMET values with ETo calculated from 793 agricultural weather stations. We also used these stations to bias correct monthly gridMET ETo. Results show that gridMET systematically overestimates ETo by 10–20% at most cropland sites, while pockets of underestimation appear in some arid western regions, primarily due to wind speed bias. Overestimation of wind speed was the dominant driver of ETo bias, amplified by positive biases in solar radiation and maximum air temperature and negative biases in humidity (vapor pressure), whereas minimum temperature bias had a smaller effect. Regionally, the relative influence of these drivers varied: in some arid western climates, ETo bias was most closely linked to humidity and temperature errors, while in many other regions, including much of the eastern and coastal regions, wind speed and solar radiation biases were the dominant drivers. Comparison with 79 independent eddy covariance sites showed that the bias correction substantially improved monthly gridMET ETo accuracy at most of these stations. For example, the mean absolute error (MAE) in ETo was reduced at 80% of cropland sites across the CONUS. The bias-corrected ETo also improved accuracy in the three ETo-dependent OpenET RSET models (eeMETRIC, SIMS, and SSEBop), reducing MAE at 47–67% of cropland sites. Moreover, at the cropland eddy covariance stations, monthly mean bias error (MBE) of the three RSET models decreased by up to 9.5 mm/month (equivalent to 10% of the mean monthly eddy covariance ET), MAE was reduced by 1.7–3.5 mm/month, and root mean square error (RMSE) was reduced by 2.6–4.2 mm/month; though the OpenET ensemble accuracy metrics changed minimally overall. Across natural land cover types including forests, wetlands, grasslands, and shrublands, MAE and RMSE also improved for all RSET models. Our findings underscore the need to account for bias in gridded ETo data, which can arise from

[1] Corresponding author at: Division of Hydrologic Sciences, Desert Research Institute, 2215 Raggio Parkway, Reno, Nevada 89512-1095, USA
Email address: john.volk@dri.edu (John M. Volk)

multiple factors in the underlying gridded meteorological data inputs and methods that we explore and discuss. We also discuss potential solutions, including alternative datasets and approaches for calculating ETo that could better capture climate conditions over irrigated land, and alternatives to the direct utilization of gridded ETo in water-limited regions for RSET modeling. Incorporating bias corrections for gridded ETo can reduce uncertainty in applications that directly use ETo and improve the reliability of RSET models and other water resource applications that depend on gridded ETo data.

Keywords: reference evapotranspiration (ETo), bias correction, irrigation, croplands, eddy covariance, remote sensing ET

Graphical Abstract

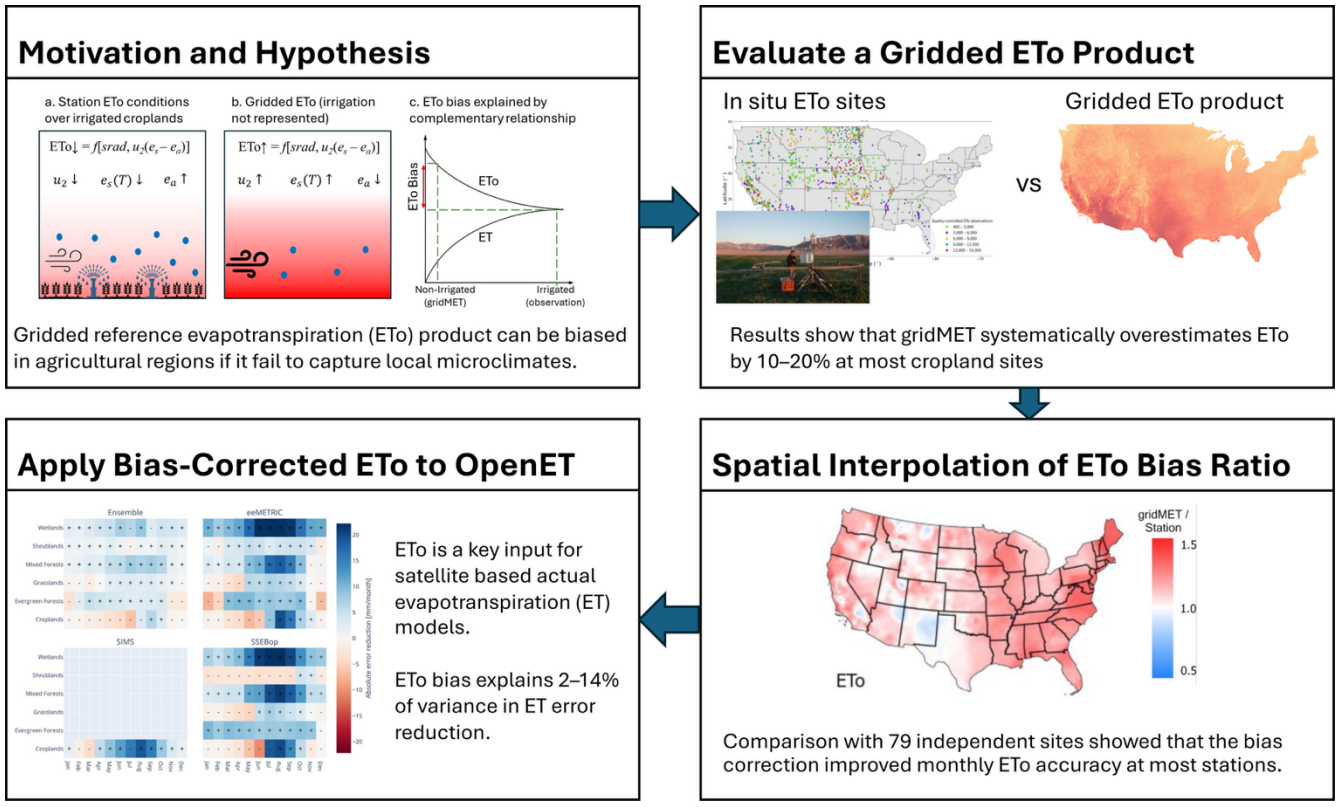

Highlights

- gridMET reference evapotranspiration (ETo) is overestimated at agricultural stations.
- Bias is driven by wind (+17%), srad (+5%), ea (−7%), and T errors (~+0.3°C).
- Primary bias drivers vary from the arid Western United States to the humid East.
- We develop monthly spatial bias-correction surfaces for gridMET ETo across CONUS.
- Corrected ETo improves OpenET remote-sensing ET performance across land covers.

1. INTRODUCTION

Evapotranspiration (ET) constitutes the largest fraction of the outgoing water balance, making it a critical variable for energy and carbon cycling, hydrologic and atmospheric studies, and water resource

management. Although *in situ* ET measurements are not widely available, reference ET (ETo) formulations based on a well-watered reference crop (typically grass or alfalfa) have been developed and are commonly used with meteorological and plant phenology data (i.e., crop coefficients) to estimate ET rates (Allen et al., 1998). Advancements in meteorological and geospatial modeling have led to the transition from using *in situ* weather station to gridded data for calculating ETo and phenology variables (e.g., growing degree days, emergence, killing frost) at local and regional scales (e.g., Hobbins et al., 2023, Abatzoglou, 2013; Kiefer et al., 2016; Lewis and Allen, 2017). Spatially complete and temporally consistent ETo datasets are essential for satellite remote sensing of ET (RSET) (Melton et al., 2022; Volk et al., 2024; Ott et al., 2024) and for quantifying irrigation water use and water requirements at regional to national scales (Allen et al., 2020; Martin et al., 2025). For instance, several RSET models calculate the fraction of reference ET (EToF, where EToF = ET / ETo) and require temporally complete ETo data to calculate time-integrated actual ET (Melton et al., 2022). Therefore, any bias in gridded ETo results in a corresponding bias of RSET model bias making it important to assess and bias correct gridded ETo (Hobbins and Huntington, 2016; Allen et al., 2021).

Previous studies suggest that gridded ETo datasets tend to overestimate *in situ* weather station ETo (Martins et al., 2017; Paredes et al., 2018), especially in agricultural areas (Abatzoglou, 2013; Huntington et al., 2015; Blankenau, 2020; Lewis & Allen, 2017; Allen et al., 2021). Variables used to calculate ETo include air temperature, solar radiation, vapor pressure, and wind speed, and are often biased to varying degrees depending on the region and environmental conditions. Higher biases have been observed in gridded atmospheric reanalysis products within agricultural areas, such as the North American Land Data Assimilation System (NLDAS-2; Xia et al., 2012), compared to products that rely more directly on weather station observations like the Parameter-elevation Regressions on Independent Slopes Model (PRISM) (Daly et al., 2008; Abatzoglou, 2013; Walton & Hall, 2018; Blankenau et al., 2020). This is likely because reanalysis products blend model output with observations from stations located outside agricultural areas.

In irrigated agricultural regions, the air tends to be cooler and more humid than the surrounding environment given that a larger fraction of available energy is partitioned into latent heat flux rather than sensible heat (Morton, 1994; Allen et al., 2021). The cooler and more humid conditions created by irrigation, enhanced soil moisture, and relatively high ET are generally not represented in coarse meteorological fields used to drive NLDAS-2, such as in the North American Regional Reanalysis (NARR) (Mesinger et al., 2006). Gridded datasets can also overestimate wind speed due to underrepresenting the effects of crop surface roughness and increased atmospheric stability over cooler irrigated surfaces, both of which reduce vertical momentum mixing and lead to slightly lower near-surface winds (Lunel et al., 2024; Phillips et al., 2022).

Outside irrigated regions, a different set of factors likely contribute to ETo bias, making it difficult to separate the influence of individual sources, particularly in regions of heterogenous land cover. For example, the assimilation of observational data from locations such as airports and developed areas, which are typically warmer and drier due to urban heat island effects, as well as the simplified representation of terrain and land surface processes in the forcing data and coupled atmospheric-land surface models (Blankenau et al., 2020; Ménard, 2010; Mesinger et al., 2006). Limitations in the

representation of subgrid hydrology and lateral water redistribution, and measurement and simulation of local weather in complex topography can also be important sources of bias in non-agricultural areas (McEvoy et al., 2014; Fan et al., 2019).

While multiple factors affect ETo bias across all land covers, this study focuses on bias within agricultural areas where evaporative cooling contrasts between local and regional conditions are marked, with the goal of understanding and correcting ETo bias to improve field-scale RSET predictions of ET within agricultural areas—specifically the OpenET ensemble of models (Melton et al., 2022). Given the limited representation of agricultural weather conditions in numerous gridded weather datasets, we hypothesize systematic positive bias in gridded ETo across the CONUS when compared to agricultural weather station ETo, especially within irrigated areas. Figure 1 illustrates this hypothesis and provides a conceptual framework for the study by contrasting conditions with and without irrigation, and panel (c) links the resulting bias to the complementary relationship (CR) of evaporation, which states that when the land surface becomes water-limited, actual ET decreases while potential (or reference) ET increases by an equal amount due to an increase in sensible heat and drying power of the air (Bouchet, 1963; Hobbins and Huntington, 2016).

OpenET relies on gridMET grass (short) reference ETo data as a key input for the majority of RSET models within the OpenET ensemble. The gridMET dataset is a 4 km resolution daily gridded meteorological dataset that covers the contiguous United States (CONUS) starting from 1979 and is generated by combining daily and monthly 4 km ($1/24^{th}$ degree) PRISM with daily 12 km NLDAS-2 data (Abatzoglou, 2013; Xia et al., 2012; Daly et al., 2008). gridMET near-surface air temperature is derived from PRISM while solar radiation, specific humidity, and wind speed are derived from NLDAS-2. gridMET ETo is used within OpenET RSET models after bias correction following the approach, methods, and datasets described in this study.

OpenET's high-resolution ET products (30 m, daily and monthly) are accurate in agricultural regions (Volk et al., 2024; Knipper et al., 2024) and are widely used for water resources research and applications (e.g., Ott et al., 2024, Martin et al., 2025). However, ETo biases still affect RSET model accuracy, especially in water-limited areas. Identifying and quantifying individual sources of error, whether from model structure or from forcing data such as gridded meteorological datasets, is essential for understanding and reducing uncertainty and guiding future model refinements (Volk et al., 2024; Melton et al., 2022).

The objective of this study was to assess bias in gridMET ETo data, and to evaluate the effectiveness of ETo bias correction on the accuracy of OpenET RSET predictions. Specifically, we ask the following key questions:

1) How does bias in gridMET ETo vary across different regions and what are the relative contributions due to biases in solar radiation, wind speed, humidity, and air temperature?
2) How well does bias-corrected ETo perform against independent station-based ETo?
3) How does the correction of gridMET ETo bias influence the accuracy of OpenET when compared to *in situ* micrometeorological station ET data?

To address these questions, we make direct comparisons between gridMET ETo to well-curated station-based datasets from 793 weather stations located in agricultural areas (Dunkerly et al., 2024; 2026) and 79 micrometeorological flux stations (Volk et al., 2023a,b) distributed across the CONUS. Station-based ETo bias assessment allowed for spatial mapping of bias and the development of bias correction surfaces for the purpose of reducing uncertainty in ET modeling. More accurate and representative gridded ETo data will ultimately improve evaluations of agriculture water consumption (Goble et al., 2021), land surface model representation of agriculture (Sabino et al., 2024), and RSET model products (Blankenau et al., 2020; Moorhead et al., 2015). The following sections describe relevant datasets, methods, and results of the gridMET bias and correction assessment.

2. DATA AND METHODS

The following summarizes processing steps, methods, and data used in this study:

1) Collection of weather station data and quality control (QC) of solar radiation, air temperature, humidity, and wind speed (components of ETo);
2) Calculation of station daily ETo using QC-processed station data and the American Society of Civil Engineers (ASCE) Standardized Penman-Monteith equation for short (grass) vegetation (Allen et al., 2005);
3) Calculation of monthly long-term station-to-gridMET bias of ETo and component variables;
4) Spatial interpolation of monthly bias results over the CONUS and correction of gridMET ETo bias;
5) Comparison of spatially interpolated bias-corrected and uncorrected gridMET ETo with an independent ETo dataset developed using micrometeorological station measurements in agricultural areas;
6) Evaluation of OpenET RSET model accuracy using uncorrected and corrected gridMET ETo as model inputs.

This study focuses on grass reference ETo as it is used by OpenET RSET models; however, analogous results of alfalfa (tall) reference ET (ETr) (Allen et al., 2005) bias are summarized by region and climate zones in supplementary material. Intermediate products, including interactive intercomparison graphs and monthly bias correction surfaces were produced and visualized during the processing steps listed above using open-source software, and all the data are public as described below.

2.1 Weather station data

Weather data for calculating ETo were collected from 1,078 stations across multiple networks, and all stations were located in agricultural areas (Table 1). Datasets included all records available through 2020 (Dunkerly et al., 2026). The initial set of 1,078 weather stations was reduced to 793 after screening and QC described below.

Table 1. Network information for agricultural weather stations used in this study.

Network	Number of Stations	Total ETo Observations (days)	Website	Access Date (yyyy-mm-dd)
Agrimet, Columbia-Pacific Northwest Region	87	516,870	https://www.usbr.gov/pn/agrimet/	2021-01-10
Agrimet, Missouri Basin Region	25	136,313	https://www.usbr.gov/gp/agrimet/	2020-02-14
AZMET	25	131,725	https://cals.arizona.edu/azmet/	2021-01-15
CIMIS	138	753,852	https://cimis.water.ca.gov/	2019-06-10
CoAgMET	68	296,712	https://coagmet.colostate.edu/	2021-01-09
GAEMN	19	111,905	http://www.georgiaweather.net/	2020-04-17
High Plains Regional Climate Center	216	1,320,191	https://hprcc.unl.edu/	2020-07-10
Missouri Mesonet	31	159,757	http://agebb.missouri.edu/weather/stations/	2020-02-27
NICE NET	13	35,312	https://nicenet.dri.edu/	2019-05-10
Oklahoma Mesonet	56	388,416	http://mesonet.org/	2019-10-17
SCAN	47	146,759	https://www.wcc.nrcs.usda.gov/scan/	2021-04-17
USCRN	22	56,145	https://www.ncdc.noaa.gov/crn/	2020-03-20
WACNet	14	34,333	http://www.wrds.uwyo.edu/WACNet/WACNet.html	2021-01-10
Other[†]	32	103,518	N/A	2021-01-20
Grand Total	793	4,191,808		

[†]Includes data from the Enviroweather, Florida Automated Weather Network, Utah Climate Center, United States Department of Agriculture, West Texas Mesonet, Western Regional Climate Center, and ZiaMET networks.

The distribution of agricultural weather stations and their assessed quality (Dunkerly et al., 2026) are shown in Figure 2. Station data were identified and obtained across major agricultural regions and stations verified to be condition for ETo (Allen et al., 2021). Regions with relatively low agricultural activity, such as northern Arizona and New Mexico, generally had fewer agriculture stations. The Eastern U.S. generally had a lower number of agricultural stations (and a major reason for this was that the development of the dataset aligned with the timeline and goals of the OpenET Phase I project that focused on the Western U.S. (Dunkerly et al., 2026; Melton et al., 2022). Other spatial patterns underscore the need for additional agricultural weather stations in regions with sparse coverage along

with more uniform distribution across political boundaries for improved representation of regional agricultural weather.

2.1.1 Weather station data processing and quality control

Weather station data (Table 1) underwent a multi-stage QC process prior to calculating ETo. First, stations were screened on data availability, requiring at least two continuous years of growing season (April-October) records for air temperature, solar radiation, wind speed, and humidity. *In situ* wind measurements were adjusted to 2 m using a logarithmic vertical wind profile (Dunkerly et al., 2024; Allen et al., 2005). Next, each station's location and surrounding environment were visually inspected using aerial and satellite imagery, land use and land cover, and terrain data to ensure the station was located in representative well-watered agricultural conditions and consistent with intended application of the ASCE standardized ETo equation (Allen et al., 2025). This led to removal of 290 sites influenced by non-agricultural, non-ideal grass-reference ETo conditions. Data from remaining agriculture weather stations were processed using the agweather-qaqc Python package (Dunkerly et al., 2024), which applies automated algorithms to flag, remove, or correct outliers and erroneous values. A final manual inspection of each time series identified any remaining discrepancies. This rigorous procedure (see Dunkerly et al., 2026 for details) resulted in high-quality curated agriculture weather datasets from 793 stations with a total of 11,484 years (4,191,808 days) for the calculation of daily ETo using agweather-qaqc (Dunkerly et al., 2024).

2.2 Relative bias calculations

Weather station-gridMET pairing and calculations described above were performed using the gridwxcomp open-source Python package (Volk et al., 2025), which was designed to evaluate and spatially interpolate biases between station and gridded weather data. The Python package performs the necessary temporal and spatial pairing of station data to gridded data and automates download of gridded data, bias calculation, and statistical calculations, allowing for consistent and reproducible results across large sample datasets.

For each QC agriculture weather station, the daily time series at each collocated gridMET cell was aligned in time. Paired data were first filtered so that only months where both station and gridded ETo contained at least ten days of paired data were retained. Next, for each month, station data and gridded data were aggregated using all data on record (e.g., all data recorded for each month were summed or averaged over all years on record), and the ratio or difference of station to gridMET was calculated using the summed or average values for each variable. Summed values and ratios were calculated for solar radiation, vapor pressure, wind speed, and ETo, and average values and differences were calculated for temperature (i.e., ratio of sums and difference of averages). The interannual variability of relative bias (gridMET/station) and differences was calculated from the standard deviation and the coefficient of variation of the annual ratios and differences for each month. Ratios and differences were also calculated for growing season (AMJJASO), summer (JJA), and annual periods assuming data minimums of 65, 35, and 125 days per year required for each period, respectively. Additional details and bias equations are in Appendix B.

Correlation between ETo bias and individual meteorological variable bias was conducted to assess potential sources of ETo bias. The influence of the surrounding irrigated agricultural land fraction (or irrigation fraction) was calculated within a 1500 m buffer (Huntington & Allen, 2009) around each station based on two publicly available 30 m spatial resolution irrigation status datasets accessed and processed via Google Earth Engine (Gorelick et al., 2017; Roy et al., 2025). These data sets included IrrMapper (Ketchum et al., 2020; 2023) and LANID (Xie et al., 2019; 2021; Martin et al., 2025). Irrigation fractions within each station-buffer were calculated by dividing total irrigated cropland area by the buffer area, using the most frequent IrrMapper and LANID class (i.e., '0' for non-irrigated and '1' for irrigated) over the station's period of record. We then defined three irrigation classes, low (< 25%), medium (25%-75%), high (> 75%), and attributed the stations as either irrigated (irrigation fraction > 0) or non-irrigated (irrigation fraction = 0). See Supplementary Discussion 1 for further details.

2.3 Spatial interpolation

Biases (i.e., ratios and differences) in gridMET ETo and forcing variables at weather station locations were spatially interpolated using a parametric kriging approach. Average monthly, seasonal, and annual point bias data were reprojected into the Lambert Conformal Conic coordinate reference system (ESRI:102004); this reference system has minimal distortion and is preferred for large regions that span CONUS east-to-west, particularly those in mid-latitudes (Jiang & Li, 2014). The kriging interpolation employed an exponential "stable" semi-variogram model with parameters fit to station ETo point biases for each month. The parameters included lag size, major range, and partial sill, which were determined to reflect the distances over which most spatial correlation occurred (approximately 70 km). The interpolation process divided the area around each station into four sectors, separated by 45-degree angles starting from north, and sampled a minimum of 10 and a maximum of 20 data points from each sector. The final surfaces were smoothed using minor (3x3 pixels at a 4 km resolution) and major (20x20 pixels) focal windows and then blended using spatially derived weights to address regional variability. After spatial interpolation, bias surfaces were bilinearly resampled to the gridMET grid and native WGS 84 coordinate reference system allowing for spatially consistent corrections of gridMET data. Average monthly bias surfaces were used to correct gridMET ETo (i.e., gridMET ETo / bias factors) at both daily and monthly time steps for respective months across the entire record from 1979 to present.

2.4 ETo validation data

An independent dataset developed from high-quality micrometeorological eddy covariance measurements (Volk et al., 2023a,b) was used to validate bias-corrected gridMET ETo results. The dataset includes measurements from 79 eddy covariance stations, 30 located in irrigated agricultural with a mix of perennial and annual crop types such as alfalfa, grass hay, nuts, wheat, soy, corn, and others. Site metadata is provided in Supplementary Table 1. Methods for calculating ETo using micrometeorological data followed the same approach of agweather-qaqc, which uses the daily formulation of the ASCE Standardized Penman-Monteith reference ET equation; including the use of

incoming shortwave radiation (as opposed to net radiation), and a logarithmic adjustment to wind measurements to a height of 2 m (Allen et al., 2005).

2.5 Remote sensing ET data and accuracy assessment

OpenET is an online platform for mapping RSET from six models including the Google Earth Engine implementation of the Mapping Evapotranspiration at high Resolution with Internalized Calibration (eeMETRIC; Allen et al., 2007), the Satellite Irrigation Management Support (SIMS; Pereira et al., 2020; Melton et al., 2012), the Operational Simplified Surface Energy Balance (SSEBop; Senay et al., 2023), the Google Earth Engine implementation of the Surface Energy Balance Algorithm for Land (geeSEBAL; Laipelt et al., 2021), the Priestley-Taylor Jet Propulsion Laboratory (PT-JPL; Fisher et al., 2008), and the Disaggregation of the Atmosphere-Land Exchange Inverse (DisALEXI; Anderson et al., 2018). Three of the six OpenET RSET models, eeMETRIC, SIMS, and SSEBop, use ETo as a scaling flux for daily ET on Landsat satellite overpass days (approximately every 8 days) as the product of ETof (direct model output) and bias-corrected ETo. Two of these models, geeSEBAL and PT-JPL, directly estimate RSET on satellite overpass days and calculate ETof as the ratio of ET and bias-corrected ETo. All these models linearly interpolate ETof between overpass days using the direct estimate of ETof (eeMETRIC, SIMS, and SSEBop) or calculated ETof (PT-JPL and geeSEBAL). Interpolated daily ETof values are then multiplied by bias-corrected ETo to calculate daily. Because PT-JPL and geeSEBAL use bias-corrected ETo for calculating daily and interpolated ETof, bias correction of ETo does not affect monthly ET totals. The sixth model, DisALEXI, directly outputs RSET on days of satellite overpass, but uses solar radiation instead of ETo and ETof for time integration, therefore it was not assessed in this study.

We compared OpenET RSET data, with and without correcting for bias in gridMET ETo, to a CONUS-wide benchmark eddy covariance ET dataset of 140 stations (Volk et al., 2024; Volk et al., 2023a). For reproducibility and interpretability of results, we applied the same methods and data used to previously evaluate the accuracy of OpenET data; specifically, those used in the Phase II Intercomparison and Accuracy Assessment described in Volk et al. (2024). The one difference in this assessment is the use of bias-corrected gridMET ETo for all locations, whereas in Volk et al. (2024) Spatial CIMIS ETo data is used in the state of California and bias-corrected gridMET ETo is used in all other states. Detailed processing steps, methods, and data sources for OpenET-eddy covariance intercomparisons are described in Volk et al. (2024), however, a brief outline is provided here as follows: post-processing and energy balance closure correction of eddy covariance data; development of flux footprints for sampling RSET data at the eddy covariance stations; pairing of RSET with eddy covariance ET; and calculation of accuracy statistics using the eddy covariance ET and RSET data. Our statistical analysis includes the regression coefficient (Slope) with a zero intercept as a measure of bias, mean bias error (MBE), mean absolute error (MAE), root-mean-square error (RMSE) and the coefficient of determination (r^2). See Appendix C for full details of error metrics. Statistical results were grouped by land cover class at each eddy covariance site. The weighted average (weighted by the square root of paired observations) of MBE, MAE, and RMSE was calculated for each land cover type (Obrecht, 2019) to limit the tendency of sites with relatively low or high numbers of paired observations to skew grouped statistics and for consistency with the previous OpenET assessments.

3. RESULTS

3.1 Regional and seasonal relative biases

Overall, we found that gridMET ETo has a positive relative bias to agricultural weather station measurements across the CONUS. Mean annual bias in the Eastern U.S. show higher homogeneity with an overestimation of gridMET ETo that is typically around 5–16% of measured ETo with a mean value of 11% and a standard deviation of 8% across all stations (Figure 3 and Supplementary Table 2). The overestimation was slightly higher in the Eastern U.S. compared to the West, with a mean bias of 13% and 9% respectively. The humid subtropical region in the Southeast and the mediterranean climate region near the West Coast showed the highest overestimation in gridMET ETo. In the arid and semi-arid Western U.S. there is heterogeneity in the station bias and in some regions, such as the Colorado River Basin, the Four Corners region, and patches in Montana and California, there are areas of ETo underestimation (Figure 4).

Seasonally, biases tended to be highest, in terms of magnitude (whether positive or negative) in the colder months of October through February (Supplementary Figure 1). However, for the individual forcing variables of ETo, the seasonal variation differs: e.g., temperature biases tend to be highest in the warmer months. Interannual variability in ETo bias ratio was also calculated using the coefficient of variation at each weather station and spatially interpolated (Supplementary Figure 2). We see a similar trend with higher variability (coefficient of variation up to 0.3) in the colder season and in northern latitudes. However, we found little interannual variability in ETo bias in most of the CONUS during the warmer season with coefficients of variation near zero. This has important (and promising) implications for the application of static monthly bias correction surfaces for correcting the entire period of record of gridMET ETo data.

We hypothesize that gridMET ETo bias is influenced by the fraction of irrigated agricultural land within each 4 km pixel, with higher biases expected in less dense irrigated agricultural areas due to the gridded product's inability to resolve evaporative cooling effects, such as those caused by irrigation in the Western U.S (Figure 1). A rudimentary analysis through boxplot distributions of the ETo bias ratios grouped by irrigation fractions (derived from IrrMapper and LANID) supports this hypothesis in general (see Supplementary Discussion 1). However, the fundamental assumption here is that the agricultural weather stations used in this analysis (Figure 2) are also included in the gridMET product (i.e., PRISM and NLDAS-2 data). Detailed site-specific assessments and verifying whether individual stations have been included in the gridMET product are beyond the scope of this manuscript as these are not readily available. Still, when compared to the ETo from independent micrometeorological (eddy covariance) flux stations not used in the bias corrected gridMET product (Supplementary Table 1A), we observe strong reductions in gridMET ETo bias over croplands (both irrigated and non-irrigated), thereby supporting our hypothesis (see Sections 3.2 and 3.3.1 for details).

3.1.1 Bias in forcing variables

The variables that determine ETo, based on the standardized ASCE Penman-Monteith formulation, are air temperature (minimum: Tmin and maximum: Tmax), wind speed (u2), incoming shortwave solar

radiation (srad), and humidity (Allen et al., 2005). The bias in gridMET ETo arises from biases in these variables. Therefore, we quantified the bias of each variable and conducted a correlation analysis to identify which variables are most influential in driving ETo bias (Supplementary Figure 3). We found that relationships between each variable's respective bias and its relation to ETo bias at the weather stations varied regionally and seasonally; however, clear patterns were also identified.

Wind speed bias exhibited the strongest influence on ETo bias (Figure 4), with widespread overestimation in gridMET data leading to significant positive ETo bias, particularly in the Central and Eastern U.S. The mean annual gridMET wind speed bias for all sites was 1.17 (17% higher than *in situ* measured wind). The mediterranean (West Coast region) and humid subtropical region (Southeast) showed the highest bias and higher variability (mean biases 1.36 and 1.28 respectively). Arid regions showed lower biases around 1.1 with lower variability among stations (Supplementary Table 2). Although the seasonal variability in wind speed bias is substantial, generally the east and far western regions have bias up to 1.5 times the measured wind (and higher at individual stations), and in the Central U.S. there are regions where gridMET is roughly half of the measured wind (Figure 4 and Supplementary Figure 4). Wind biases were found to be highest from July through October, and variability among sites tended to be higher than other variables with standard deviations of the bias ratio typically around 0.3.

Overestimated solar radiation further contributed to the ETo positive bias, as increased available energy directly enhances atmospheric demand (Albano et al., 2022; Kukal et al., 2024). Overall, gridMET solar radiation had a mean overestimation of 1.05 (5%) and a standard deviation of 0.04. The spatial variability in solar radiation bias was also less (i.e., more homogeneous) than other variables, with overestimation in most regions with exception of the intermountain arid West (Figure 4). The radiation bias increased in October–January, particularly in the Northeast, the Great Lakes region, and the Pacific Northwest (Supplementary Figure 5).

Conversely to wind speed and solar radiation, gridMET vapor pressure (ea) was generally underestimated compared to the agricultural weather stations, especially in the Western U.S. Underestimation of vapor pressure also acts to increase ETo bias through increased atmospheric demand. The average bias of vapor pressure was 0.93 or 7% underestimation, with a standard deviation of 0.06 (Supplementary Table 2). The Western U.S. showed more underestimation particularly in the arid Southwest, whereas the Great Lakes and New England regions showed the least bias in vapor pressure. However, there are seasonal shifts in the vapor pressure bias; for example, in most of the Eastern U.S. and some other areas, there was an increase in vapor pressure bias during the growing season months of April–October with positive (overestimation) bias values recorded (Supplementary Figure 6).

Biases were present for both minimum and maximum air temperature (Tmin and Tmax). Although biases in Tmin were slightly higher than Tmax, Tmax tended to show more correlation with ETo bias (Figure 4 and Supplementary Figure 3). The average annual bias for all stations was 0.26 and 0.33 °C for Tmax and Tmin, respectively with standard deviations of 0.57 and 0.91 °C. Arid and semi-arid desert regions in the Western U.S. showed the highest biases, where overestimation was 0.5 and 1.6 °C

for Tmax and Tmin, respectively. Maximum and minimum air temperature biases showed different spatial patterns: Tmax tended to be overestimated more widely across the CONUS except for areas in the Pacific Northwest, and central regions around the Upper Colorado River Basin and south through Western Texas where Tmax was slightly underestimated relative to station measurements (Figure 4). On the other hand, Tmin was overestimated in much of the arid Southwest and Central Intermountain West and slightly in the East Coast and New England region, however, it was underestimated in much of the humid regions of the CONUS in the East where Tmax was overestimated. Seasonally, there was also a clear pattern of increased overestimation of Tmax and Tmin during warmer months (Supplementary Figures 7 and 8).

Collectively, results suggest that ETo overestimation in gridMET is primarily driven by biases in wind speed and solar radiation, with temperature and humidity playing a secondary but important role in modulating the spatial patterns of bias (Figure 4).

3.2 Validation of ETo bias correction and spatial interpolation

We compared the bias-corrected gridMET ETo monthly data at point locations to an independent *in situ* dataset of ETo based on 79 eddy covariance systems and found that overall, the bias correction greatly improved the gridMET ETo data with respect to the independent dataset (Figure 5). These sites covered different land covers, including croplands, evergreen forests, grasslands, mixed forests, shrublands, and wetland/riparian regions. We found that the bias correction improved the r^2 from 0.88 to 0.90, MAE from 26.95 mm/month to 16.62 mm/month (~38% reduction), and MBE from -26.15 mm/month to -12.57 mm/month, using all measured ETo data across all sites.

The largest improvements in reducing gridMET ETo overestimation due to bias correction were observed in the Eastern U.S. (distinguished by the 100th meridian), where ETo bias is greatest due to significant biases in wind speed and solar radiation (Figure 4). Cropland sites showed some of the largest adjustments whereas dryland sites (grasslands and shrublands) showed less of a change (Supplementary Figure 9). Supplementary Figures 10 (all land covers) and 11 (croplands) show the monthly uncorrected and bias-corrected ETo as scatter plots and suggest that MAE and MBE substantially improve across all months. The r^2 also improves for most months, slightly reducing in June and July for all land covers. The largest improvements (> 60% MBE reductions in some cases) occur in the warmer months between April and September when ETo is higher.

3.3 ETo bias correction influence on remote sensing ET accuracy

In addition to evaluating bias in gridMET ETo, we assessed how bias-corrected ETo affects the accuracy of OpenET RSET models relative to eddy covariance ET. Overall, ETo bias correction reduced magnitude errors (MAE, RMSE) and systematic bias (MBE, regression slope) across all land-cover types, while producing only negligible changes in explained variance (r^2). This is consistent with ETo acting primarily as a scalar input to those models that use it (eeMETRIC, SIMS, SSEBop). Changes for the OpenET ensemble were muted, likely because the ensemble includes three models whose monthly ET values are not affected by ETo bias correction and because the outlier removal

approach used by OpenET may be excluding up to two models from the ensemble value, including those that did improve due to ETo bias correction.

3.3.1 Croplands

Overall, ETo bias correction improved both the gridMET ETo and RSET compared to ground measurements. Monthly ETo was improved, due to bias correction, at 29 of the 30 (~97%) cropland sites considering r^2, MAE, and MBE (Supplementary Figure 12a) and their combinations. MAE showed the best improvements across 24 of the 30, i.e., 80% of the cropland sites, followed by r^2 (15 sites, i.e., at 50% sites), and MBE (3 sites, i.e., at 10% sites). Although the OpenET ensemble and individual ET models that depend on ETo (eeMETRIC, SSEBop, SIMS) showed varied site-specific improvements, we observed that the bias-corrected ETo also improved the ET from the OpenET ensemble, eeMETRIC, and SSEBop at 38 (~75%), 44 (~86%), and 41 (~80%) of the 51 cropland sites, respectively (see Supplementary Figures 12b-d). SIMS ET also improved at 41 of the 51 cropland sites (same as SSEBop), however, the number of improved sites differ when considering the individual error metrics (Supplementary Figures 12d-e). Note that the difference in the number of cropland sites for these monthly comparisons is due to the unavailability of required data to calculate ASCE Penman-Monteith ETo across different cropland flux stations (Dunkerly et al., 2026). Here, the number of improved sites include sites where one or more error metrics or their combinations improved, with only five sites showing OpenET ensemble ET improvements for all error metrics (r^2, MBE, and MAE). Additionally, Supplementary Figures 13a and 13b-e show that the ETo and the OpenET ensemble ET estimates improved at 28 (~97%) and 23 (~79%) of the 29 intersecting cropland sites, respectively, in terms of r^2, MAE, MBE, and their combinations, with the eeMETRIC analysis again showing the highest number of improved sites (24 of 29, ~83%), followed by SIMS (23 of 29, ~79%), and SSEBop (21 of 29, ~72%)

Across croplands, the ETo-scaled models (eeMETRIC, SIMS, SSEBop) showed the largest accuracy improvements: MAE decreased by 1.7–3.5 mm/month and RMSE by 2.6–4.2 mm/month, with slope reduced by about 0.1 and MBE by ~9 mm/month (Figure 6 and Table 2). These improvements were most pronounced during the growing season, peaking in JJA and SON, and minimally in DJF (Figures 7 and 8). Despite improvements in the individual models, the OpenET ensemble showed only modest change, likely because the outlier removal algorithm sometimes excludes one or more of these improved models, for example, SIMS was typically excluded ~10% more frequently in croplands compared to the other models in OpenET (Volk et al., 2024).

While the reduction in ETo bias was positively associated with reductions in RSET ET bias across most models (Figure 9), the strength of this relationship was modest. Overall, for monthly data, r^2 values range from 0.02 for the ensemble to 0.14 for SSEBop, indicating that reductions in ETo error account for roughly 2–14 % of the variability in the reduction of RSET ET error on average. In some cases, improved ETo coincided with larger ET errors. This reflects a limitation in models that assume that ET is directly coupled with ETo, an assumption that breaks down under periods of water limitation or reduced atmospheric demand. Modest correlations between ETo and ET error reductions also suggest that a substantial fraction of the variability in RSET ET error is driven by external factors such

as model formulation and other model inputs, including land cover and meteorology (Reitz et al., 2025; Allen et al., 2011).

Table 2. Monthly OpenET Satellite based ET error and bias metrics and improvements that are due to the bias correction of gridMET ETo for models that rely on it. Error metrics are calculated by comparisons with post-processed eddy covariance ET measurements and grouped by general land cover types as described in Volk et al. (2023a; 2024). The change or **Δ** values were calculated as the results with bias correction of ETo as a model minus the results without bias correction of ETo (**Δ** = corrected - uncorrected); i.e., a negative **Δ** signifies a reduction in the metric due to bias correction and a positive **Δ** signifies an increase in the metric. 53 stations with 1671 months of paired model-station data were used for Slope and R^2 whereas a limit of 3 paired months were applied for calculating MBE, MAE, and RMSE √(n) weighted means resulting in 44 sites and 1657 paired months for those metrics, following the methodologies of Volk et al. (2024). Here, MBE, MAE, RMSE, and the corresponding **Δ**s are in mm/month**.**

Model	Slope	MBE	MAE	RMSE	R^2	Δ Slope	Δ MBE	Δ MAE	Δ RMSE	Δ R^2
Ensemble	0.92	–4.97	15.92	20.51	0.90	–0.05	–4.05	0.27	0.00	0.0
eeMETRIC	0.96	–1.99	21.61	27.40	0.82	–0.10	–8.80	–2.14	–3.22	0.01
SSEBop	0.96	–5.69	22.81	28.32	0.85	–0.10	–8.38	–1.61	–2.51	0.01
SIMS	1.00	4.40	18.08	23.12	0.86	–0.10	–9.49	–3.43	–4.12	0.0

3.3.2 Natural land cover types

The improvements in RSET model accuracy from bias correction of gridMET ETo varied considerably by land cover type (Figure 8 and Supplementary Table 3). The strongest improvements in RSET error were found in wetland and riparian sites and forested sites. Mixed results were observed for grassland and shrubland sites, where bias correction led to slight to moderate improvements for some metrics at certain locations but often resulted in negligible changes or slight deterioration in others.

For shrublands, the ensemble, eeMETRIC, and SSEBop all showed improved error metrics. Ensemble RMSE decreased from 21.66 to 20.8 mm/month, and MBE dropped by 1.3 mm/month. SSEBop MBE improved from -0.83 to -4.21 mm/month, and RMSE dropped from 20.29 to 18.33 mm/month. These changes suggest modest but consistent benefits of bias correction for models using ETo in shrubland systems.

For grasslands, ensemble and model improvements were modest. The ensemble RMSE dropped marginally (from 24.04 to 23.49 mm/month), and eeMETRIC showed a 1.8 mm/month reduction in MBE and 1.85 mm/month reduction in RMSE. SSEBop showed similar small gains, with Slope decreasing from 0.84 to 0.75 and MBE dropping from -4.16 to -7.93 mm/month. Overall, model improvements in grasslands were modest due to already low bias, and the ensemble showed minimal net benefit.

Evergreen forests saw relatively more benefit from ETo bias correction. The ensemble MBE decreased by 3 mm/month, and RMSE by 1.8 mm/month. Individual models had larger improvements:

eeMETRIC MBE dropped from 14.9 to 8.8 mm/month, while SSEBop MAE fell from 30.09 to 26.2 mm/month and RMSE from 35.88 to 32.07 mm/month. These error reductions account for ~6–10% of mean monthly ET.

In mixed forests, model improvement was even more pronounced. Ensemble MAE and RMSE both decreased by nearly 5 mm/month. SSEBop RMSE decreased by 11 mm/month, from 38.55 to 27.49 mm/month, and eeMETRIC RMSE fell by 6.6 mm/month (from 31.62 to 25.03 mm/month). Slope and MBE improvements across models indicate a strong reduction in ET overestimation from ETo bias correction. The RMSE reductions for SSEBop and eeMETRIC correspond to 18% and 11% of the mean monthly ET in mixed forests, respectively.

Wetland and riparian ecosystems also showed improvement, especially for eeMETRIC. MAE and RMSE decreased by 12.6 and 13.1 mm/month, respectively (from 44.26 to 32.66 and 51.43 to 38.36 mm/month). SSEBop and SIMS also improved, though less dramatically. The ensemble also benefited, with MAE decreasing by 2.4 mm/month. The reductions in MAE and RMSE for eeMETRIC represent 14–15% of the mean monthly ET in wetland and riparian systems. These error reductions represent a meaningful improvement for wetland ecosystems that are not water-limited.

4. DISCUSSION

4.1 Bias in gridMET ETo and forcing variables

The biases observed in gridMET ETo and its forcing variables are primarily due to the data assimilation techniques, interpolation methods, and input dataset limitations inherent in gridMET's production process (Abatzoglou, 2013; Daly et al., 2008; Bohn et al., 2013; Xia et al., 2012). These biases vary spatially and seasonally. The following sections discuss the key sources of bias associated with each forcing variable that contribute to errors in ETo estimates.

4.1.1 Wind speed

gridMET derives wind speed from NLDAS-2 (Xia et al., 2012), which relies on reanalysis datasets rather than direct station observations (Abatzoglou, 2013). Reanalysis models tend to overestimate wind speeds, particularly in regions with complex terrain where subgrid-scale effects such as surface roughness, vegetation-induced friction, and topographic channeling are not fully resolved (Xia et al., 2012). This overestimation is particularly pronounced in mountainous and forested regions, where local sheltering effects are not captured at the coarse native resolution of NLDAS-2 (~12 km), although, we note that gridMET is downscaled to ~4 km. Given that wind speed plays a crucial role in the aerodynamic term of the ASCE Penman-Monteith equation, higher-than-observed wind speeds lead to inflated ETo estimates.

Overestimation of wind speed in flatter regions and in the eastern U.S. can be attributed to multiple factors beyond subgrid-scale terrain effects. A key factor is how land surface roughness and boundary-layer processes are represented in the NARR reanalysis fields that provide the wind forcing for NLDAS-2 (Xia et al., 2012; Mesinger et al., 2006). Coarse reanalyses smooth out local land cover and

underestimate surface friction, which leads to higher wind speeds (Yu et al., 2015), and differences in boundary-layer parameterizations can also affect vertical mixing and low-level winds (Shen & Du, 2023). Additionally, in the West, irrigation cools and moistens the surface, creating a more stable boundary layer that weakens turbulent mixing, and it also weakens thermally driven circulations (e.g., daytime slope winds) as air flows across the cooler irrigated patches. These processes, documented in field observations (Phillips et al., 2022) and modeling studies (Lunel et al., 2024), are likely underrepresented in coarse reanalysis models, which do not explicitly resolve the fine-scale conditions over agricultural areas.

While the mediterranean (West Coast) and humid subtropical (Southeast) regions showed the highest positive bias in wind speed, the propagation of this bias into ETo bias was reduced in these regions (Figure 3). This is because the sensitivity of ETo to wind speed is generally low under humid conditions due to the lower vapor pressure deficit (VPD) (Hobbins, 2016). In contrast, even small wind speed biases can propagate into substantial ETo bias in dry regions. This explains why ETo underestimation is observed in some arid regions (Southwest) rather than in the Central U.S., even though the negative wind speed bias is more pronounced in the Central U.S. Albano et al. (2022) found greater agreement among gridded datasets of wind speed in the western U.S. than in the eastern U.S.

4.1.2 Solar radiation

gridMET's shortwave solar radiation (srad) product is derived from GOES satellite retrievals and bias-corrected using NLDAS-2 forcing data. While satellite-based radiation estimates provide broad spatial coverage, they often struggle to resolve subgrid-scale cloud variability, leading to positive biases in clear-sky conditions (Bohn et al., 2013).

The overestimation of incoming shortwave radiation in humid regions with frequent convective cloud development can be attributed to the limitations of satellite-based radiation products in capturing rapid cloud dynamics. Satellite sensors, due to their temporal resolution, may miss transient cloud formations and dissipations, leading to an underestimation of cloud cover and, consequently, an overestimation of surface-reaching shortwave radiation. This issue is particularly evident in regions like the Amazon, where shallow and deep convective clouds significantly impact radiation fluxes during both wet and dry periods (Silva Dias et al., 2002). The humid astern U.S. is likely subject to the same processes to a lesser degree. High atmospheric moisture content in these regions attenuates incoming solar radiation through absorption and scattering. However, satellite retrieval algorithms often underestimate this effect, particularly in the lower and middle troposphere, leading to a positive bias in shortwave radiation estimates. Incomplete corrections for water vapor absorption and cloud optical thickness further exacerbate this bias, as excessive atmospheric moisture can significantly reduce surface-reaching radiation (Liang & Yu, 2022).

In arid and semi-arid regions, where cloud cover is limited, other factors contribute to solar radiation biases. Satellite retrievals rely on clear-sky radiative transfer models that may not adequately represent attenuation due to aerosols and water vapor, particularly in dust-prone regions such as the Southwestern U.S. (Ruiz-Arias et al., 2013). If aerosol optical depth (AOD) is underestimated, more solar radiation is assumed to reach the surface than actually does, leading to a systematic

overestimation of srad. Despite these widespread positive biases, some locations in the Intermountain West show lower or even negative biases, likely because gridMET srad is not adjusted for topographic effects. In addition, local terrain influences on cloud persistence and shading effects are not well captured by coarse-resolution satellite and reanalysis models (Xia et al., 2012).

4.1.3 Vapor pressure and humidity

Humidity biases in gridMET largely stem from the interpolation of dew point temperature using the PRISM (Daly et al., 2008). PRISM is primarily designed to interpolate temperature and precipitation; its application to humidity variables can introduce systematic errors, especially in arid and semi-arid regions where station coverage is sparse (Abatzoglou, 2013).

Spatial analysis indicates that underestimation bias in humidity is more pronounced in the Western U.S., similar findings were reported by Albano et al. (2022) for multiple gridded products. Irrigated agriculture fields in the Western U.S. may contribute to this regional pattern of underestimation of humidity and the subsequent overestimation of ETo. Results suggest that humidity biases are further exacerbated in high-elevation regions, where PRISM's lapse rate adjustments for temperature may not adequately capture humidity variations, leading to inconsistencies in vapor pressure estimates (Pierce et al., 2014).

The negative bias in humidity can increase VPD, leading to positive ETo bias. However, the humidity bias was a less important factor in ETo bias than wind speed and radiation biases according to our correlation analysis (Supplementary Figure 3). One reason for this is related to sensitivity. Although humidity bias was particularly pronounced in the dry Western US, the sensitivity of ETo to humidity is generally low in these areas (Hobbins, 2016). This low sensitivity results from the combination of high temperature and low wind speeds (Supplementary Figure 14). Therefore, the impact of humidity bias on ETo in arid regions is smaller than other variables. Nevertheless, the spatial pattern of ETo bias was still strongly influenced by humidity bias (Figure 4).

4.1.3 Air Temperature

Air temperature biases in gridMET arise from the reliance on PRISM interpolation methods, that blend station observations with elevation-based regressions (Daly et al., 2008). While PRISM may capture large-scale temperature gradients, regional biases emerge due to station density limitations, complex terrain effects, and other regional land surface conditions. Our analysis indicates that Tmax tends to be overestimated in arid regions of the Western U.S., while Tmin is generally overestimated in high-elevation areas.

The overestimation of Tmax in arid regions likely stems from PRISM's interpolation not fully capturing the cooling effects of latent heat flux from irrigation. Irrigated croplands experience enhanced evapotranspiration, which lowers daytime temperatures, but station observations in nearby non-irrigated areas may skew the interpolated Tmax higher than actual conditions (Lobell & Bonfils, 2008). Additionally, many temperature stations are located at airports or non-agricultural areas, which

do not fully represent the cooling effects of irrigation, leading to a warm bias in Tmax over irrigated regions.

In high-elevation regions Tmin is overestimated, likely due to PRISM's elevation-based lapse rate assumptions. Tmin in mountain regions is heavily influenced by cold-air drainage, inversions, and local topographic effects, which PRISM's interpolation may smooth out, leading to a warm bias (Daly et al., 2008). The sparse station network in mountainous areas exacerbates this effect, as fewer direct observations force the model to rely more on broad-scale elevation-based adjustments rather than local meteorological effects. Additionally, PRISM's dependence on lowland stations for interpolation may further warm Tmin estimates at high elevations, especially in areas where cold-air pooling is prevalent (e.g., intermountain valleys).

The overestimation of Tmax in well-watered agricultural areas leads to an artificial increase in ETo, reinforcing previous findings that gridded ETo products may exaggerate atmospheric demand in these regions. Similarly, the overestimation of Tmin in high elevations could influence nighttime evaporative processes, though the overall impact on ETo is likely smaller than that of Tmax. Future improvements to gridded temperature datasets should consider incorporating higher-resolution land surface models and refining lapse rate adjustments to better capture local thermal dynamics in complex terrain.

Additionally, the blending of observational data with model-driven data in gridded climate products is a potential source of spatial inconsistency and potential bias in all the forcing variables of ETo. This is particularly true in areas where station density is low or unevenly distributed, resulting in spatially inconsistent corrections (Mesinger et al., 2006).

4.2 RSET accuracy implications

The relationship between ETo error reduction and corresponding changes in RSET ET error varied by model, land cover type, and season, with ETo bias explaining 2–14% (r^2 = 0.02 - 0.14) of the variance in RSET error reduction (Section 3.3). While bias correction of ETo improved RSET ET accuracy overall, these correlations indicate that ETo bias is an important but partial contributor to RSET ET error. The incomplete correspondence between ETo bias reduction and ET bias reduction suggests that additional factors, including RSET model formulation and uncertainty in bias correction methods and data, also play important roles (Allen et al., 2011; Daly, 2006).

From a process standpoint, the degree to which ETo error propagates into ET estimates also depends on the coupling between atmospheric demand and ET. This coupling is strongest when vegetation is unstressed and well-watered, allowing ET to track ETo closely. It weakens in energy-limited conditions (e.g., humid climates, high cloud cover, or periods of high atmospheric humidity) where VPD is low and ET is constrained more by available energy, particularly during calm conditions with limited mixing (Bouchet, 1963; Brutsaert and Parlange, 1998; Szilagyi and Józsa, 2008). Seasonal transitions can further modify the relationship: in humid climates, ETo bias correction may have a strong effect in dry months but little to no effect, or even an opposite effect, in wetter months when the air approaches saturation (Hobbins, 2016). In irrigated or well-watered croplands, increased ET can raise local

humidity during the growing season, further weakening ETo-ET coupling as the season progresses (Pereira et al., 2015).

In true water-limited ecosystems such as arid grasslands and shrublands, vegetation stress often decouples ET from atmospheric demand, weakening the relationship between ETo and actual ET. Under these conditions, models that rely heavily on ETo scaling, such as SSEBop (which uses land surface temperature (LST) to adjust an ETo fraction) and SIMS (which applies a crop coefficient from vegetation indices), tend to overestimate ET because they implicitly assume vegetation can meet potential demand. Performance maps from Reitz et al. (2025) suggest that SSEBop and SIMS may have lower accuracy in natural vegetation of arid regions compared to approaches like PT-JPL (Fisher et al., 2008) and DisALEXI (Anderson et al., 2018), which more explicitly represent water stress. PT-JPL incorporates biophysical constraint functions using VPD, the normalized difference vegetation index, and LST to reduce ET when stomatal closure is likely (Liu et al., 2025), while DisALEXI infers vegetation water stress by linking elevated canopy LST to reduced transpiration within a two-source energy balance model (Anderson et al., 2018).

These patterns have direct implications for operational use of OpenET and other ETo-based data products in irrigation scheduling and water accounting in the arid Western U.S. In well-watered croplands or wetland/riparian zones, where coupling remains strong, ETo bias correction can improve RSET estimates, supporting its use for precision irrigation and seasonal water planning. However, the coupling of ETo and ET may be negative as illustrated by the complementary relationship—where drying of the environment results in increased ETo that corresponds with decreased actual ET (Figure 1; Bouchet, 1963; Brutsaert and Parlange, 1998; Szilagyi and Józsa, 2008). In these cases, the bias reduction in gridded ETo may result in an increase in RSET error, which we found in section 3.3 and Figure 9. For analogous reasons, we found sites and periods of time where ETo error increased (as a result of bias correction) yet corresponding RSET error decreases. Models that scale ET directly from ETo implicitly assume that vegetation can meet potential demand, an assumption that breaks down when soil moisture or reduced atmospheric demand (e.g., low VPD and calm conditions) limits ET (Bouchet, 1963; Brutsaert and Parlange, 1998; Szilagyi and Józsa, 2008). For operational use, this suggests that RSET estimates that depend on gridded ETo would benefit from a customized correction to ETo data that considers local moisture, humidity, and atmospheric conditions, particularly when these estimates are used for regional water balance or policy applications (Volk et al., 2024; Allen et al., 2011).

Across evergreen and mixed forests, where OpenET models often overestimate ET (Khand et al., 2025; Volk et al., 2024), ETo bias correction reduces error more than in other land covers. However, a sizable residual bias remains, indicating additional RSET error sources. Tall forest canopies increase aerodynamic roughness, enhance turbulent mixing, and reduce the LST to air temperature gradient even under water limitation. Therefore, when surface energy balance models misrepresent aerodynamic conductance in dry forests, they can cause significant bias in sensible heat flux estimation (Trebs et al., 2021). In addition, daytime biomass energy storage in dense tall canopies is not negligible but is typically ignored in models. Together, these effects cause forest RSET overestimation, particularly in dry conditions that ETo bias correction alone cannot eliminate.

4.3 Limitations and next steps

Although gridded ETo products like gridMET are widely used in agricultural applications, they remain limited by their coarse resolution and the parameterizations of the reanalysis systems they rely on. For example, land surface models used in NLDAS-2 do not represent agricultural effects (irrigation, crop surface roughness, albedo, crop phenology, etc.) or their feedbacks on the surface energy balance (Xia et al., 2012). This likely contributes to the warm and dry biases we observe in well-watered agricultural regions. However, the large wind speed, humidity, and radiation biases documented in this study are not solely due to water availability (Blankenau et al., 2020). They also reflect broader limitations in reanalysis systems, including terrain smoothing, sparse station coverage, and coarse parameterizations of the surface layer. Wind speed errors, for instance, are especially large in topographically complex areas where channeling and sheltering effects are not resolved. While bias correction can reduce these errors, it does not address their structural or mechanistic origins. Future improvements may require ETo estimates that explicitly incorporate subgrid agricultural-atmospheric feedbacks or, for example, apply machine learning techniques trained on denser observational networks in agricultural landscapes (Jung et al., 2020; Kim et al., 2025).

While ETo bias correction improved RSET accuracy across a range of land covers, the size and timing of the improvement varied in meaningful ways. The largest reductions in RSET error were found in wetlands and forests. In wetlands, ET and ETo are well coupled under wet conditions, and the assumption of potential demand being met generally holds. In forests, however, notable residual bias and error remained even after correction due to other factors not addressed by ETo correction, such as the misrepresentation of canopy turbulence, aerodynamic conductance, and unmodeled heat storage in biomass (Trebs et al., 2021; Khand et al., 2025). Improvements were also observed in croplands during the peak growing season, where reducing ETo bias may have helped mitigate overestimation of atmospheric demand. Models that scale ET estimates directly from ETo, such as SSEBop and SIMS, assume vegetation can meet potential demand, which is not always true. Our analysis cannot isolate this decoupling as the only reason for varying correction effectiveness. Structural model limitations, mixed land cover, and uncertainty in the gridded meteorological inputs (including interpolation uncertainty) also contribute; importantly, this uncertainty can vary substantially across space and time, so average error metrics may not reflect where uncertainty is actually largest (Doherty et al., 2025). These results highlight the importance of improving model sensitivity to environmental stress (Allen et al., 2011; Fisher et al., 2017), and of clearly conveying uncertainty in RSET estimates used for management and decision-making (Volk et al., 2024).

Despite improvements from ETo bias correction, temporal uncertainty (in gridded ETo data) also contributes to RSET uncertainty for models that rely on interpolating between satellite overpasses to generate continuous time series. Several models calculate ETo fractions (EToF) derived from gridded ETo to fill daily gaps. This approach inherits the limitations of the underlying ETo data that we highlight, and the accuracy of time integration depends on both the quality of the interpolation and the frequency of cloud-free observations (Fisher et al., 2017; Alfieri et al., 2017). When long cloud gaps occur, especially during dynamic phases of the growing season, errors in interpolated ET can accumulate and introduce uncertainty into monthly and seasonal estimates. Addressing this issue may

require a combination of strategies, including the use of multiple satellite platforms to reduce revisit intervals, development of alternative gap-filling methods that do not rely solely on EToF, and increased testing of machine learning models that can learn vegetation and climate dynamics more flexibly (Jung et al., 2020; Kim et al., 2025).

5. CONCLUSIONS

This study provides a comprehensive assessment of bias in the gridMET reference evapotranspiration (ETo) dataset across agricultural regions of the United States and demonstrates the benefits of correcting those biases. We found that gridMET ETo is generally overestimated in agricultural areas, often by 10–20%, primarily due to systematic errors in meteorological inputs from PRISM and reanalysis datasets that do not account for the cooling and humidifying effects of irrigation in the Western U.S. or other agricultural conditions. ETo bias varies geographically, with some arid regions showing underestimation due to terrain complexity and interpolation limitations.

Wind speed bias was the dominant contributor to ETo error, followed by biases in solar radiation and vapor pressure. While temperature bias played a smaller role overall, it became more important in hot, dry regions where maximum temperature and humidity interact to influence vapor pressure deficit.

By interpolating station-based ETo data from 793 weather stations (Dunkerly et al., 2026) we created monthly bias-correction maps that, when applied, substantially reduced error in gridMET ETo across diverse climates and regions of the U.S. This was evaluated using an independent set of observations from 79 eddy flux towers, including 30 located over agricultural areas. These findings have important implications for satellite-based remote sensing ET models (including several in the OpenET platform) that use gridded ETo as a key input for estimating overpass ET and for temporal integration. If left uncorrected, the positive bias in gridMET ETo can propagate through to overestimate actual ET in irrigated croplands and in natural land covers. The seasonality in the bias can also distort the water use signal, with implications for irrigation management and water resource management.

We found that applying spatially complete bias corrections to gridded ETo improved the accuracy of OpenET's monthly ET estimates at most eddy flux sites located in croplands and other natural land cover types. Improvements in satellite-based ET due to ETo bias reduction tended to be most substantial during the growing season. Although the overall improvements in statistical metrics were modest, even small reductions in bias are valuable when applied across millions of acres or hectares of agricultural land. These findings support the use of bias correction as a necessary step when applying gridded ETo to agricultural and environmental applications in the U.S.

CRediT AUTHORSHIP CONTRIBUTION STATEMENT

John M. Volk: Conceptualization, Methodology, Software, Validation, Formal analysis, Investigation, Data Curation, Visualization, Writing – Original Draft, Writing – Review & Editing; **Christian Dunkerly:** Methodology, Software, Investigation, Validation, Data Curation, Writing – Review & Editing; **Sayantan Majumdar:** Methodology, Formal analysis, Software, Data Curation, Validation, Investigation, Visualization, Writing – Original Draft, Writing – Review & Editing; **Justin L. Huntington:** Funding acquisition, Supervision, Project administration, Conceptualization, Methodology, Investigation, Writing – Review & Editing; **Blake A. Minor:** Methodology, Investigation, Software, Visualization; **Yeonuk Kim:** Investigation, Writing – Original Draft, Writing – Review & Editing, Visualization; **Charles G. Morton:** Methodology, Data Curation, Writing – Review & Editing; **Peter ReVelle:** Formal analysis, Investigation; **Ayse Kilic:** Methodology, Investigation; **Forrest Melton:** Project administration, Methodology, Investigation, Writing – Review & Editing; **Richard G. Allen:** Conceptualization, Project administration, Investigation, Validation, Writing – Review & Editing; **Christopher Pearson:** Methodology, Data Curation, Software, Writing – Review & Editing, Visualization; **Adam J. Purdy:** Project administration, Writing – Review & Editing; **Todd G. Caldwell:** Writing – Review & Editing.

DATA AVAILABILITY

The curated, quality-controlled agricultural weather station reference ET (ETo) dataset used for bias correcting gridMET ETo is available via Dunkerly et al. (2026) and is archived on Zenodo (https://zenodo.org/records/18122157). All analysis scripts and workflows used to generate the results and figures in this manuscript, and the Supplementary Information are available in the following repositories: https://github.com/Open-ET/gridMET-bias-correction (Volk et al., 2026), https://github.com/WSWUP/gridwxcomp (Volk et al., 2025), and https://github.com/WSWUP/agweather-qaqc (Dunkerly et al., 2024). The derived datasets supporting this study, including ETo bias estimates and results products (gridMET, flux ET, and OpenET comparisons), are archived on Zenodo (Volk et al., 2026: https://zenodo.org/records/18673484). Bias-corrected gridMET ETo outputs are also available as Google Earth Engine assets at:

- projects/openet/assets/reference_et/conus/gridmet/monthly/v1
- projects/openet/assets/reference_et/conus/gridmet/daily/v1
- projects/openet/assets/reference_et/conus/gridmet/ratios/v1/monthly/eto
- projects/openet/assets/reference_et/conus/gridmet/ratios/v1/monthly/etr

These can be visualized through this GEE script:
https://code.earthengine.google.com/68688bab0c31c37243bba932169b367c

DECLARATION OF COMPETING INTEREST

The authors declare that they have no known competing financial interests or personal relationships that could have appeared to influence the work reported in this paper.

ACKNOWLEDGMENTS

We gratefully acknowledge funding from the S. D. Bechtel, Jr. Foundation; Walton Family Foundation; Lyda Hill Philanthropies; U.S. Bureau of Reclamation; United States Geological Survey (USGS) Water Resources Research Institute (grant G22AC00584-00); National Aeronautics and Space Administration (NASA) Applied Science Program (grants NNX17AF53G and NNX12AD05A); USGS-NASA Landsat Science Team (grant number 140G0118C0007); USGS Cooperative Ecosystem Studies Units (CESU) (grant G23AC00568); NASA Western Water Applications Office (grant 1669431, 80NSSC23K0836); California State University Agricultural Research Institute (grant number 21-01-106); Desert Research Institute Maki Endowment; and the Windward Fund. We also thank all the weather station network data providers for providing the critical in situ data and the open-source software (Python, QGIS) and open-access data communities (e.g., Google Earth Engine, awesome-gee-community-catalog) for their public resources. Essential computational support was provided by the OpenET consortium, its funding partners, and Google Earth Engine. Finally, we thank our colleagues and families for their unwavering support. The opinions and findings presented here are solely those of the authors and do not necessarily reflect the views of the funding agencies.

REFERENCES

Abatzoglou, J.T., 2013. Development of gridded surface meteorological data for ecological applications and modeling. *International Journal of Climatology*, 33(1), pp.121-131. https://doi.org/10.1002/joc.3413

Albano, C. M., McEvoy, D. J., Huntington, J. L., & Abatzoglou, J. T., 2022. A Multidataset Assessment of Climatic Drivers and Uncertainties of Reference Evapotranspiration across the Contiguous United States. *Journal of Hydrometeorology*, 23(4), 503–518. https://doi.org/10.1175/JHM-D-21-0163.1

Alfieri, J. G., Anderson, M. C., Kustas, W. P., & Cammalleri, C., 2017. Effect of the revisit interval and temporal upscaling methods on the accuracy of remotely sensed evapotranspiration estimates. *Hydrology and Earth System Sciences*, 21(1), 83-98. https://doi.org/10.5194/hess-21-83-2017

Allen, R. G., Pereira, L. S., Walter, I. A., & Jensen, M. E., 2011. Evapotranspiration information reporting: I. Factors governing measurement accuracy. *Irrigation Science*, *30*(2), 135–149.

Allen, R.G., Pereira, L.S., Raes, D., Smith, M., 1998. *Crop evapotranspiration – Guidelines for computing crop water requirements*. FAO Irrigation and Drainage Paper No. 56, Food and Agriculture Organization of the United Nations (FAO), Rome.

Allen, R.G., Tasumi, M. and Trezza, R., 2007. Satellite-based energy balance for mapping evapotranspiration with internalized calibration (METRIC) – Model. *Journal of Irrigation and Drainage Engineering*, 133(4), pp.380-394. https://doi.org/10.1061/(ASCE)0733-9437(2007)133:4(380).

Allen, R. G., Dhungel, R., Dhungana, B., Huntington, J., Kilic, A., & Morton, C., 2021. Conditioning point and gridded weather data under aridity conditions for calculation of reference evapotranspiration. *Agricultural Water Management*, 245, 106531.

ASCE-EWRI. (2005). The ASCE Standardized Reference Evapotranspiration Equation (R. G. Allen, I. A. Walter, R. L. Elliott, T. A. Howell, D. Itenfisu, M. E. Jensen, & R. L. Snyder, Eds.). American Society of Civil Engineers, Reston, VA. https://doi.org/10.1061/9780784408056

Anderson, M., Gao, F., Knipper, K., Hain, C., Dulaney, W., Baldocchi, D., Eichelmann, E., Hemes, K., Yang, Y., Medellin-Azuara, J. & Kustas, W., 2018. Field-scale assessment of land and water use change over the California Delta using remote sensing. *Remote Sensing*, 10(6), p. 889.

Blankenau, P.A., Kilic, A. & Allen, R., 2020. An evaluation of gridded weather data sets for the purpose of estimating reference evapotranspiration in the United States. *Agricultural Water Management*, 242, 106376. https://doi.org/10.1016/j.agwat.2020.106376

Bohn, T. J., Livneh, B., Oyler, J. W., Running, S. W., & Nijssen, B., 2013. Global evaluation of MTCLIM and related algorithms for forcing of ecological and hydrological models. *Agricultural and Forest Meteorology*, 176, 38-49.

Bouchet, R.J., 1963. Evapotranspiration reelle et potentielle, signification climatique. *International Association of Scientific Hydrology*, 62, pp.134–142.

Brutsaert, W., Parlange, M.B., 1998. Hydrologic cycle explains the evaporation paradox. *Nature*, 396, 30. https://doi.org/10.1038/23845

Daly, C., 2006. Guidelines for assessing the suitability of spatial climate data sets. *International Journal of Climatology*, 26, 707–721. https://doi.org/10.1002/joc.1322

Daly, C., Halbleib, M., Smith, J. I., Gibson, W. P., Doggett, M. K., Taylor, G. H., Curtis, J., & Pasteris, P. P., 2008. Physiographically sensitive mapping of climatological temperature and precipitation across the conterminous United States. *International Journal of Climatology*, 28(15), 2031–2064. https://doi.org/10.1002/joc.1688

Doherty, C. T., Wang, W., Hashimoto, H., and Brosnan, I. G., 2025. A method for quantifying uncertainty in spatially interpolated meteorological data with application to daily maximum air temperature, *Geosci. Model Dev*., 18, 3003–3016, https://doi.org/10.5194/gmd-18-3003-2025

Dunkerly, C., Huntington, J. L., McEvoy, D., Morway, A., & Allen, R. G., 2024. agweather-qaqc: An Interactive Python Package for Quality Assurance and Quality Control of Daily Agricultural Weather Data and Calculation of Reference Evapotranspiration. Journal of Open Source Software, 9(97), 6368. https://doi.org/10.21105/joss.06368

Dunkerly, C., Volk, J. M., Majumdar, S., Huntington, J. L., Allen, R.G., Pearson, C., Kim, Y., Morton, C. G., Minor, B. A., ReVelle, P., Kilic, A., Melton, F., Purdy, A. J., & Caldwell, T. G., 2026. CONUS-AgWeather, a high-quality benchmark daily agricultural weather station dataset for evapotranspiration applications in the Contiguous United States (1.0.0) [Data set]. *Zenodo*. https://doi.org/10.5281/zenodo.18122157. Preprint: https://doi.org/10.31223/X56T9Z

Fan, Y., Clark, M., Lawrence, D. M., Swenson, S., Band, L. E., Brantley, S. L., Brooks, P. D., Dietrich, W. E., Flores, A., Grant, G., Kirchner, J. W., Mackay, D. S., McDonnell, J. J., Milly, P. C. D., Sullivan, P. L., Tague, C., Ajami, H., Chaney, N., Hartmann, A., Hazenberg, P., McNamara, J., Pelletier, J., Perket, J., Rouholahnejad-Freund, E., Wagener, T., Zeng, X., Beighley, E., Buzan, J., Huang, M., Livneh, B., Mohanty, B. P., Nijssen, B., Safeeq, M., Shen, C., van Verseveld, W., Volk, J., Yamazaki, D., 2019. Hillslope hydrology in global change research and Earth system modeling. *Water Resources Research*, 55(2), pp. 1737–1772. https://doi.org/10.1029/2018WR023903

Fisher, J.B., Tu, K.P. & Baldocchi, D.D., 2008. Global estimates of the land–atmosphere water flux based on monthly AVHRR and ISLSCP-II data, validated at 16 FLUXNET sites. *Remote Sensing of Environment*, 112, pp. 901-919.

Goble, P.E., Bolinger, R.A. and Schumacher, R.S., 2021. A CONUS-wide standardized precipitation–evapotranspiration index for major U.S. row crops. *Journal of Hydrometeorology*, 22(12), pp.3141-3158. https://doi.org/10.1175/JHM-D-21-0071.1

Gorelick, N., Hancher, M., Dixon, M., Ilyushchenko, S., Thau, D., & Moore, R., 2017. Google Earth Engine: Planetary-scale geospatial analysis for everyone. *Remote Sensing of Environment*, *202*, pp. 18–27. https://doi.org/10.1016/j.rse.2017.06.031

Hobbins, M.T., 2016. The variability of ASCE standardized reference evapotranspiration: A rigorous, CONUS-wide decomposition and attribution. *Transactions of the ASABE*, 59(2), pp.561–576. https://doi.org/10.13031/trans.59.10975.

Hobbins, M. T. and Huntington, J. L., 2016. Evapotranspiration and Evaporative Demand, Chapter 44, Handbook of Applied Hydrology, edited by V. P. Singh, McGraw-Hill Education, New York.

Hobbins, M., Jansma, T., Sarmiento, D. P., McNally, A., Magadzire, T., Jayanthi, H., ... & Dewes, C. F., 2023. A global long-term daily reanalysis of reference evapotranspiration for drought and food-security monitoring. *Scientific Data*, 10(1), 746.

Huntington, J., & Allen, R. G. (2009). Evapotranspiration and Net Irrigation Water Requirements for Nevada. *World Environmental and Water Resources Congress 2009*, 1–15. https://doi.org/10.1061/41036(342)420

Huntington, J., Gangopadhyay, S., Spears, M., Allen, R. G., King, D., Morton, C., Harrison, A., McEvoy, D., Joros, A., & Pruitt, T. (2015). West-Wide Climate Risk Assessments: Irrigation Demand and Reservoir Evaporation Projections (Technical Memorandum No. 68-68210-2014-01) (U.S. Bureau of Reclamation, Ed.). U.S. Bureau of Reclamation.

Jiang, W. & Li, J., 2014. The effects of spatial reference systems on the predictive accuracy of spatial interpolation methods. Canberra, Australia: Geoscience Australia.

Jung, M., Schwalm, C., Migliavacca, M., Walther, S., Camps-Valls, G., Koirala, S., Anthoni, P., Besnard, S., Bodesheim, P., Carvalhais, N., Chevallier, F., Gans, F., Goll, D. S., Haverd, V., Köhler, P., Ichii, K., Jain, A. K., Liu, J., Lombardozzi, D., … Reichstein, M. (2020). Scaling carbon fluxes from eddy covariance sites to globe: synthesis and evaluation of the FLUXCOM approach. *Biogeosciences*, *17*(5), 1343–1365. https://doi.org/10.5194/bg-17-1343-2020

Khand, K., Senay, G. B., Friedrichs, M., Yi, K., Fisher, J. B., Wang, L., Suvočarev, K., Ahmadi, A., Chu, H., Good, S., Mallick, K., Missik, J., Nelson, J. A., Reed, D. E., Wang, T., & Xiao, X., 2025. A novel approach to increase accuracy in remotely sensed evapotranspiration through basin water balance and flux tower constraints. *Journal of Hydrology*, 662, 133824. https://doi.org/10.1016/j.jhydrol.2025.133824

Kiefer, M.T., Andresen, J.A., Doubler, D., & Pollyea, A., 2016. Development of a gridded reference evapotranspiration dataset for the Great Lakes region. *Journal of Hydrology: Regional Studies*, 8, 106-114. https://doi.org/10.1016/j.ejrh.2019.100606

Ketchum, D., Hoylman, Z. H., Huntington, J., Brinkerhoff, D., & Jencso, K. G. (2023). Irrigation intensification impacts sustainability of streamflow in the Western United States. *Communications Earth & Environment*, *4*(1), 479. https://doi.org/10.1038/s43247-023-01152-2

Ketchum, D., Jencso, K., Maneta, M. P., Melton, F., Jones, M. O., & Huntington, J. (2020). IrrMapper: A Machine Learning Approach for High Resolution Mapping of Irrigated Agriculture Across the Western U.S. *Remote Sensing*, *12*(14), 2328. https://doi.org/10.3390/rs12142328

Kim, Y., Garcia, M., Andrew Black, T., & Johnson, M. S. (2025). Physically-constrained evapotranspiration models with machine learning parameterization outperform pure machine learning: Critical role of domain knowledge. *PLOS One*, *20*(7), e0328798. https://doi.org/10.1371/journal.pone.0328798

Kukal, M. S., Kukal, S., Irmak, S., & Vellidis, G. (2024). Drivers of enhanced evaporative demand in U.S. croplands: Determining relative contribution using constrained input scenarios. *JAWRA Journal of the American Water Resources Association*, *60*(1), 79–94. https://doi.org/10.1111/1752-1688.13156

Laipelt, L., Kayser, R.H.B., Fleischmann, A.S., Ruhoff, A., Bastiaanssen, W., Erickson, T.A. & Melton, F., 2021. Long-term monitoring of evapotranspiration using the SEBAL algorithm and Google Earth Engine cloud computing. *ISPRS Journal of Photogrammetry and Remote Sensing*, 178, pp. 81-96.

Lewis, C.S. and Allen, L.N., 2017. Potential crop evapotranspiration and surface evaporation estimates via a gridded weather forcing dataset. *Journal of Hydrology*, *546*, pp.450-463.

Liang, S., & Yu, Y., 2022. A global long-term (1981–2019) daily land surface radiation budget product from AVHRR satellite data using a residual convolutional neural network. *Earth System Science Data*, 14, 2315–2341.

Liu, M., Lei, H., Wang, X., & Paredes, P., 2025. High-resolution mapping of evapotranspiration over heterogeneous cropland affected by soil salinity. *Agricultural Water Management,* 308, 109301. https://doi.org/10.1016/j.agwat.2025.109301

Lobell, D. B., & Bonfils, C., 2008. The effect of irrigation on regional temperatures: A spatial and temporal analysis of trends in California, 1934–2002. *Journal of Climate*, 21(10), 2063–2071. https://doi.org/10.1175/2007JCLI1755.1

Lunel, T., Boone, A.A. and Le Moigne, P., 2024. Irrigation strongly influences near-surface conditions and induces breeze circulation: Observational and model-based evidence. *Quarterly Journal of the Royal Meteorological Society*, 150(762), pp.2798–2819. https://doi.org/10.1002/qj.4736.

Mankin, K. R., Mehan, S., Green, T. R., & Barnard, D. M., 2025. Review of gridded climate products and their use in hydrological analyses reveals overlaps, gaps, and the need for a more objective approach to selecting model forcing datasets. *Hydrology and Earth System Sciences*, 29(1), 85–108. https://doi.org/10.5194/hess-29-85-2025.

Martin, D. J., Niswonger, R. G., Regan, R. S., Huntington, J. L., Ott, T., Morton, C., Senay, G. B., Friedrichs, M., Melton, F. S., Haynes, J., Henson, W., Read, A., Xie, Y., Lark, T., & Rush, M., 2025. Estimating irrigation consumptive use for the conterminous United States: coupling satellite-sourced estimates of actual evapotranspiration with a national hydrologic model. *Journal of Hydrology*, *662*, 133909. https://doi.org/10.1016/j.jhydrol.2025.133909

Martins, D.S., Paredes, P., Raziei, T., Pires, C., Cadima, J., Pereira, L.S., 2017. Assessing reference evapotranspiration estimation from reanalysis weather products. An application to the Iberian Peninsula. *International Journal of Climatology*, 37, pp. 2378–2397. Available at: https://doi.org/10.1002/joc.4852

McEvoy, D.J., Mejia, J.F. and Huntington, J.L., 2014. Use of an observation network in the Great Basin to evaluate gridded climate data. *Journal of Hydrometeorology*, *15*(5), pp.1913-1931.

Melton, F.S., Huntington, J., Grimm, R., Herring, J., Hall, M., Rollison, D. & Anderson, R.G., 2022. OpenET: Filling a critical data gap in water management for the Western United States. *JAWRA Journal of the American Water Resources Association*. https://doi.org/10.1111/1752-1688.12956

Melton, F.S., Johnson, L.F., Lund, C.P., Pierce, L.L., Michaelis, A.R., Hiatt, S.H., Guzman, A., Adhikari, D.D., Purdy, A.J., Rosevelt, C. & Votava, P., 2012. Satellite irrigation management support with the terrestrial observation and prediction system: A framework for integration of satellite and surface observations to support improvements in agricultural water resource management. *IEEE Journal of Selected Topics in Applied Earth Observations and Remote Sensing*, 5(6), pp. 1709-1721.

Ménard, R., 2010. Bias estimation. In: W. Lahoz, B. Khattatov and R. Ménard, eds., *Data assimilation*. Berlin Heidelberg: Springer, pp. 113-135. Available at: https://doi.org/10.1007/978-3-540-74703-1_6

Mesinger, F., DiMego, G., Kalnay, E., Mitchell, K., Shafran, P. C., Ebisuzaki, W., Jović, D., Woollen, J., Rogers, E., Berbery, E. H., Ek, M. B., Fan, Y., Grumbine, R., Higgins, W., Li, H., Lin, Y., Manikin, G., Parrish, D., & Shi, W., 2006. North American Regional Reanalysis. *Bulletin of the American Meteorological Society*, 87(3), 343–360. https://doi.org/10.1175/BAMS-87-3-343

Moorhead, J., Gowda, P., Hobbins, M., Senay, G., Paul, G., Marek, T. & Porter, D., 2015. Accuracy assessment of NOAA gridded daily reference evapotranspiration for the Texas High Plains. *JAWRA Journal of the American Water Resources Association*, 51(5), pp.1262–1271.

Morton, F. I., 1994. Evaporation Research—a Critical Review and Its Lessons for the Environmental Sciences, *Critical Reviews in Environmental Science and Technology*, vol. 24, no. 3, 237–80. https://doi.org/10.1080/10643389409388467

Obrecht, N.A., 2019. Sample size weighting follows a curvilinear function. *Journal of Experimental Psychology: Learning, Memory, and Cognition*, 45, p. 614.

Ott, T. J., Majumdar, S., Huntington, J. L., Pearson, C., Bromley, M., Minor, B. A., ReVelle, P., Morton, C. G., Sueki, S., Beamer, J. P., & Jasoni, R. L., 2024. Toward field-scale groundwater pumping and improved groundwater management using remote sensing and climate data. *Agricultural Water Management*, *302*, 109000. https://doi.org/10.1016/j.agwat.2024.109000

Paredes, P., Martins, D.S., Pereira, L.S., Cadima, J., Pires, C., 2018. Accuracy of daily estimation of grass reference evapotranspiration using ERA-Interim reanalysis products with assessment of alternative bias correction schemes. *Agricultural Water Management*, 210, pp. 340–353. Available at: https://doi.org/10.1016/j.agwat.2018.08.003

Pereira, L.S., Allen, R.G., Smith, M., Raes, D., 2015. Crop evapotranspiration estimation with FAO56: Past and future. *Agricultural Water Management*, 147, 4–20. https://doi.org/10.1016/j.agwat.2014.07.031

Pereira, L.S., Paredes, P., Melton, F., Johnson, L., Wang, T., López-Urrea, R., Cancela, J.J. and Allen, R.G., 2020. Prediction of crop coefficients from fraction of ground cover and height: Background and validation using ground and remote sensing data. *Agricultural Water Management*, 241, p.106197. https://doi.org/10.1016/j.agwat.2020.106197.

Phillips, C.E., Nair, U.S., Mahmood, R., Rappin, E. and Pielke Sr, R.A., 2022. Influence of irrigation on diurnal mesoscale circulations: Results from GRAINEX. *Geophysical Research Letters*, 49(7), 2021GL096822. https://doi.org/10.1029/2021GL096822.

Pierce, D. W., Cayan, D. R., & Thrasher, B. L., 2014. Statistical downscaling using localized constructed analogs (LOCA). *Journal of Hydrometeorology*, 15(6), 2558–2585. https://doi.org/10.1175/JHM-D-14-0082.1

Pondeca, M.S.F.V., Manikin, G.S., DiMego, G., Benjamin, S.G., Parrish, D.F., Purser, R.J., & Vavra, J., 2011. The Real-Time Mesoscale Analysis at NOAA's National Centers for Environmental Prediction: Current status and development. *Weather and Forecasting*, 26(5), pp.593–612. https://doi.org/10.1175/WAF-D-10-05037.1

Reitz, M., Volk, J. M., Ott, T., Anderson, M., Senay, G. B., Melton, F., Kilic, A., Allen, R., Fisher, J. B., Ruhoff, A., Purdy, A. J., & Huntington, J. (2025). Performance Mapping and Weighting for the Evapotranspiration Models of the OpenET Ensemble. *Water Resources Research*, *61*(8). https://doi.org/10.1029/2024WR038899

Roy, S., Jensen, E., Majumdar, S., & Saah, A. (2025). samapriya/awesome-gee-community-datasets: Community Catalog (3.8.0). https://doi.org/10.5281/zenodo.17248117

Kottek, M., Grieser, J., Beck, C., Rudolf, B., & Rubel, F. (2006). World Map of the Köppen-Geiger climate classification updated. Meteorologische Zeitschrift, 15(3), 259–263. https://doi.org/10.1127/0941-2948/2006/0130

Sabino, M., da Silva, A.C., de Almeida, F.T. and de Souza, A.P., 2024. Reference evapotranspiration in climate change scenarios in Mato Grosso, Brazil. *Hydrology*, *11*(7), p.91.

Senay, G.B., Parrish, G.E., Schauer, M., Friedrichs, M., Khand, K., Boiko, O., Kagone, S., Dittmeier, R., Arab, S. and Ji, L., 2023. Improving the operational simplified surface energy balance evapotranspiration model using the forcing and normalizing operation. *Remote Sensing*, 15(1), p.260. https://doi.org/10.3390/rs15010260.

Shen, Y., & Du, Y., 2023. Sensitivity of boundary layer parameterization schemes in a marine boundary layer jet and associated precipitation during a coastal warm-sector heavy rainfall event. *Frontiers in Earth Science*, 10, 1085136.

Silva Dias, M. A. F., Rutledge, S., Kabat, P., et al., 2002. Cloud and rain processes in a biosphere-atmosphere interaction context in the Amazon Region. *Journal of Geophysical Research*: *Atmospheres*, 107(D20), LBA 39-1–LBA 39-18.

Szilagyi, J., Józsa, J., 2008. New findings about the complementary relationship-based evaporation estimation methods. *Journal of Hydrology*, 354, 171–186. https://doi.org/10.1016/j.jhydrol.2008.03.008

Trebs, I., Mallick, K., Bhattarai, N., et al., 2021. The role of aerodynamic resistance in thermal remote sensing-based evapotranspiration models. *Remote Sensing of Environment*, 264, 112602. https://doi.org/10.1016/j.rse.2021.112602

Volk, J., Dunkerly, C., Majumdar, S., Huntington, J., Minor, B., Kim, Y., Morton, C., ReVelle, P., Kilic, A., Melton, F., Allen, R., Pearson, C., Purdy, A., & Caldwell, T. (2026). CONUS Gridded Reference Evapotranspiration Bias Correction: Inputs, Station Validation, and Outputs (gridMET/OpenET) [Data set]. *Zenodo*. https://doi.org/10.5281/zenodo.18673484

Volk, J.M., Dunkerly, C., Pearson, C., Morton, C.G. and Huntington, J.L., 2025. gridwxcomp: A Python package to evaluate and interpolate biases between station and gridded weather data. *Journal of Open Source Software.* 10(105), 7178. https://doi.org/10.21105/joss.07178

Volk, J. M., Huntington, J., Melton, F. S., Allen, R., Anderson, M. C., Fisher, J. B., Kilic, A., Senay, G., Halverson, G., Knipper, K., Minor, B., Pearson, C., Wang, T., Yang, Y., Evett, S., French, A. N., Jasoni, R., & Kustas, W. P., 2023a. Development of a benchmark eddy flux evapotranspiration dataset for evaluation of satellite-driven evapotranspiration models over the CONUS. *Agricultural and Forest Meteorology*, 330, 109307. https://doi.org/10.1016/j.agrformet.2023.109307

Volk, J. M., Huntington, J. L., Melton, F., Minor, B., Wang, T., Anapalli, S., Anderson, R. G., Evett, S., French, A., Jasoni, R., Bambach, N., Kustas, W. P., Alfieri, J., Prueger, J., Hipps, L., McKee, L., Castro, S. J., Alsina, M. M., McElrone, A.J., Reba, M., Runkle, B., Saber, M., Sanchez, C., Tajfar, E., Allen, R., and Anderson, M., 2023b. Post-processed data and graphical tools for a CONUS-wide eddy flux evapotranspiration dataset. *Data in Brief*, 48, 109274.https://doi.org/10.1016/j.dib.2023.109274

Walton, D. and Hall, A., 2018. An assessment of high-resolution gridded temperature datasets over California. *Journal of Climate*, 31(10), pp. 3789–3810. https://doi.org/10.1175/JCLI-D-17-0410.1

Yu, L., Bian, X., & Heilman, W. E., 2015. Temporal and spatial variability of wind resources in the United States as derived from the Climate Forecast System Reanalysis. *Journal of Climate*, 28(3), 1166-1183.

Xia, Y., Mitchell, K., Ek, M., Cosgrove, B., Sheffield, J., Luo, L., Lohmann, D., 2012. Continental-scale water and energy flux analysis and validation for North American Land Data Assimilation System project phase 2 (NLDAS-2): 2. Validation of model-simulated streamflow. *Journal of Geophysical Research: Atmospheres*, 117(3). https://doi.org/10.1029/2011JD016051

Xie, Y., Gibbs, H. K., & Lark, T. J.,2021. Landsat-based Irrigation Dataset (LANID): 30 m resolution maps of irrigation distribution, frequency, and change for the US, 1997–2017. *Earth System Science Data*, *13*(12), 5689–5710. https://doi.org/10.5194/essd-13-5689-2021

Xie, Y., Lark, T. J., Brown, J. F., & Gibbs, H. K.,2019. Mapping irrigated cropland extent across the conterminous United States at 30 m resolution using a semi-automatic training approach on Google Earth Engine. *ISPRS Journal of Photogrammetry and Remote Sensing*, *155*, 136–149. https://doi.org/10.1016/j.isprsjprs.2019.07.005

FIGURES

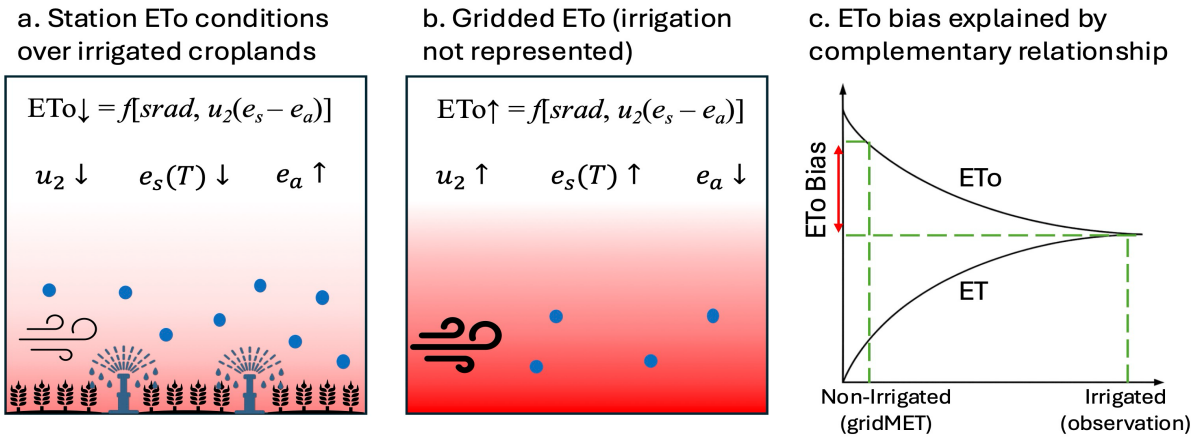

Figure 1. Conceptual framework illustrating the hypothesized causes of positive bias in gridded reference evapotranspiration (ETo) datasets over irrigated agricultural areas. Panels (a) and (b) contrast the microclimatic and aerodynamic conditions between irrigated and non-irrigated environments, highlighting the cooling, humidifying, and roughness effects of irrigation that are not well captured in coarse-resolution gridded data. Panel (c) links these effects to the complementary relationship, which posits that as actual ET decreases under water-limited conditions, potential or ETo increases. This framework underlies the hypothesis that gridded ETo overestimates irrigated ETo due to failure to represent irrigation-modified surface conditions in meteorological data and land surface models.

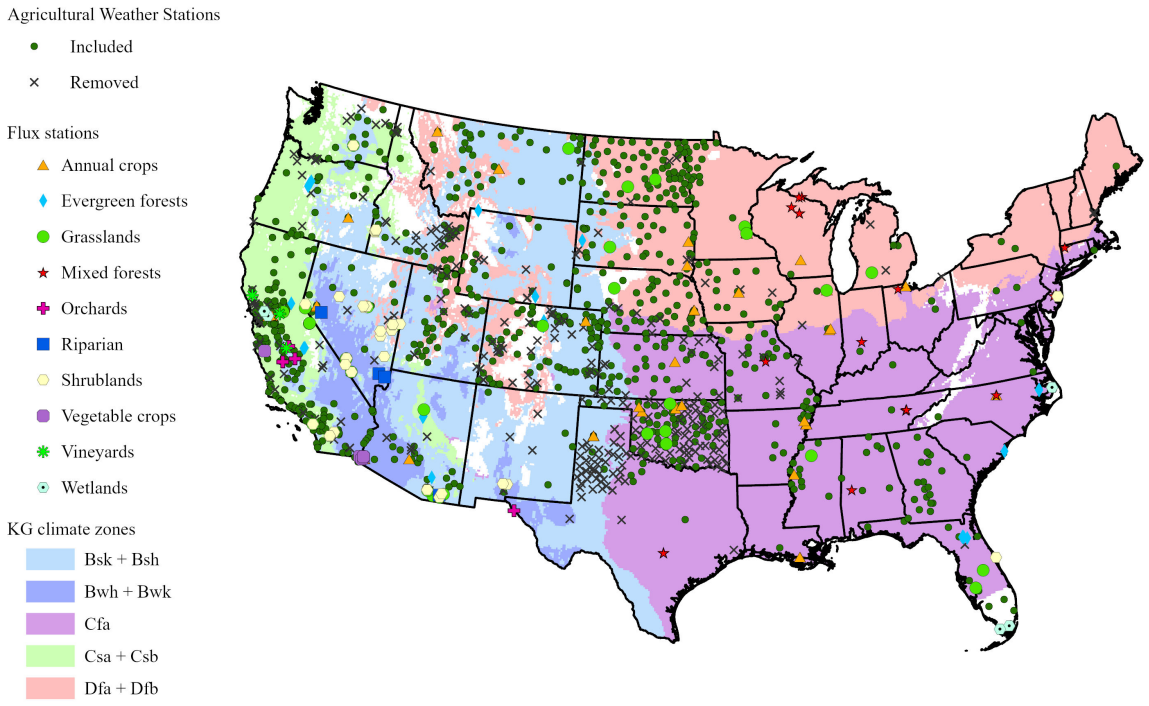

Figure 2. Distribution of agricultural ETo stations included and removed as a result of station and data QC (Dunkerly et al., 2025), and micrometeorological "flux" stations (Volk et al., 2023a,b) included for independent comparisons of bias-corrected ETo and OpenET RSET model predictions. Also illustrated are Köppen-Geiger climate zones used to characterize ETo bias (Kottek et al., 2006). Climate zone abbreviations are defined as follows: cold and hot semi-arid steppe (Bsk + Bsh); hot and cold desert (Bwh + Bwk); humid subtropical (Cfa); hot- and warm-summer Mediterranean (Csa + Csb); and hot- and warm-summer humid continental (Dfa + Dfb).

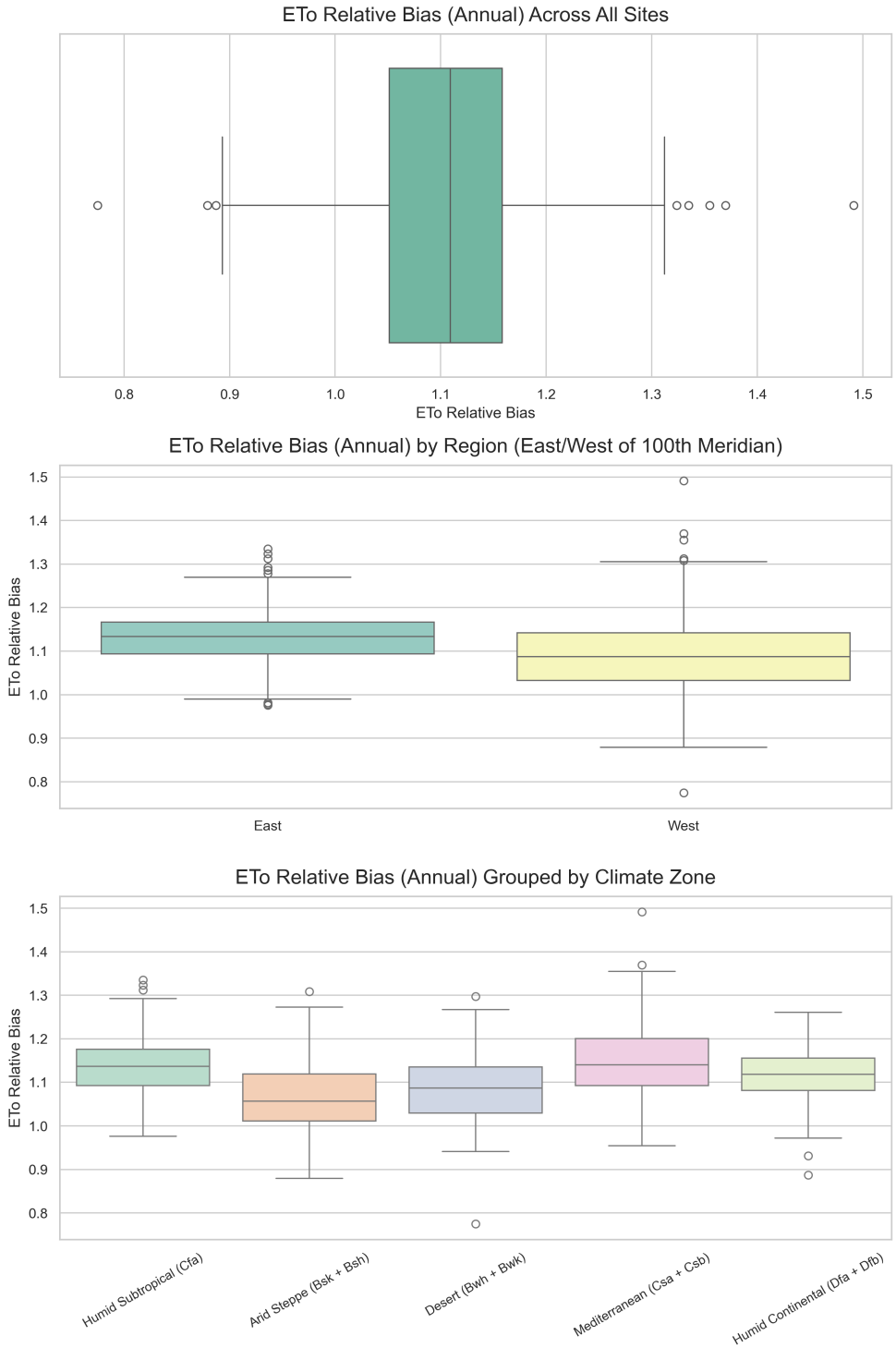

Figure 3. Box and whisker plots of the average annual ratio (i.e. bias) of gridMET ETo relative to agricultural weather station ETo, using all 793 stations, grouped by geographic and Köppen-Geiger climate zones (Rubel et al., 2017).

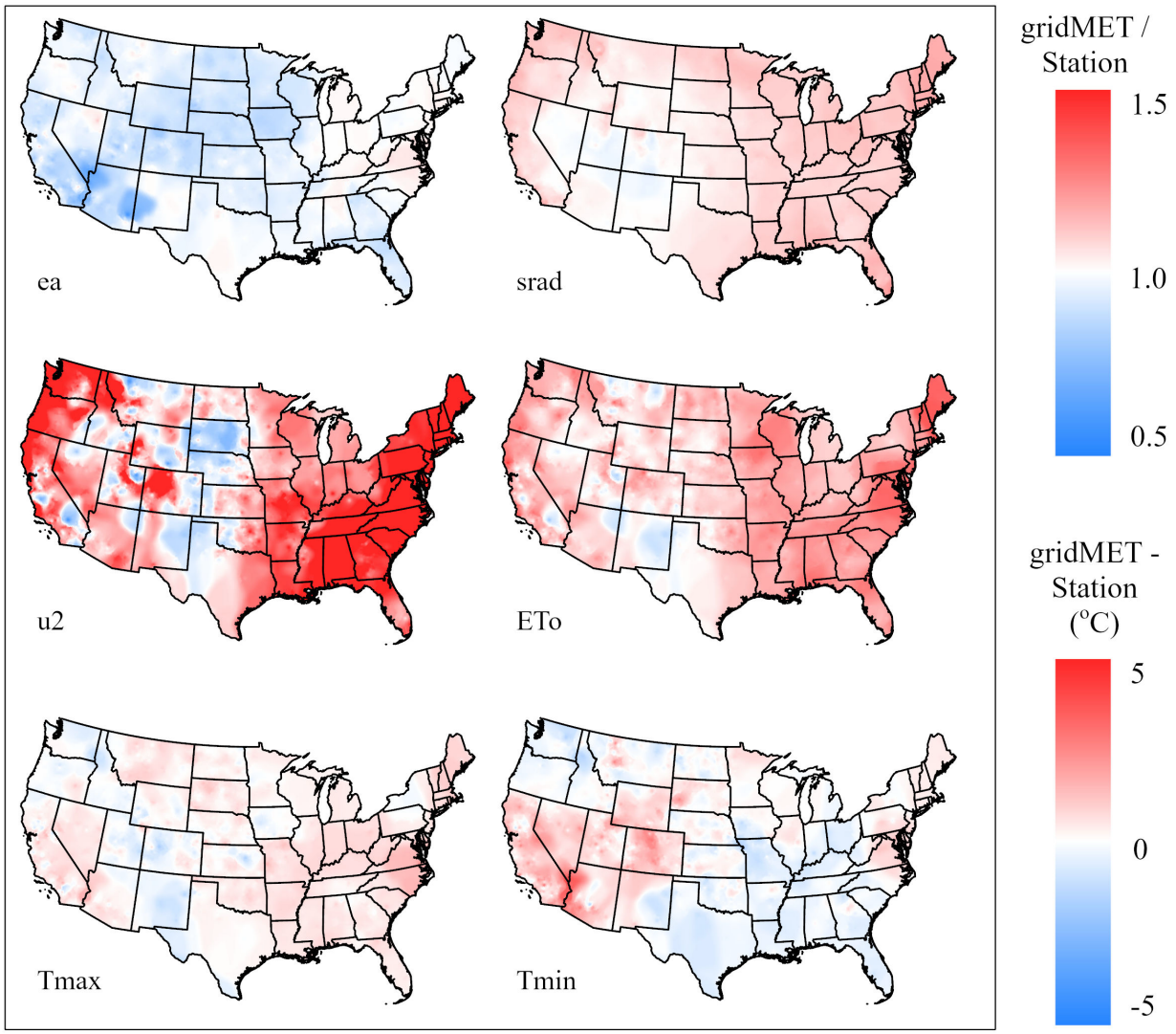

Figure 4. Spatially interpolated mean annual relative bias of vapor pressure (ea), solar radiation (srad), 2-meter wind speed (u2), Penman-Monteith Standardized grass reference ET (ETo), and daily maximum and minimum temperature differences.

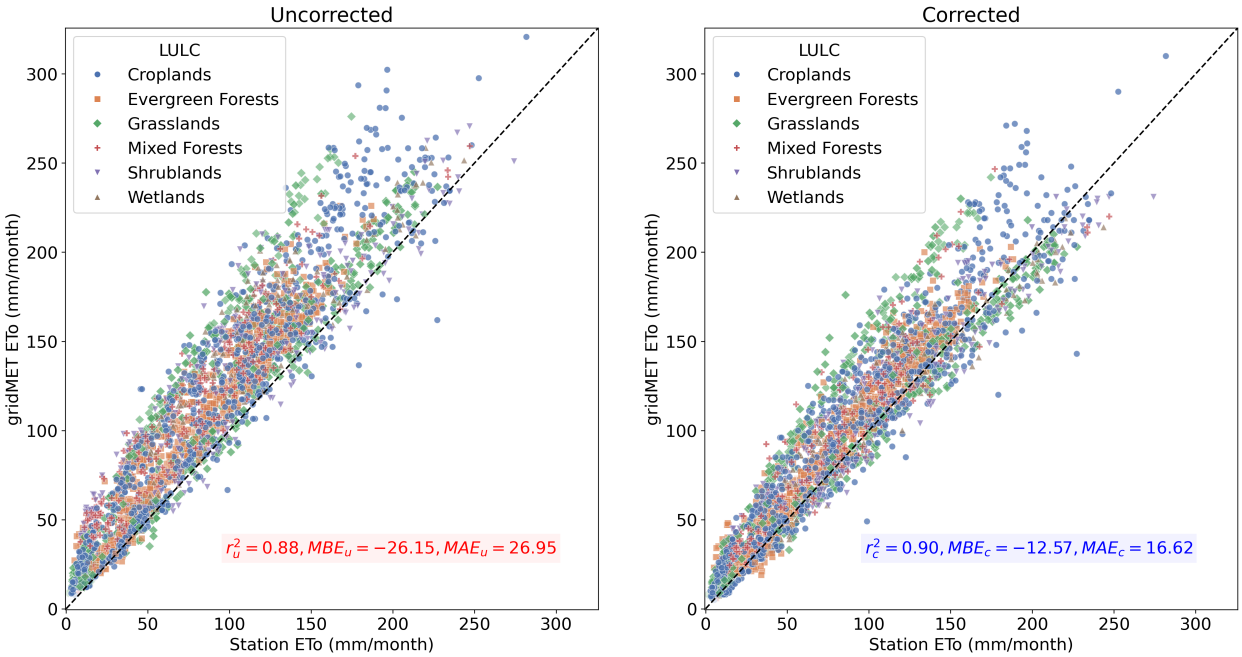

Figure 5. Monthly gridMET ETo before (left) and after (right) bias correction versus independently estimated in situ measured ETo at 79 flux stations across the CONUS. The subscripts 'u' and 'c' denote the error metrics for the uncorrected and bias-corrected ETo, respectively.

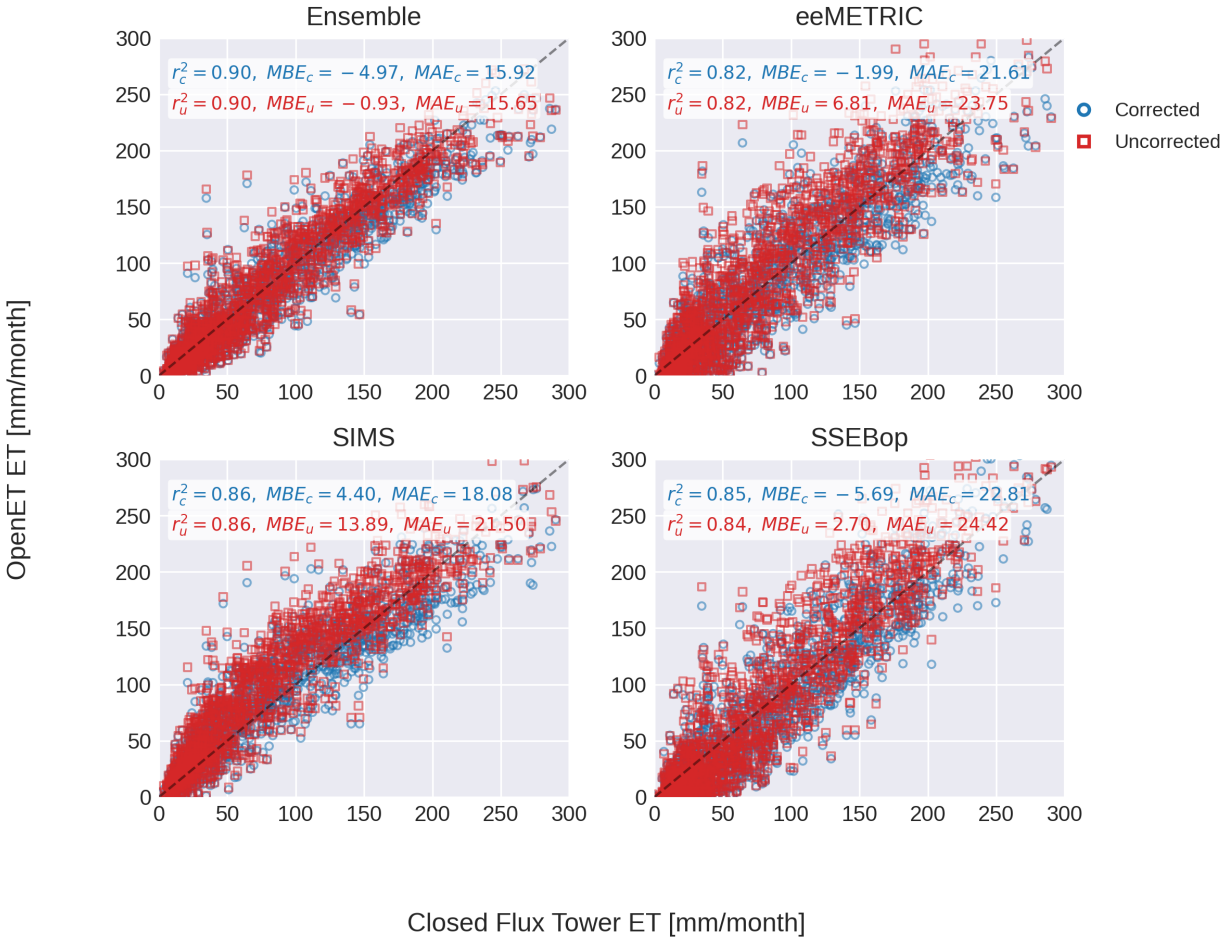

Figure 6. Monthly ET from OpenET remote sensing models versus closed flux towers located in croplands for models that rely on gridded ETo (eeMETRIC, SIMS, and SSEBop) and the OpenET ensemble which includes three other models that do not use ETo for computing ET. Model data are shown with and without bias correction applied to gridded ETo. The subscripts ‘u’ and ‘c’ denote the error metrics for the uncorrected ETo-derived OpenET RSET and the bias-corrected ETo-derived OpenET RSET, respectively.

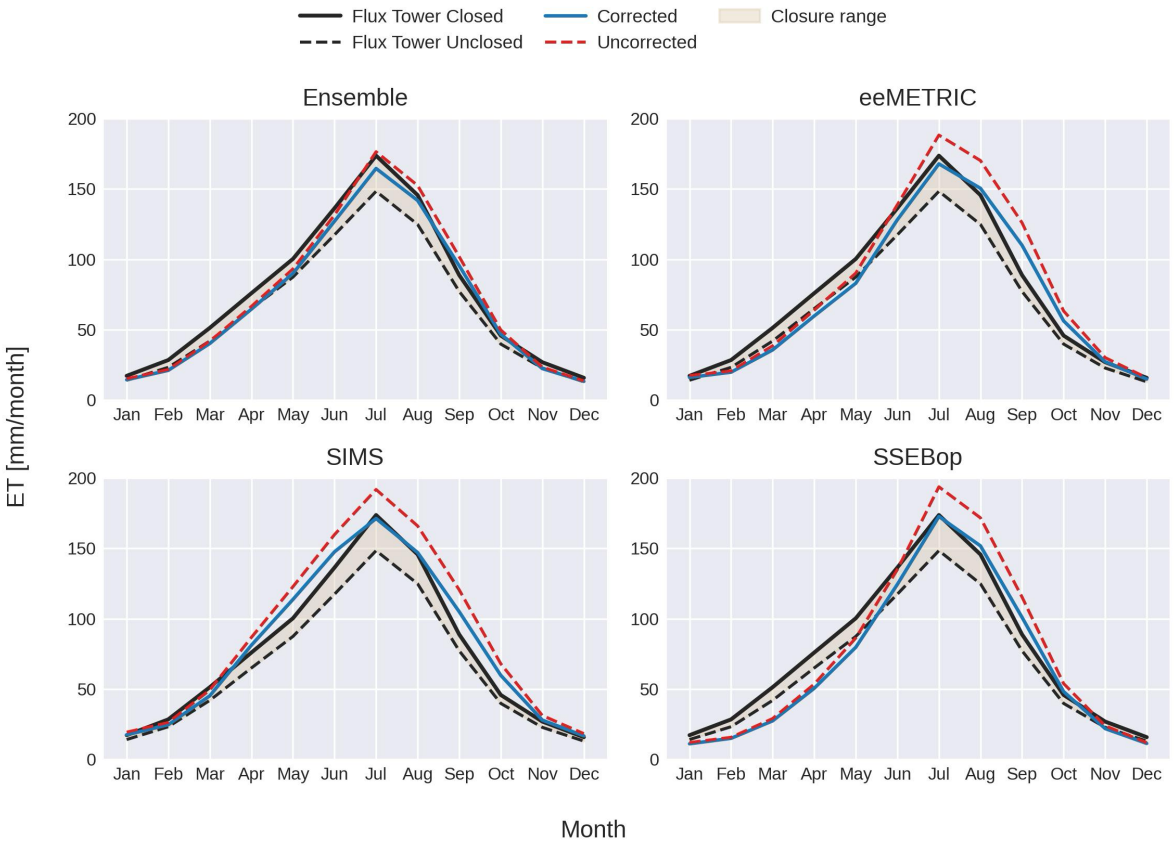

Figure 7. Mean monthly ET from OpenET remote sensing models before and after ETo bias correction and monthly mean flux tower ET that has been corrected and not corrected for energy balance closure error ("Closed" and "Unclosed"). The range between the closed and unclosed flux tower ET are shown to give a band of uncertainty associated with the flux tower ET measurements. Data shown is for croplands flux sites and for models that rely on gridded ETo (eeMETRIC, SIMS, and SSEBop) and the OpenET ensemble which includes three other models that do not use ETo for computing ET.

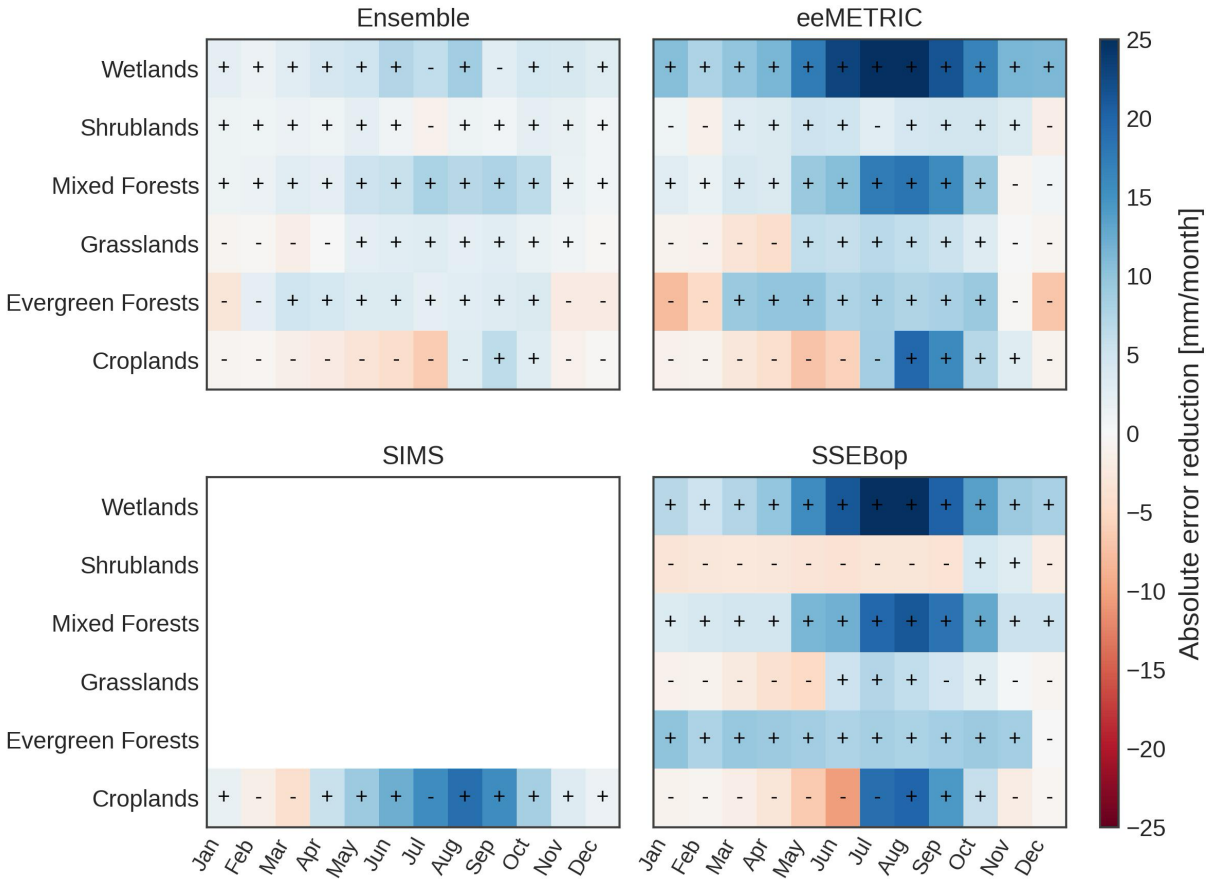

Figure 8. Change in absolute mean monthly model–flux ET difference after applying an ETo bias correction (blue = improvement; red = dis-improvement). Symbols indicate the sign of the residual model bias relative to flux ET after ETo correction ("+" = model > flux ET; "–" = model < flux ET). Rows are flux sites grouped by land cover (Wetlands include riparian sites). Panels show eeMETRIC, SIMS, SSEBop (ETo-scaled) and the OpenET ensemble (which also includes models that do not use ETo).

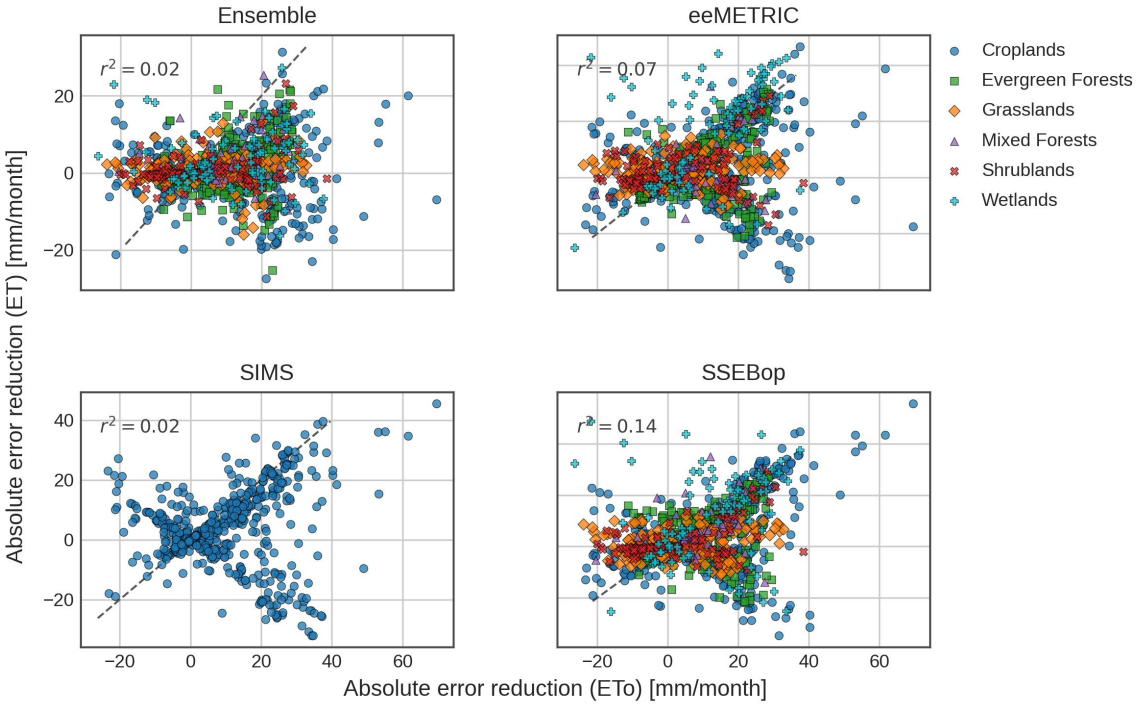

Figure 9. Absolute improvement in monthly model–flux ET after applying an ETo bias correction versus improvement in ETo at the same flux stations. Colors show monthly paired errors grouped by land cover. Dashed line is 1:1.

APPENDICES

Appendix A: ASCE Standardized Penman-Monteith Equation (Daily Version)

Equation:

$$ET_o = \frac{0.408\Delta(R_n - G) + \gamma \frac{900}{T + 273} u_2 (e_s - e_a)}{\Delta + \gamma(1 + 0.34)u_2}$$

Net radiation from solar radiation:

$$R_n = (1 - \alpha)R_s - R_{nl}$$

Variable Definitions:

- ET_o: Reference evapotranspiration for short grass (mm/day)
- Δ: Slope of saturation vapor pressure curve at air temperature T (kPa/°C)
- R_n: Net radiation at the crop surface (MJ/m²/day)
- R_s: Incoming solar radiation (MJ/m²/day)
- R_{nl}: Net outgoing longwave radiation (MJ/m²/day)
- α: Surface albedo (typically 0.23 for grass)
- γ: Psychrometric constant (kPa/°C)
- T: Mean daily air temperature (°C), average of T_{max} and T_{min}
- u_2: Wind speed at 2 meters height (m/s)
- e_s: Saturation vapor pressure (kPa), from T
- e_a: Actual vapor pressure (kPa), from RH or dewpoint
- VPD: Vapor pressure deficit (e_s - e_a) (kPa)

Appendix B: Monthly Bias Ratio, Bias Difference, and Coefficient of Variation

Monthly bias ratio (for non-temperature variables):

$$BiasRatio_m = \frac{\overline{S_m}}{\overline{G_m}}$$

Where $\overline{S_m}$ and $\overline{G_m}$ are the long-term monthly means of daily station and gridded values, respectively, for calendar month m.

Monthly bias difference (for temperature variables):

$$BiasDifference_m = \overline{S_m} - \overline{G_m}$$

used instead of a ratio for variables like temperature, based on paired daily values pooled across all years for calendar month m.

Long-Term monthly means were calculated as:

$$\overline{S_m} = \frac{\sum S_d}{N_{days,m}}$$

$$\overline{G_m} = \frac{\sum G_d}{N_{days,m}}$$

where the summations are taken over all valid paired daily values in calendar month m across all years.

Coefficient of variation (CV) for calendar month m:

$$CV_m = \frac{\sigma(Annual_m)}{\mu(Annual_m)}$$

where the numerator and denominator are the standard deviation and mean, respectively, of the set of annual (calculated for each year on record as opposed to all days pooled across all years) monthly bias ratios or differences for calendar month m.

Variable Definitions:

- $BiasRatio_m$: Long-term mean bias ratio for calendar month m
- $BiasDifference_m$: Long-term mean bias difference for calendar month m (used for temperature variables)
- $\overline{S_m}$: Long-term mean of station values for calendar month m
- $\overline{G_m}$: Long-term mean of gridded values for calendar month m
- S_d: Station value on a valid day d within calendar month m, pooled across all years
- G_d: Gridded value on the same day d
- $N_{days,m}$: Number of valid paired days in calendar month m across all years
- CV_m: Coefficient of variation for calendar month m
- σ ($Annual_m$): Standard deviation of annual monthly bias ratios (or differences) for calendar month m
- μ ($Annual_m$): Mean of annual monthly bias ratios (or differences) for calendar month m

Appendix C: Error Metrics

The mean bias error (MBE) was calculated as:

$$MBE = \frac{1}{n}\sum_{i=1}^{n}(P_i - O_i)$$

The mean absolute error (MAE) was calculated as:

$$MAE = \frac{1}{n}\sum_{i=1}^{n}|P_i - O_i|$$

And the root mean square error (RMSE) was calculated as:

$$MBE = \sqrt{\sum_{i=1}^{n} \frac{(P_i - O_i)^2}{n}}$$

Variable Definitions:

- O_i: the observed ET
- P_i: the model predicted ET
- n: is the total number of paired model-measured ET data points

Supplementary Information for "Assessing and Correcting Bias in Gridded Reference Evapotranspiration over Agricultural Lands Across the Contiguous United States"

John M. Volk [a2], Christian Dunkerly [a], Sayantan Majumdar [a], Justin L. Huntington [a], Blake A. Minor [a], Yeonuk Kim [a], Charles G. Morton [a], Peter ReVelle [a], Ayse Kilic [b], Forrest Melton [c, d], Richard G. Allen [e], Christopher Pearson [a], Adam J. Purdy [c, d], Todd G. Caldwell [a]

[a] Desert Research Institute, Reno, NV, USA
[b] University of Nebraska-Lincoln, Lincoln, NE, USA
[c] NASA Ames Research Center, Moffett Field, CA, USA
[d] California State University, Monterey Bay, Seaside, CA, USA
[e] (ret) University of Idaho, Kimberly, ID, USA

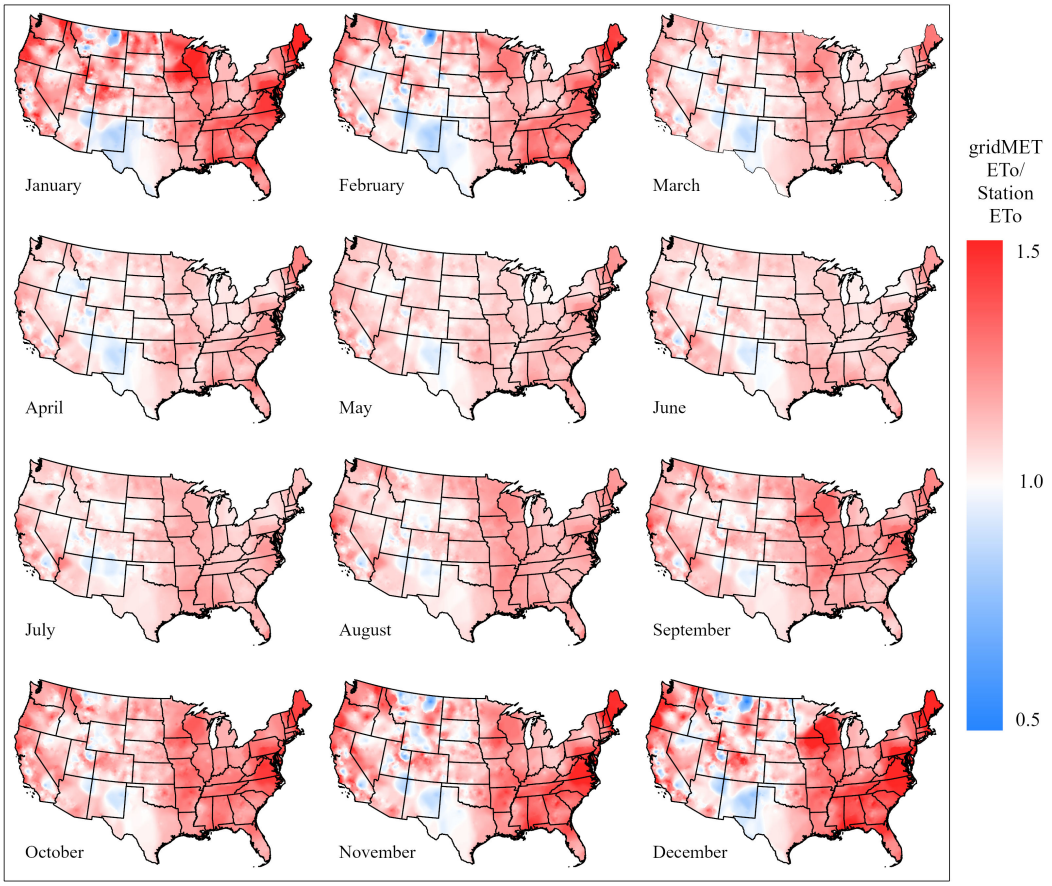

Supplementary Figure 1. Spatially interpolated monthly average gridMET grass reference ET (ETo) bias relative to ETo measured at agricultural weather stations.

[2] Corresponding author at: Division of Hydrologic Sciences, Desert Research Institute, 2215 Raggio Parkway, Reno, Nevada 89512-1095, USA
Email address: john.volk@dri.edu (John M. Volk)

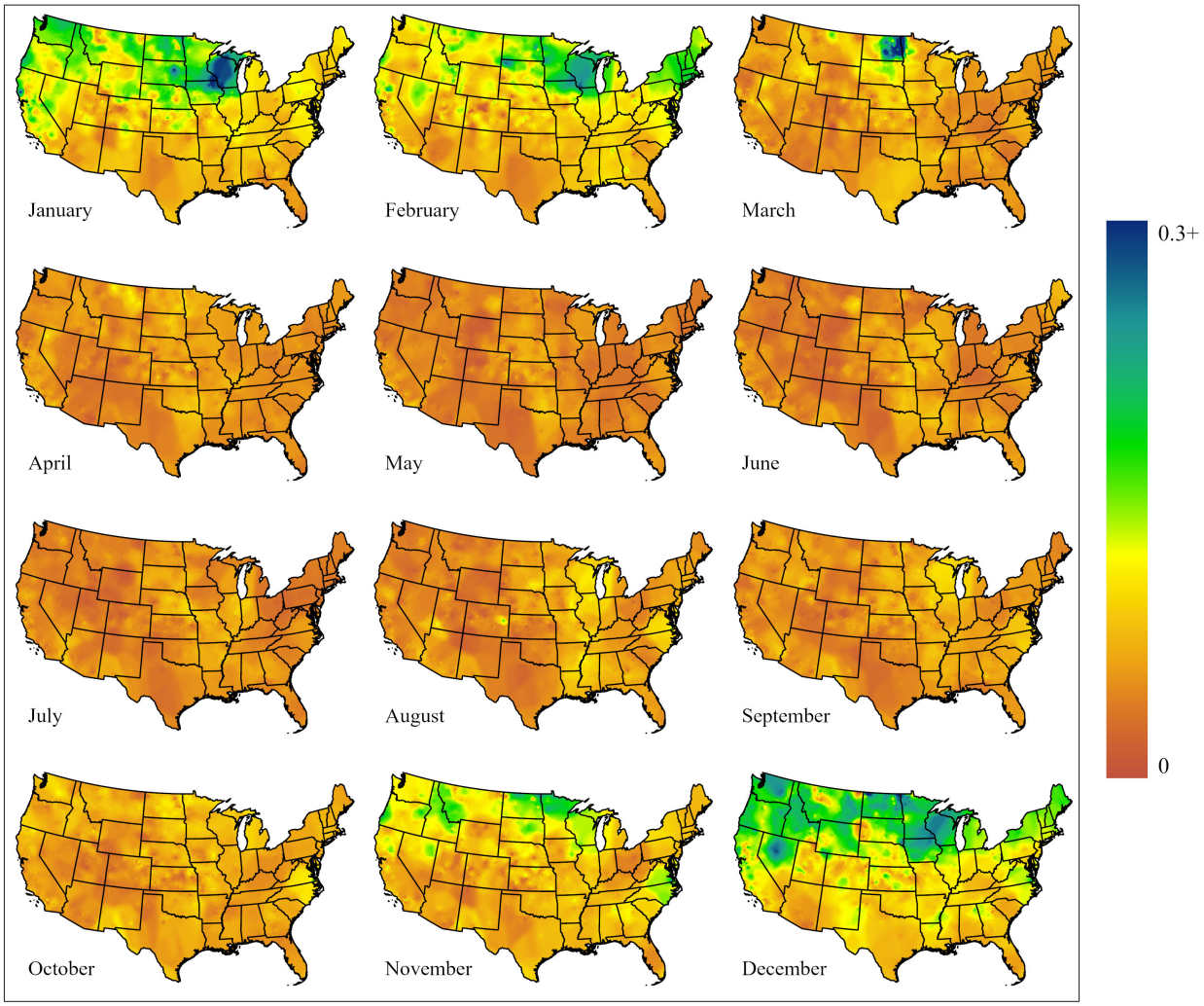

Supplementary Figure 2. Spatially interpolated annual average monthly coefficients of variation of gridMET ETo bias relative to ETo calculated at agricultural weather stations.

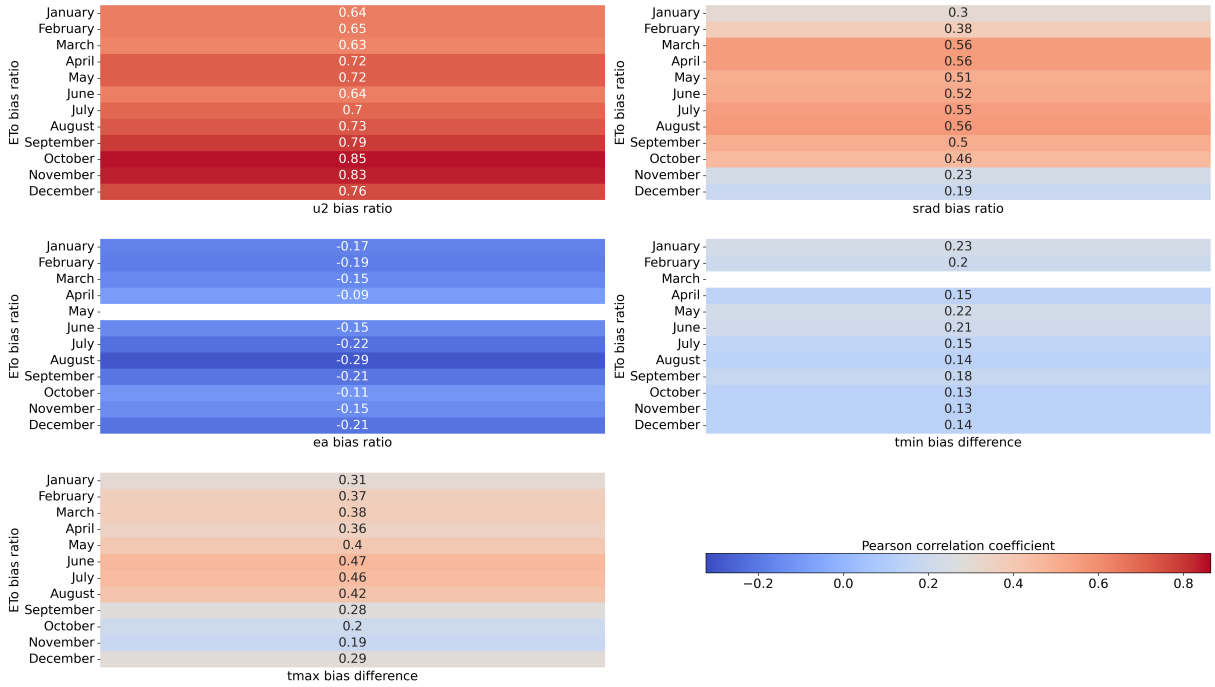

Supplementary Figure 3. Monthly Pearson correlation coefficients (r) between ETo and each forcing variable. Missing ea and tmin values for May and March, respectively, indicate that these correlations are not statistically significant, i.e., p-value ≥ 0.05, considering a 95% significance level.

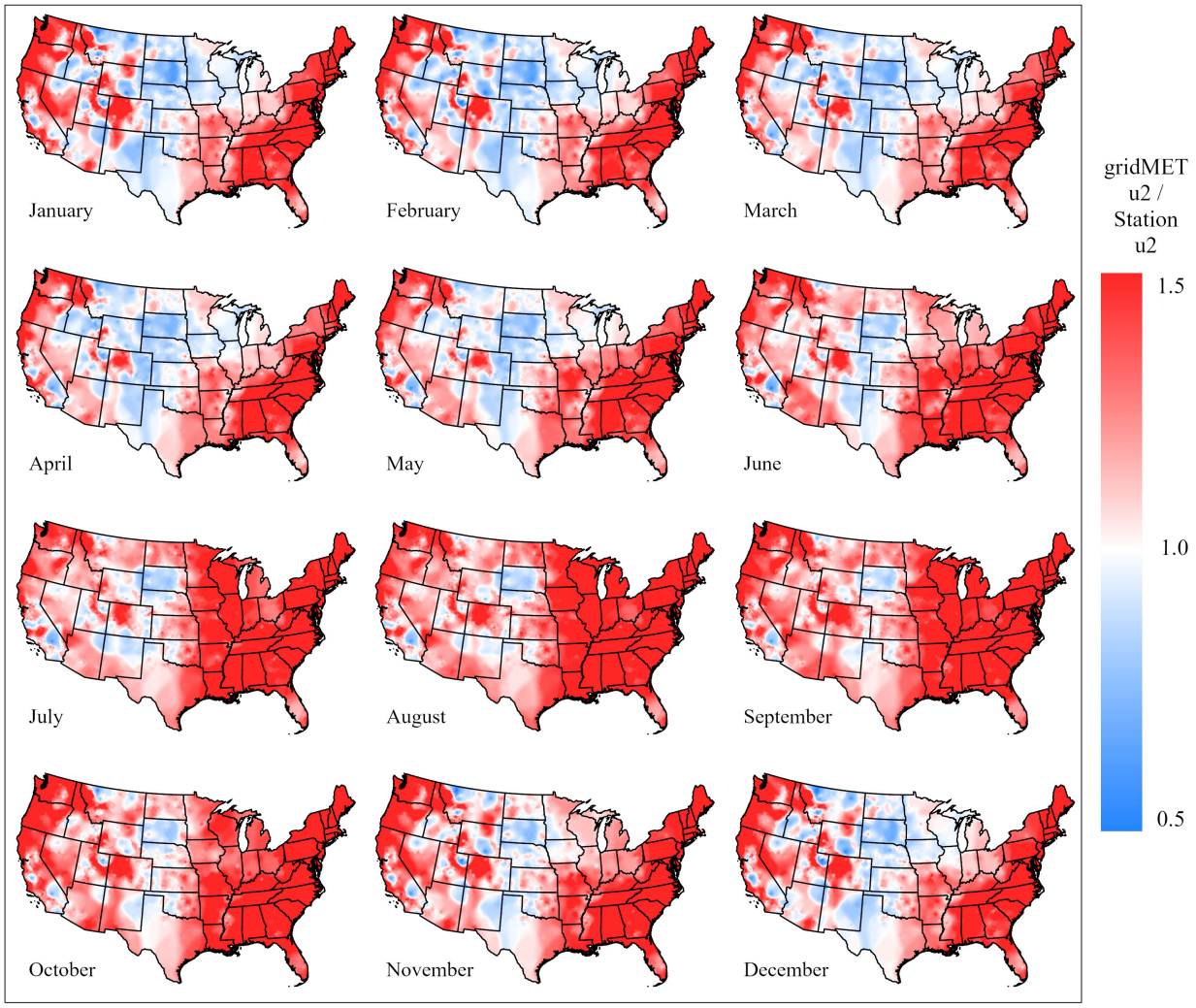

Supplementary Figure 4. Spatially interpolated monthly average gridMET 2-meter wind speed (u2) bias relative to u2 measured at agricultural weather stations.

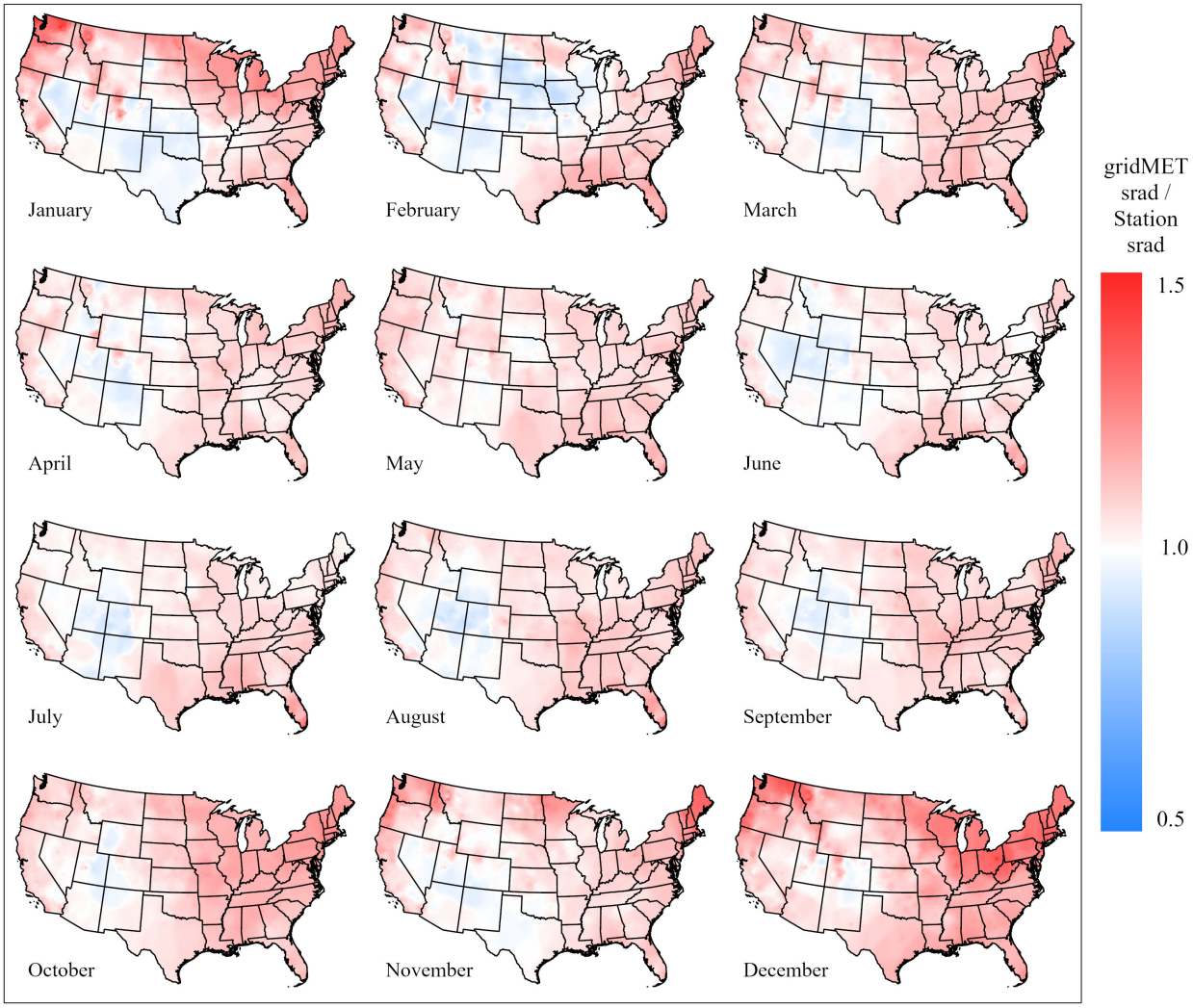

Supplementary Figure 5. Spatially interpolated monthly average gridMET solar radiation (srad) bias relative to srad measured at agricultural weather stations.

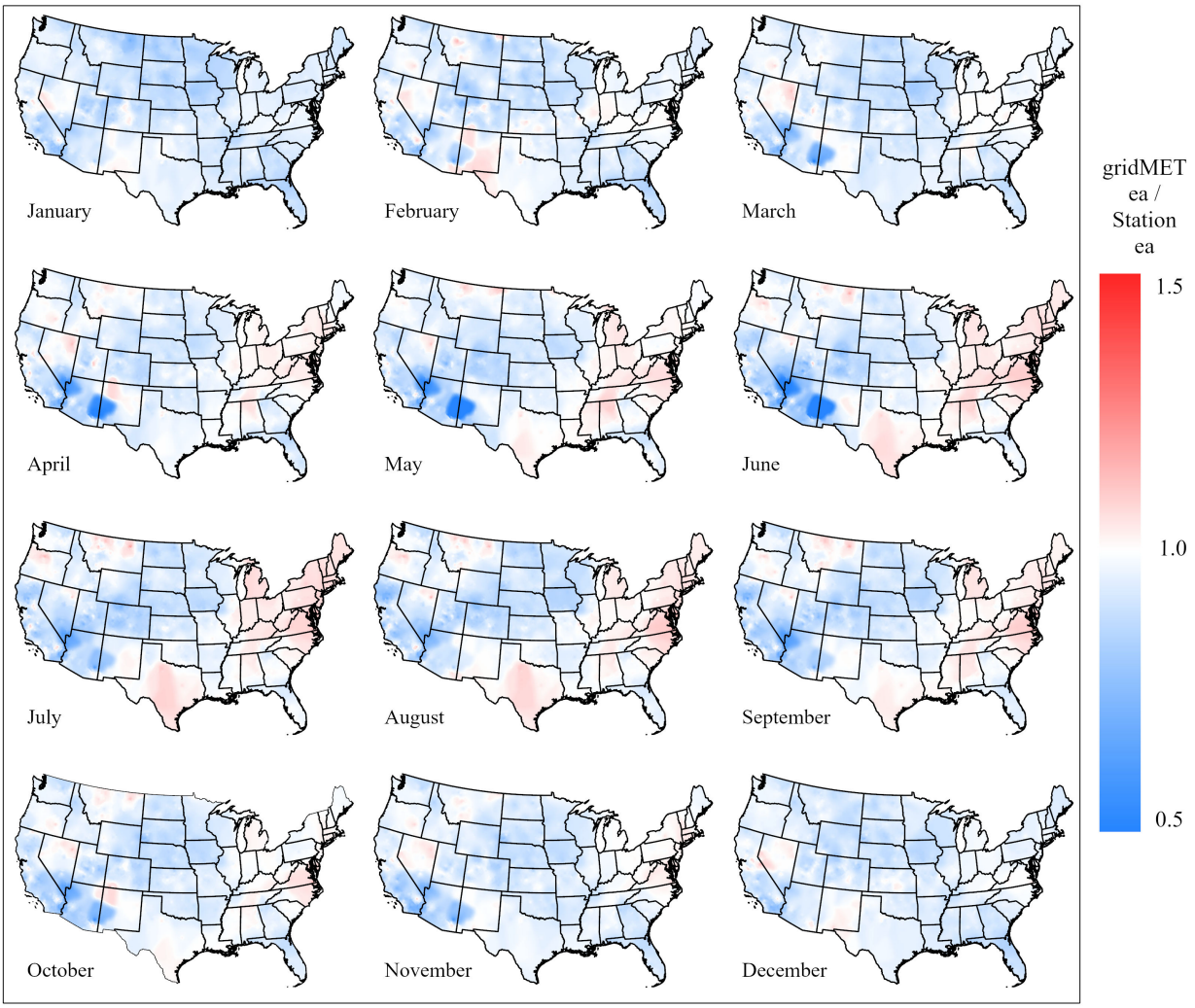

Supplementary Figure 6. Spatially interpolated monthly average gridMET vapor pressure (ea) bias relative to ea measured at agricultural weather stations.

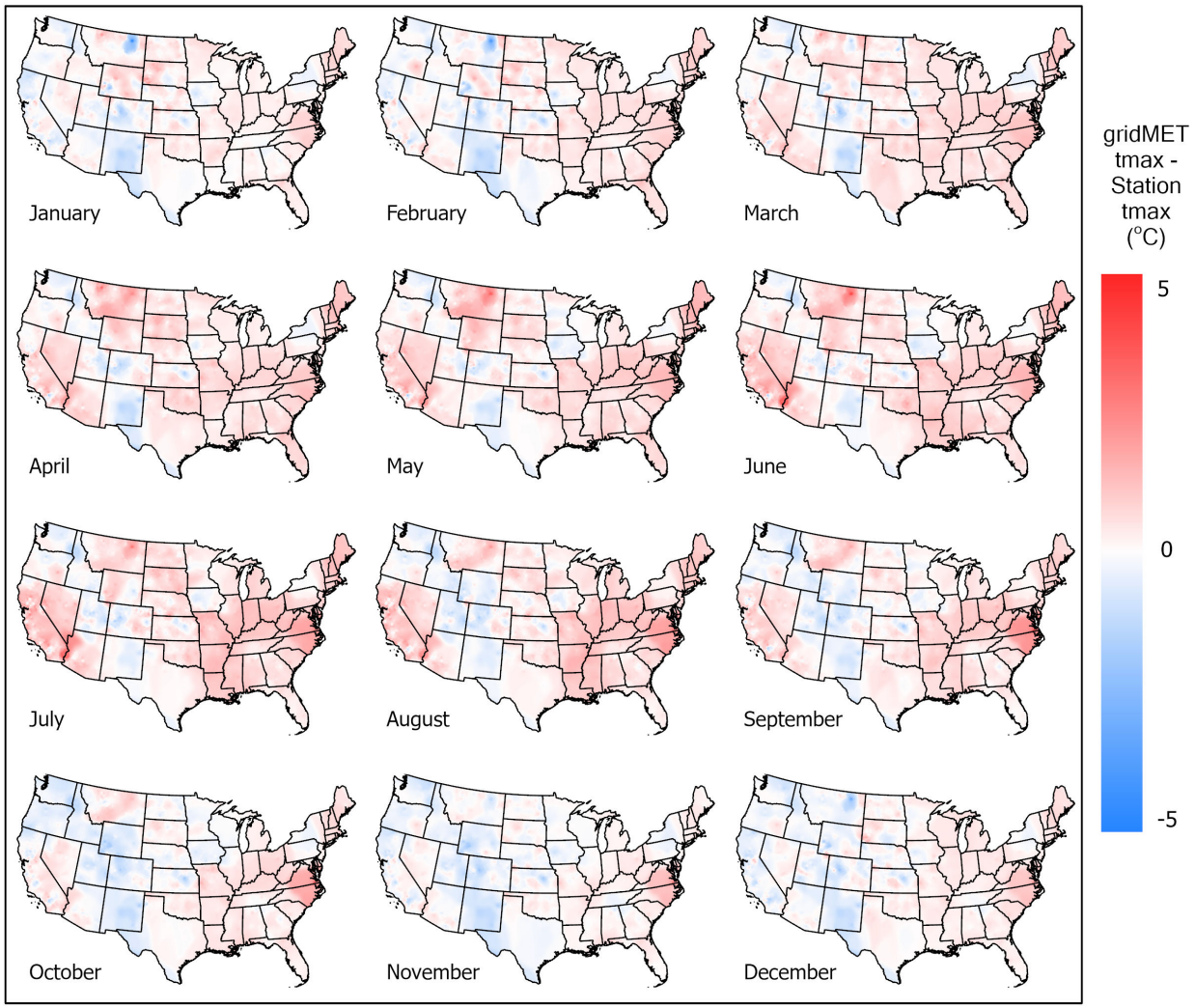

Supplementary Figure 7. Spatially interpolated monthly average gridMET maximum air temperature (tmax) difference relative to tmax measured at agricultural weather stations

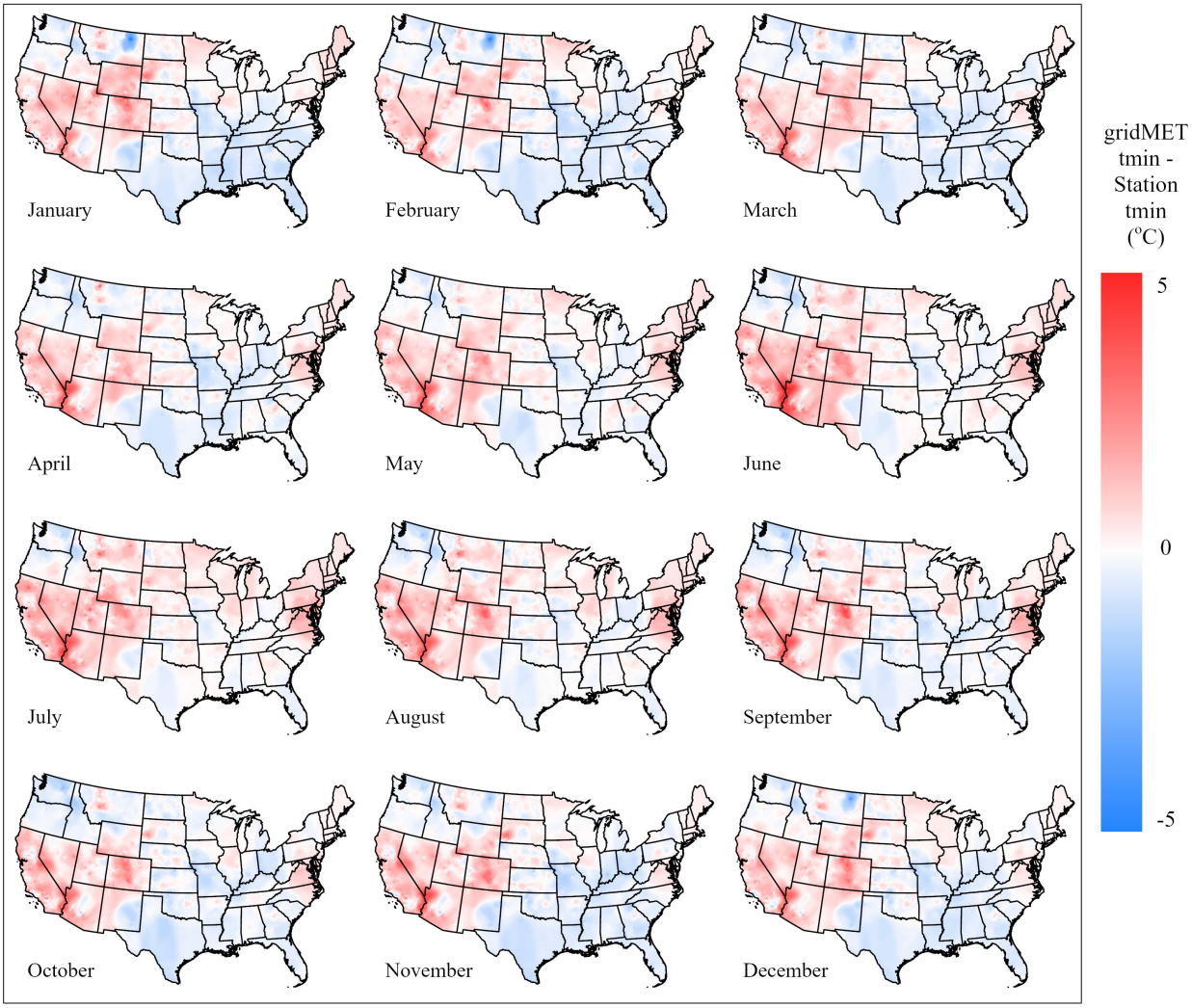

Supplementary Figure 8. Spatially interpolated monthly average gridMET minimum air temperature (tmin) difference relative to tmin measured at agricultural.

(a)

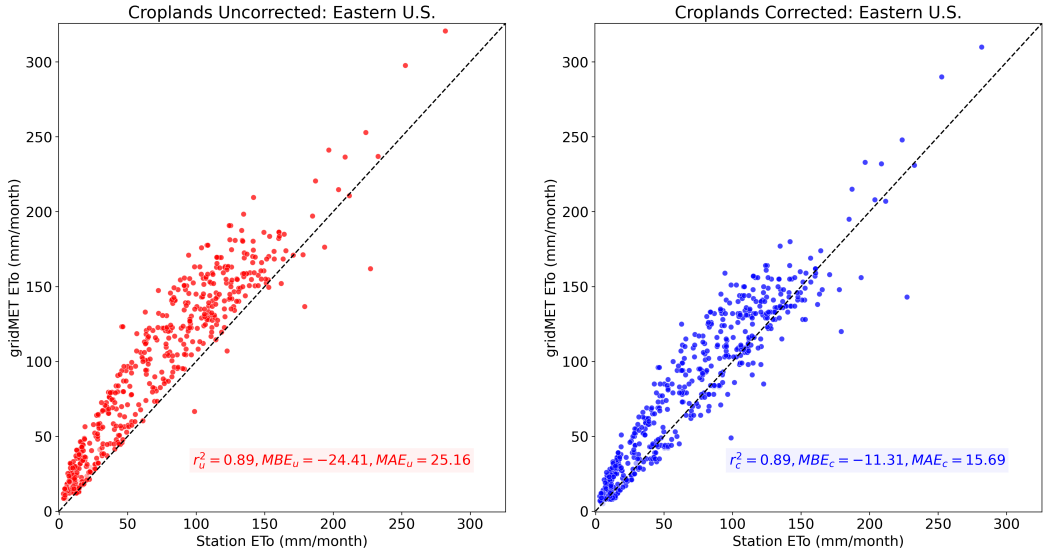

(b)

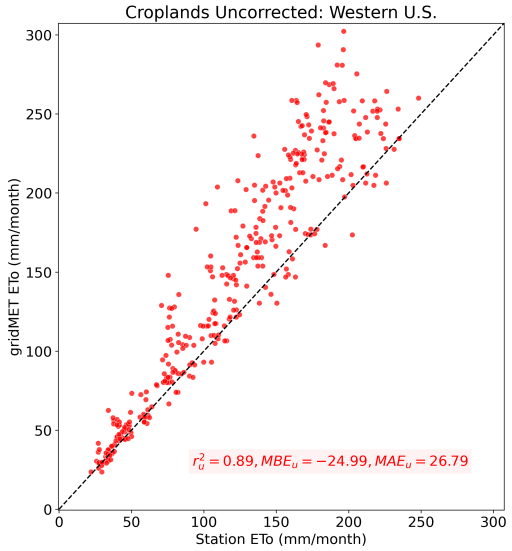
Croplands Uncorrected: Western U.S.
gridMET ETo (mm/month)
Station ETo (mm/month)
$r_u^2 = 0.89, MBE_u = -24.99, MAE_u = 26.79$

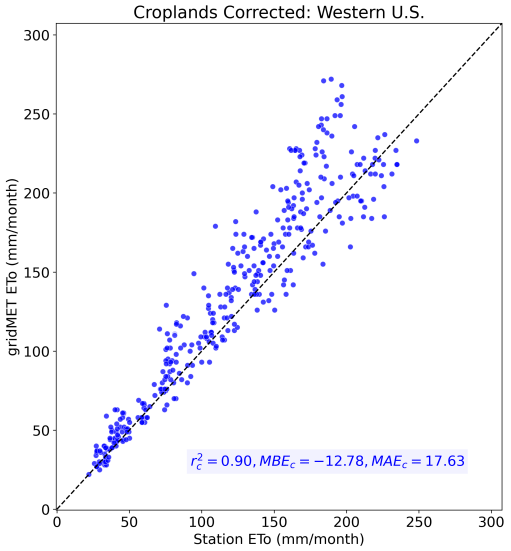
Croplands Corrected: Western U.S.
gridMET ETo (mm/month)
Station ETo (mm/month)
$r_c^2 = 0.90, MBE_c = -12.78, MAE_c = 17.63$

(c)

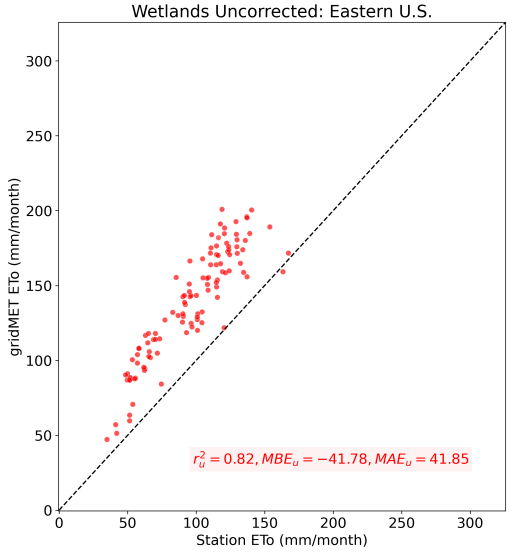
Wetlands Uncorrected: Eastern U.S.
gridMET ETo (mm/month)
Station ETo (mm/month)
$r_u^2 = 0.82, MBE_u = -41.78, MAE_u = 41.85$

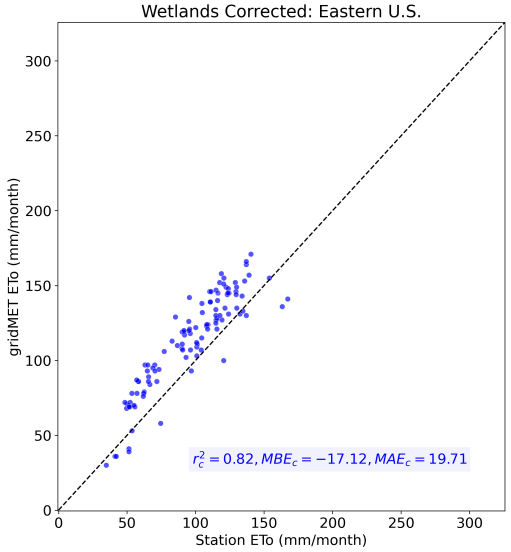
Wetlands Corrected: Eastern U.S.
gridMET ETo (mm/month)
Station ETo (mm/month)
$r_c^2 = 0.82, MBE_c = -17.12, MAE_c = 19.71$

(d)

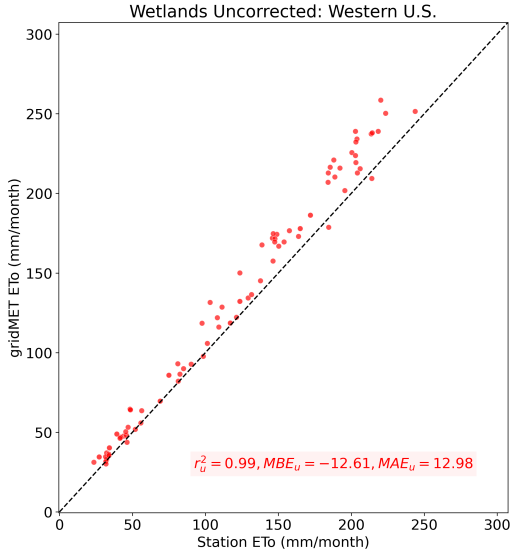
Wetlands Uncorrected: Western U.S.
gridMET ETo (mm/month)
Station ETo (mm/month)
$r_u^2 = 0.99, MBE_u = -12.61, MAE_u = 12.98$

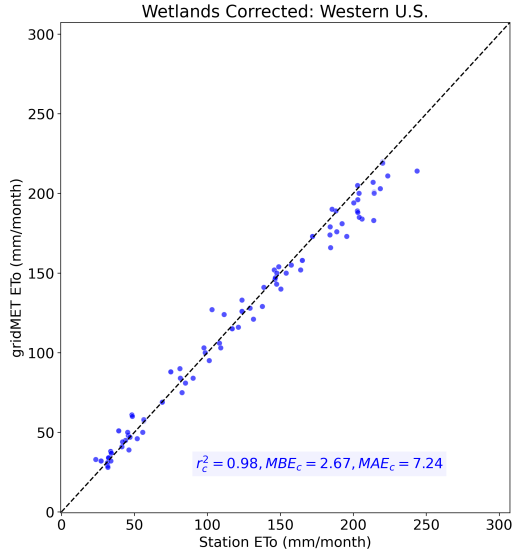
Wetlands Corrected: Western U.S.
gridMET ETo (mm/month)
Station ETo (mm/month)
$r_c^2 = 0.98, MBE_c = 2.67, MAE_c = 7.24$

(e)

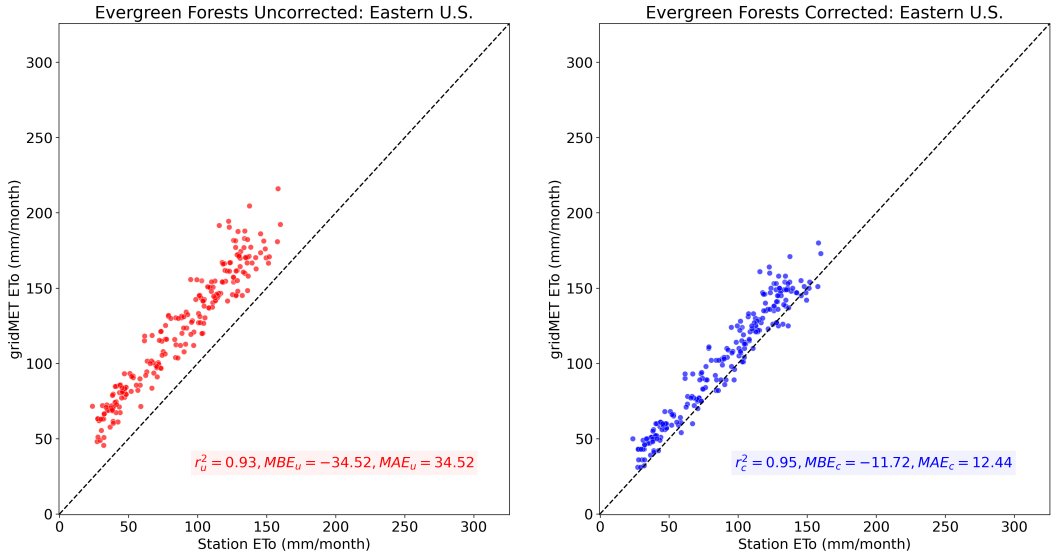
Evergreen Forests Uncorrected: Eastern U.S.
gridMET ETo (mm/month)
Station ETo (mm/month)
$r_u^2 = 0.93, MBE_u = -34.52, MAE_u = 34.52$

Evergreen Forests Corrected: Eastern U.S.
gridMET ETo (mm/month)
Station ETo (mm/month)
$r_c^2 = 0.95, MBE_c = -11.72, MAE_c = 12.44$

(f)

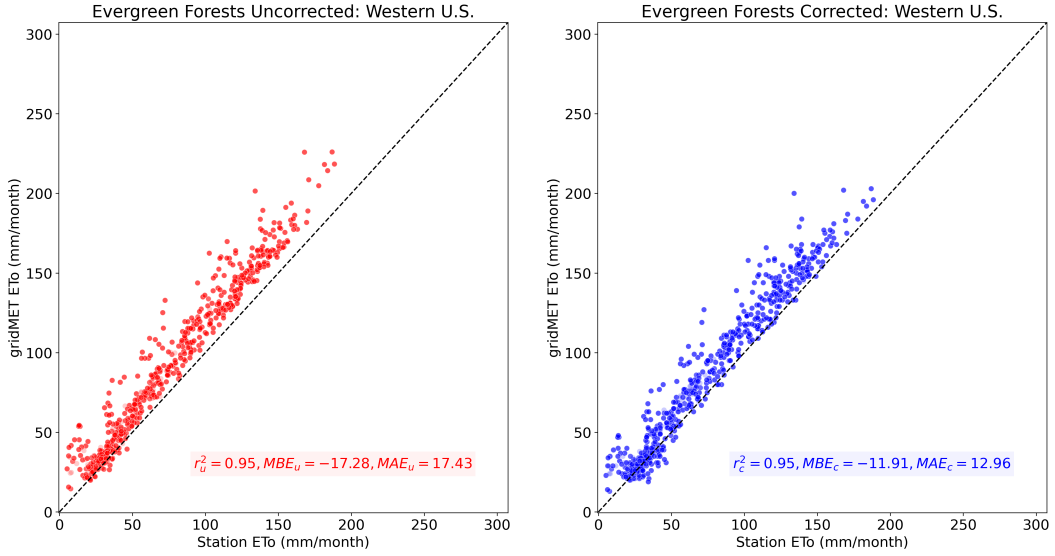
Evergreen Forests Uncorrected: Western U.S.
gridMET ETo (mm/month)
Station ETo (mm/month)
$r_u^2 = 0.95, MBE_u = -17.28, MAE_u = 17.43$

Evergreen Forests Corrected: Western U.S.
gridMET ETo (mm/month)
Station ETo (mm/month)
$r_c^2 = 0.95, MBE_c = -11.91, MAE_c = 12.96$

(g)

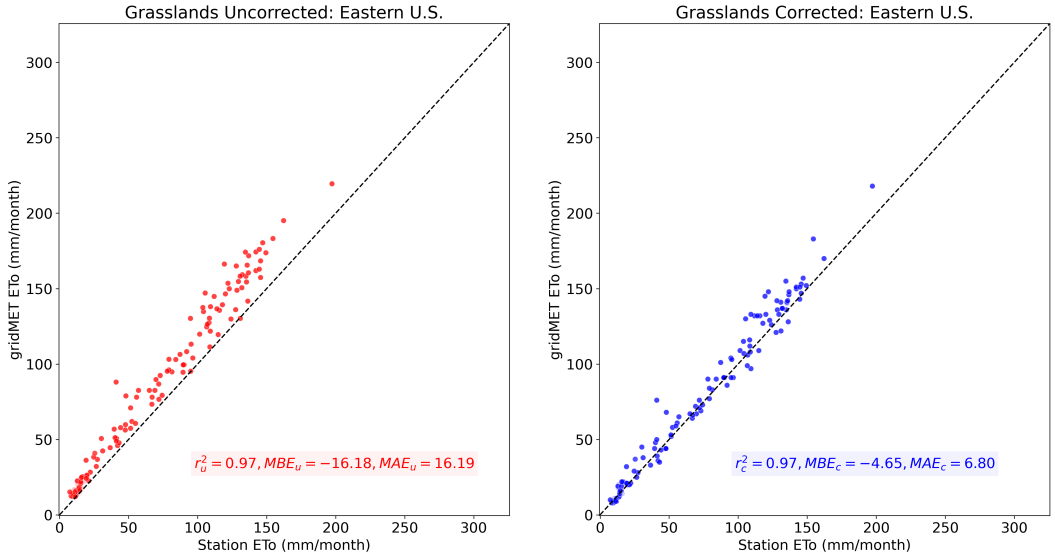
Grasslands Uncorrected: Eastern U.S.
gridMET ETo (mm/month)
Station ETo (mm/month)
$r_u^2 = 0.97, MBE_u = -16.18, MAE_u = 16.19$

Grasslands Corrected: Eastern U.S.
gridMET ETo (mm/month)
Station ETo (mm/month)
$r_c^2 = 0.97, MBE_c = -4.65, MAE_c = 6.80$

(h)

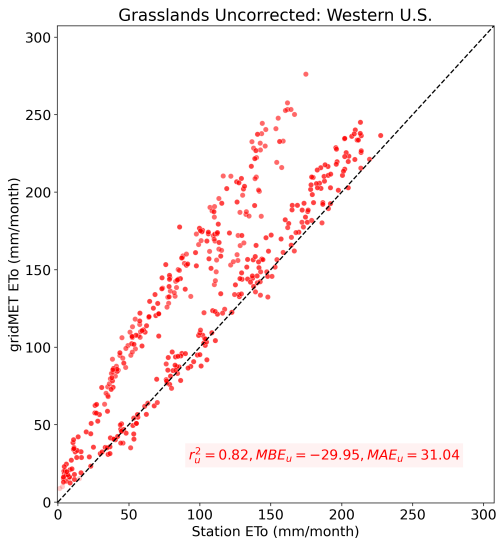
Grasslands Uncorrected: Western U.S.
gridMET ETo (mm/month)
Station ETo (mm/month)
$r_u^2 = 0.82, MBE_u = -29.95, MAE_u = 31.04$

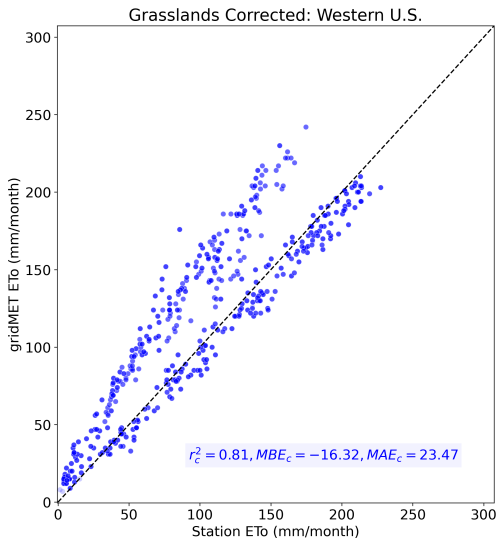
Grasslands Corrected: Western U.S.
gridMET ETo (mm/month)
Station ETo (mm/month)
$r_c^2 = 0.81, MBE_c = -16.32, MAE_c = 23.47$

(i)

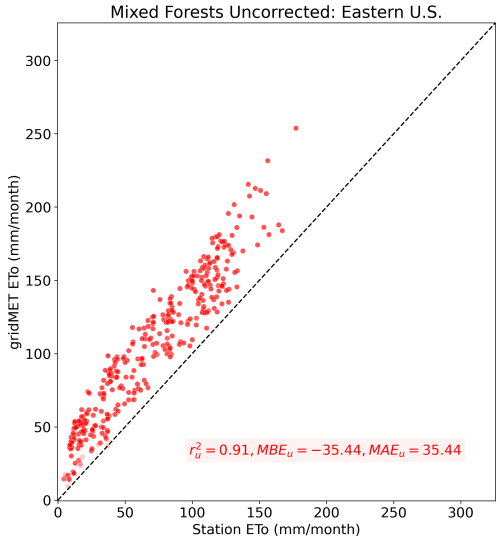
Mixed Forests Uncorrected: Eastern U.S.
gridMET ETo (mm/month)
Station ETo (mm/month)
$r_u^2 = 0.91, MBE_u = -35.44, MAE_u = 35.44$

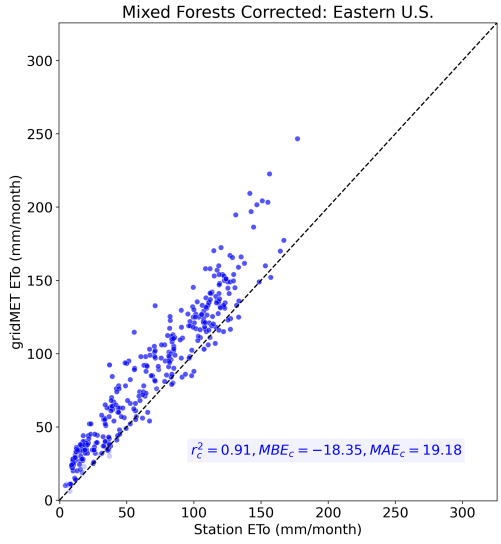
Mixed Forests Corrected: Eastern U.S.
gridMET ETo (mm/month)
Station ETo (mm/month)
$r_c^2 = 0.91, MBE_c = -18.35, MAE_c = 19.18$

(j)

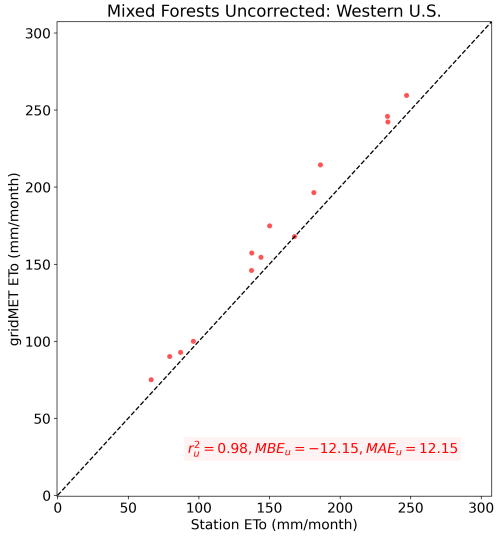
Mixed Forests Uncorrected: Western U.S.
gridMET ETo (mm/month)
Station ETo (mm/month)
$r_u^2 = 0.98, MBE_u = -12.15, MAE_u = 12.15$

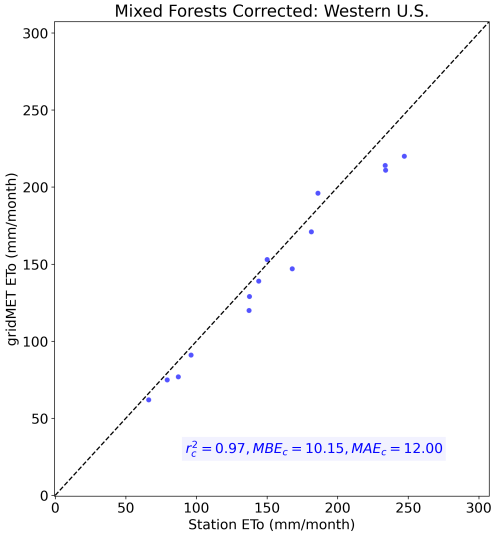
Mixed Forests Corrected: Western U.S.
gridMET ETo (mm/month)
Station ETo (mm/month)
$r_c^2 = 0.97, MBE_c = 10.15, MAE_c = 12.00$

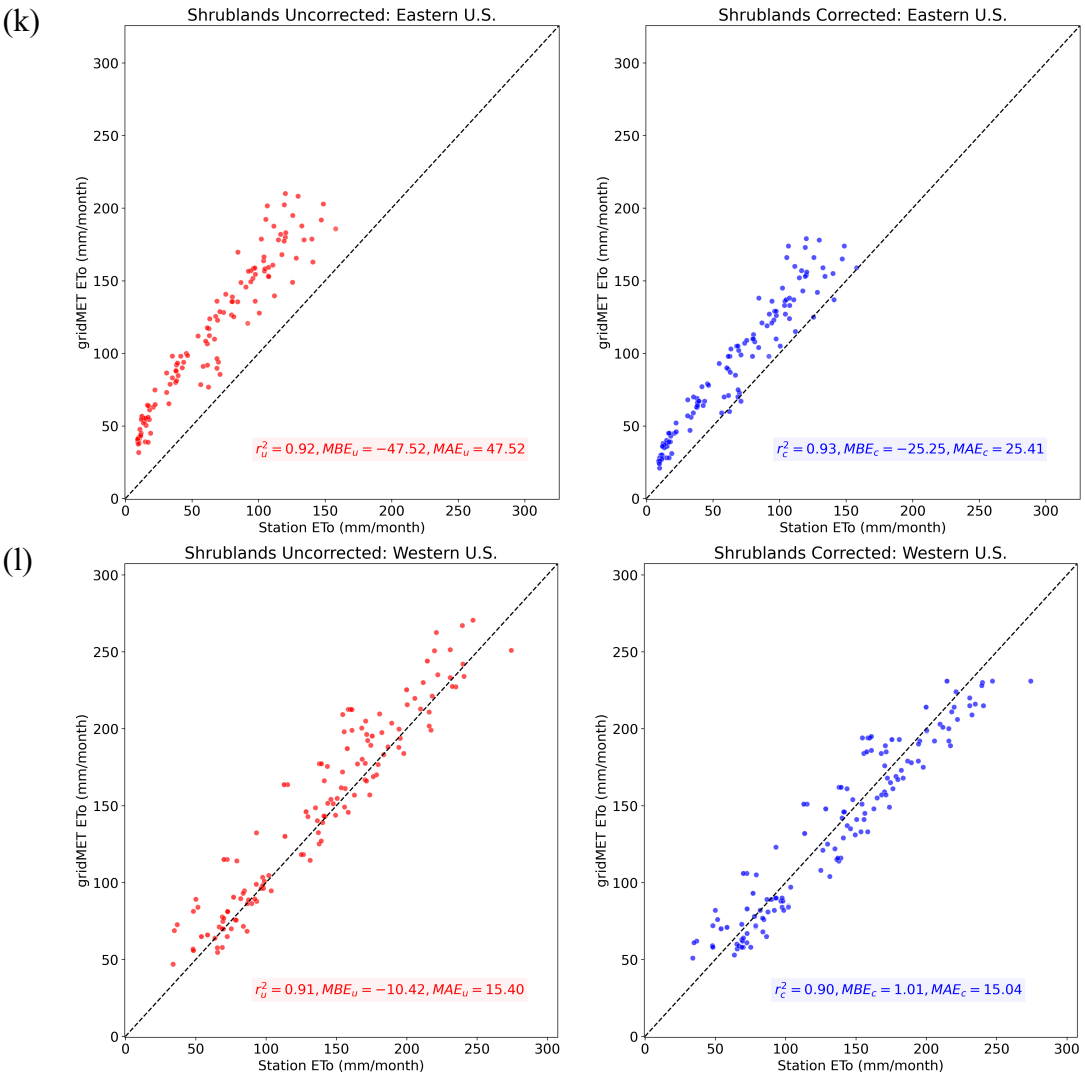

Supplementary Figure 9. Scatter plots of uncorrected and bias-corrected monthly gridMET ETo across different land covers: (a)-(b) croplands, (c)-(d) wetlands, (e)-(f) evergreen forests, (g)-(h) grasslands, (i)-(j) mixed forests, and (k)-(l) shrublands). (a), (c), (e), (g), (i), and (k) are for the eastern U.S. (distinguished by the 100th meridian), with the remaining scatter plots showing results over the western U.S. The subscripts 'u' and 'c' denote the error metrics for the uncorrected and bias-corrected ETo, respectively.

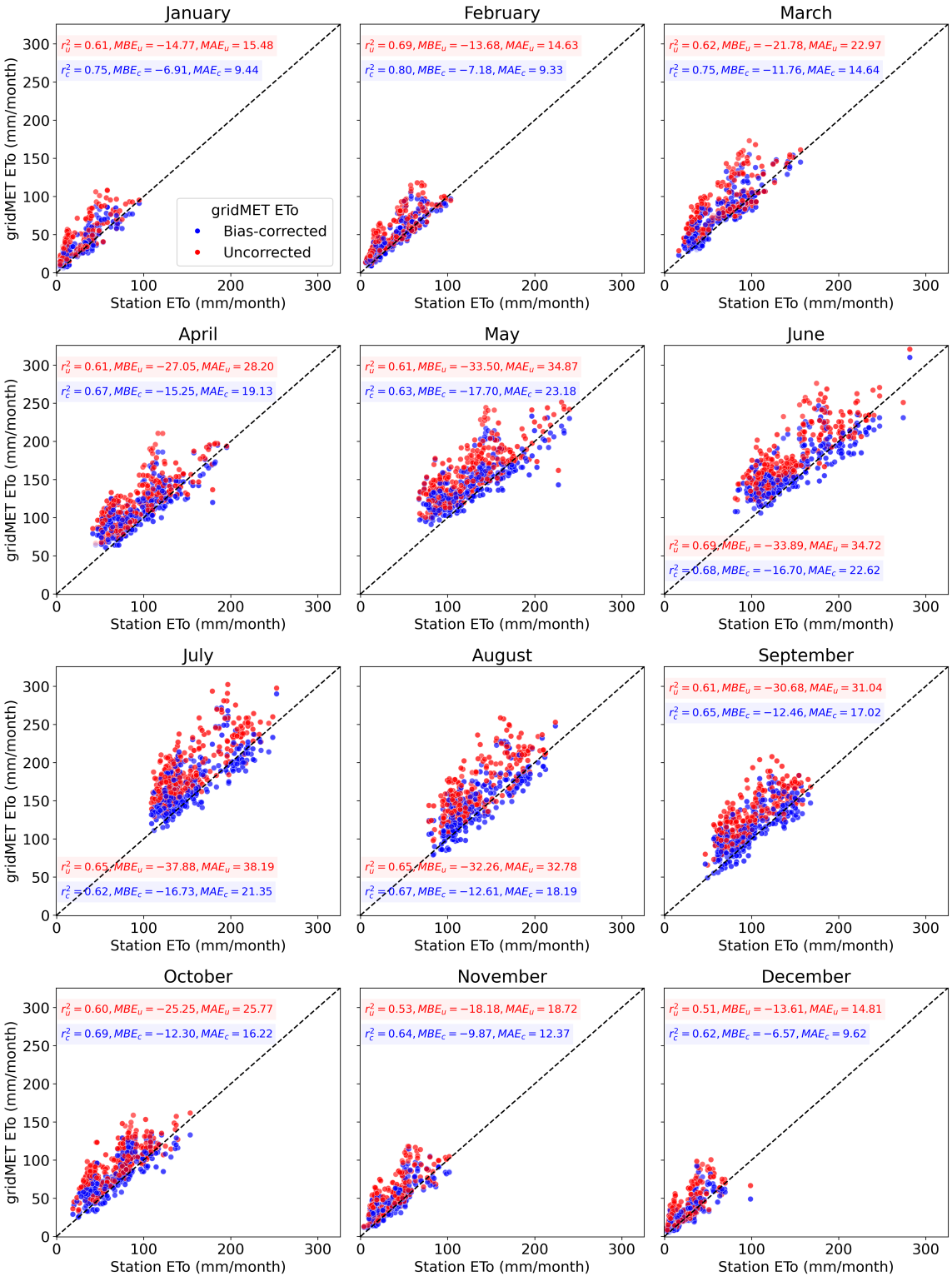

Supplementary Figure 10. Scatter plots of uncorrected and bias-corrected gridMET ETo across all land covers (croplands, evergreen forests, mixed forests, grasslands, shrublands, and wetlands) for each calendar month. The subscripts 'u' and 'c' denote the error metrics for the uncorrected and bias-corrected ETo, respectively.

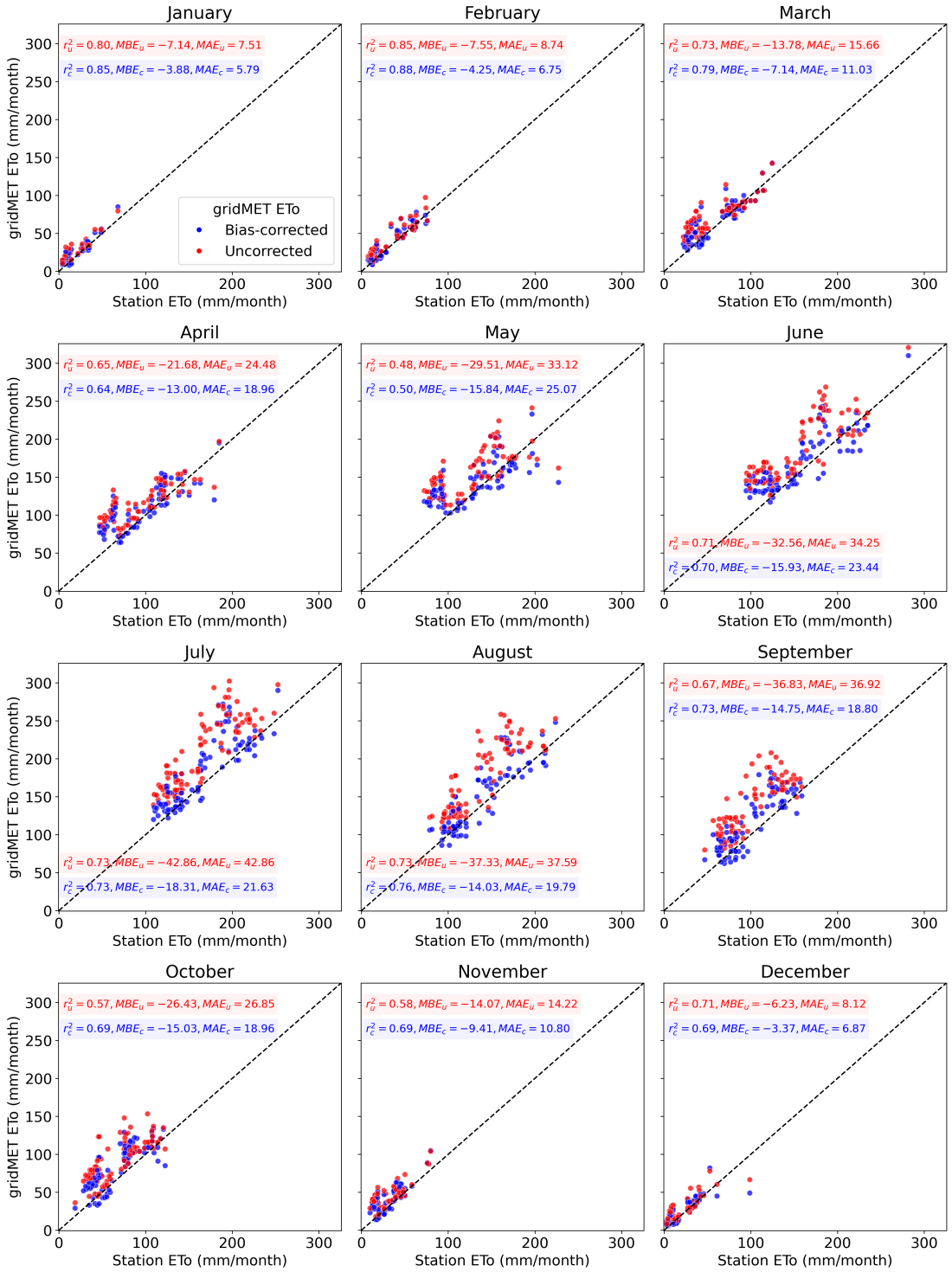

Supplementary Figure 11. Scatter plots of uncorrected and bias-corrected gridMET ETo across croplands for each calendar month. The subscripts 'u' and 'c' denote the error metrics for the uncorrected and bias-corrected ETo, respectively.

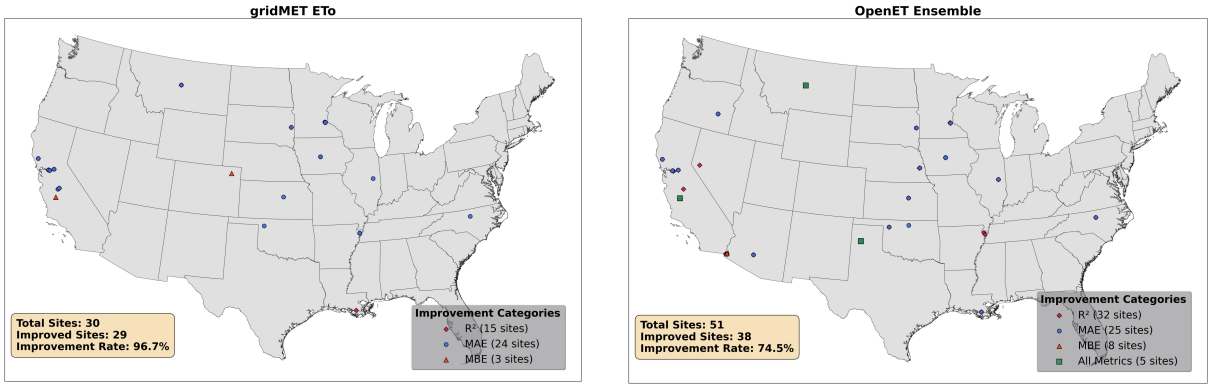

(a)

(b)

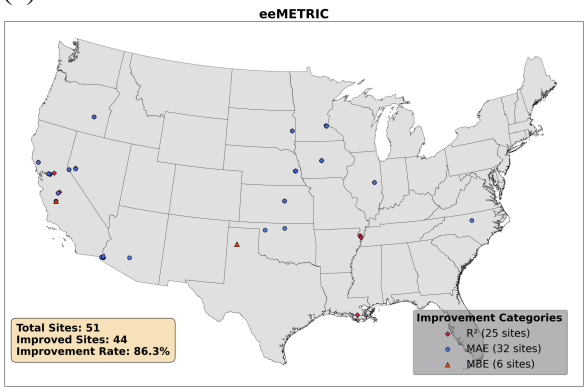

(c)

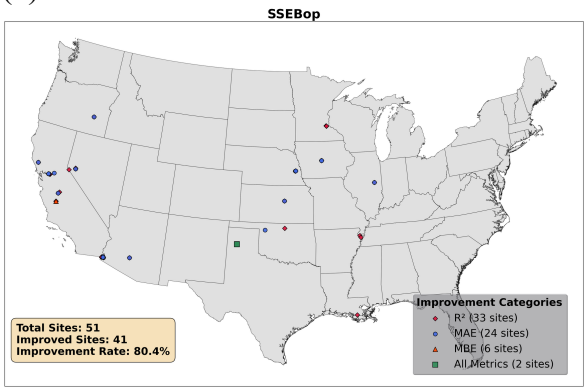

(d)

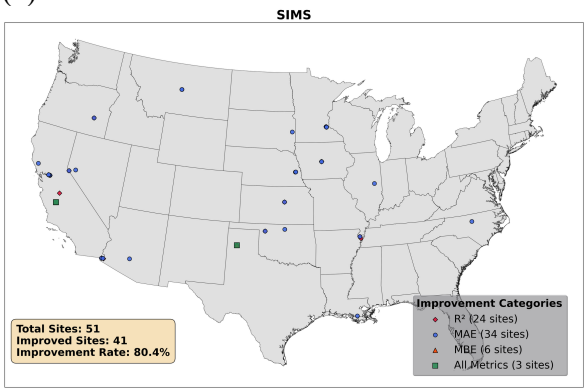

(e)

Supplementary Figure 12. Improved cropland sites for monthly (a) gridMET ETo, (b) OpenET ensemble, (c) eeMETRIC, (d) SSEBop, and (e) SIMS ET. The number of available cropland sites vary for the ETo and ET analysis because of the unavailability of required data for computing ASCE Penman Monteith ETo at certain flux sites. Note that the number of improved sites includes sites where one or more error metrics or a combination of error metrics improved.

Supplementary Figure 13. Improved cropland sites for monthly (a) gridMET ETo, (b) OpenET ensemble, (c) eeMETRIC, (d) SSEBop, and (e) SIMS ET. These are for the intersecting 29 cropland sites where ASCE Penman Monteith ETo and closed flux ET were both calculated. Note that the number of improved sites includes sites where one or more error metrics or a combination of error metrics improved.

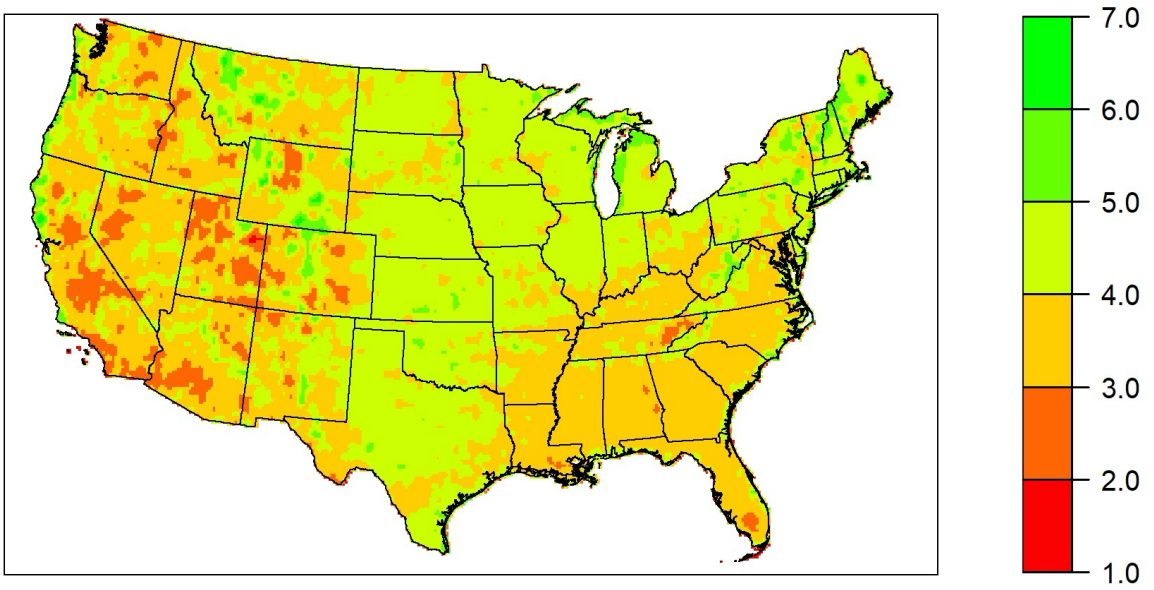

Supplementary Figure 14. Average annual 10 m wind speed (m/s) from gridMET for 1979-2024 calculated using Climate Engine (Huntington et al., 2017).

Supplementary Table 1A. Core metadata. Metadata for 79 eddy covariance sites with monthly ASCE ETo data availability. Split into three panels to keep columns within page width: 1A (Core metadata), 1B (Location and land-cover details), 1C (Contacts and citations). Note that the thirteen shaded sites (11 in CA and 2 in MT) are located over irrigated croplands as observed from the LANID and IrrMapper datasets. All the CA cropland sites show 100% irrigation fractions, whereas the ones in MT show < 5% irrigation. See Supplementary Discussion 1 for details on irrigation fraction computation.

Site ID	General classification	State	Data source/network	Period of record	Energy balance	Measurement technique	Land cover type
Almond_High	Croplands	CA	USDA-ARS	10/2016-10/2019	0.83	Eddy covariance	Orchards
Almond_Low	Croplands	CA	USDA-ARS	10/2016-10/2019	0.84	Eddy covariance	Orchards
Almond_Med	Croplands	CA	USDA-ARS	09/2016-10/2019	0.82	Eddy covariance	Orchards
BAR012	Croplands	CA	USDA-ARS GRAPEX	05/2017-11/2018	0.85	Eddy covariance	Vineyards
Ellendale	Croplands	LA	Delta-Flux	8/2018-12/2020	0.77	Eddy covariance	Annual crops
RIP760	Croplands	CA	USDA-ARS GRAPEX	05/2017-11/2018	0.88	Eddy covariance	Vineyards
SLM001	Croplands	CA	USDA-ARS GRAPEX	01/2017-11/2018	0.94	Eddy covariance	Vineyards
US-AR1	Croplands	OK	AmeriFlux	06/2009-12/2012	1.09	Eddy covariance	Annual crops
US-ARb	Grasslands	OK	AmeriFlux	03/2005-10/2006	1.01	Eddy covariance	Grasslands
US-ARc	Grasslands	OK	AmeriFlux	03/2005-10/2006	1.02	Eddy covariance	Grasslands
US-Aud	Grasslands	AZ	AmeriFlux	06/2002-09/2011	1.14	Eddy covariance	Grasslands
US-Bi1	Croplands	CA	AmeriFlux	08/2016-12/2019	0.78	Eddy covariance	Annual crops
US-Bi2	Croplands	CA	AmeriFlux	04/2017-07/2020	0.8	Eddy covariance	Annual crops
US-Bkg	Croplands	SD	AmeriFlux	04/2004-03/2010	0.99	Eddy covariance	Annual crops
US-Blk	Evergreen Forests	SD	AmeriFlux	01/2004-04/2008	0.94	Eddy covariance	Evergreen Forests
US-Bo1	Croplands	IL	AmeriFlux	08/1996-04/2008	0.84	Eddy covariance	Annual crops
US-Br1	Croplands	IA	AmeriFlux	04/2005-11/2011	0.81	Eddy covariance	Annual crops
US-Br3	Croplands	IA	AmeriFlux	01/2005-11/2011	0.81	Eddy covariance	Annual crops
US-Ced	Shrublands	NJ	AmeriFlux	07/2005-12/2014	1.08	Eddy covariance	Shrublands
US-Ctn	Grasslands	SD	AmeriFlux	11/2006-09/2009	0.71	Eddy covariance	Grasslands
US-Dix	Mixed Forests	NJ	AmeriFlux	04/2005-04/2008	1.06	Eddy covariance	Mixed Forests
US-Dk1	Croplands	NC	AmeriFlux	01/2006-11/2008	0.87	Eddy covariance	Annual crops
US-Dk2	Mixed Forests	NC	AmeriFlux	07/2006-04/2008	0.89	Eddy covariance	Mixed Forests
US-Esm	Wetland/Riparian	FL	AmeriFlux	01/2008-11/2013	0.8	Eddy covariance	Wetlands
US-FPe	Grasslands	MT	AmeriFlux	01/2000-06/2008	1.07	Eddy covariance	Grasslands
US-FR2	Mixed Forests	TX	AmeriFlux	01/2005-12/2007	0.78	Eddy covariance	Mixed Forests
US-Fmf	Evergreen Forests	AZ	AmeriFlux	08/2005-12/2010	0.83	Eddy covariance	Evergreen Forests
US-Fuf	Evergreen Forests	AZ	AmeriFlux	09/2005-12/2010	0.96	Eddy covariance	Evergreen Forests
US-Fwf	Grasslands	AZ	AmeriFlux	06/2005-12/2010	0.97	Eddy covariance	Grasslands
US-GLE	Evergreen Forests	WY	AmeriFlux	01/1999-03/2018	0.73	Eddy covariance	Evergreen Forests
US-Jo2	Shrublands	NM	AmeriFlux	08/2010-12/2019	0.8	Eddy covariance	Shrublands
US-KLS	Croplands	KS	AmeriFlux	12/2014-12/2016	0.78	Eddy covariance	Annual crops

US-KM4	Grasslands	MI	AmeriFlux	07/2010-12/2018	0.78	Eddy covariance	Grasslands
US-KS2	Shrublands	FL	AmeriFlux	04/2000-09/2006	0.81	Eddy covariance	Shrublands
US-Me5	Evergreen Forests	OR	AmeriFlux	01/2000-12/2002	0.76	Eddy covariance	Evergreen Forests
US-Mj1	Croplands	MT	AmeriFlux	04/2013-09/2014	0.94	Eddy covariance	Annual crops
US-Mj2	Croplands	MT	AmeriFlux	04/2014-09/2014	1.03	Eddy covariance	Annual crops
US-NC2	Evergreen Forests	NC	AmeriFlux	01/2005-12/2019	1.09	Eddy covariance	Evergreen Forests
US-NC3	Evergreen Forests	NC	AmeriFlux	03/2013-11/2019	1.07	Eddy covariance	Evergreen Forests
US-NC4	Wetland/Riparian	NC	AmeriFlux	02/2009-12/2019	1.1	Eddy covariance	Wetlands
US-NR1	Evergreen Forests	CO	AmeriFlux	06/1999-12/2019	0.81	Eddy covariance	Evergreen Forests
US-OF1	Croplands	AR	Delta-Flux	5/2017-9/2017	0.84	Eddy covariance	Annual crops
US-OF2	Croplands	AR	Delta-Flux	6/2017-9/2017	0.76	Eddy covariance	Annual crops
US-OF4	Croplands	AR	Delta-Flux	5/2018-8/2018	0.89	Eddy covariance	Annual crops
US-OF6	Croplands	AR	Delta-Flux	5/2018-8/2018	0.78	Eddy covariance	Annual crops
US-Ro1	Croplands	MN	AmeriFlux	01/2011-12/2016	0.78	Eddy covariance	Annual crops
US-Ro2	Croplands	MN	AmeriFlux	01/2016-12/2016	0.76	Eddy covariance	Annual crops
US-Ro4	Grasslands	MN	AmeriFlux	09/2015-06/2020	0.83	Eddy covariance	Grasslands
US-Ro5	Croplands	MN	AmeriFlux	03/2017-12/2017	0.77	Eddy covariance	Annual crops
US-Ro6	Croplands	MN	AmeriFlux	03/2017-12/2017	0.8	Eddy covariance	Annual crops
US-SO2	Shrublands	CA	AmeriFlux	03/1997-12/2006	0.99	Eddy covariance	Shrublands
US-SO3	Shrublands	CA	AmeriFlux	03/1997-12/2006	0.9	Eddy covariance	Shrublands
US-SO4	Shrublands	CA	AmeriFlux	01/2004-12/2006	0.87	Eddy covariance	Shrublands
US-SP2	Evergreen Forests	FL	AmeriFlux	02/1999-07/2008	0.89	Eddy covariance	Evergreen Forests
US-SP3	Evergreen Forests	FL	AmeriFlux	01/1999-12/2010	0.85	Eddy covariance	Evergreen Forests
US-SRC	Mixed Forests	AZ	AmeriFlux	03/2008-06/2014	0.82	Eddy covariance	Mixed Forests
US-SRS	Shrublands	AZ	AmeriFlux	05/2011-11/2018	0.94	Eddy covariance	Shrublands
US-SdH	Grasslands	NE	AmeriFlux	05/2004-12/2009	1.04	Eddy covariance	Grasslands
US-Skr	Wetland/Riparian	FL	AmeriFlux	01/2004-08/2011	0.93	Eddy covariance	Wetlands
US-Slt	Mixed Forests	NJ	AmeriFlux	01/2005-12/2014	1.08	Eddy covariance	Mixed Forests
US-Sne	Wetland/Riparian	CA	AmeriFlux	05/2016-12/2019	0.85	Eddy covariance	Wetlands
US-Srr	Wetland/Riparian	CA	AmeriFlux	03/2016-10/2017	0.86	Eddy covariance	Wetlands
US-Tw2	Croplands	CA	AmeriFlux	05/2012-04/2013	0.77	Eddy covariance	Annual crops
US-Tw3	Croplands	CA	AmeriFlux	05/2013-06/2018	0.85	Eddy covariance	Annual crops
US-Twt	Croplands	CA	AmeriFlux	04/2009-04/2017	0.9	Eddy covariance	Annual crops
US-Var	Grasslands	CA	AmeriFlux	10/2000-08/2020	0.94	Eddy covariance	Grasslands
US-WBW	Mixed Forests	TN	AmeriFlux	01/1995-06/2007	0.75	Eddy covariance	Mixed Forests
US-WCr	Mixed Forests	WI	AmeriFlux	02/1999-04/2020	0.89	Eddy covariance	Mixed Forests
US-xAE	Grasslands	OK	AmeriFlux	02/2018-05/2020	0.76	Eddy covariance	Grasslands
US-xDC	Grasslands	ND	AmeriFlux	10/2017-05/2020	0.74	Eddy covariance	Grasslands
US-xDL	Mixed Forests	AL	AmeriFlux	01/2017-05/2020	0.83	Eddy covariance	Mixed Forests
US-xDS	Grasslands	FL	AmeriFlux	01/2018-05/2020	0.75	Eddy covariance	Grasslands

US-xJR	Shrublands	NM	AmeriFlux	11/2017-05/2020		Eddy covariance	Shrublands
US-xNG	Grasslands	ND	AmeriFlux	10/2017-04/2020	0.71	Eddy covariance	Grasslands
US-xRM	Evergreen Forests	CO	AmeriFlux	06/2017-05/2020	0.65	Eddy covariance	Evergreen Forests
US-xSL	Croplands	CO	AmeriFlux	06/2017-05/2020	0.78	Eddy covariance	Annual crops
US-xST	Mixed Forests	WI	AmeriFlux	08/2018-05/2020	0.77	Eddy covariance	Mixed Forests
US-xUN	Mixed Forests	MI	AmeriFlux	08/2017-05/2020	0.74	Eddy covariance	Mixed Forests
US-xYE	Evergreen Forests	WY	AmeriFlux	10/2018-05/2020		Eddy covariance	Evergreen Forests

Supplementary Table 1B. Location and land-cover details.

Site ID	Latitude (°)	Longitude (°)	Elevation (m)	Land cover details
Almond_High	36.169669	-120.201004	147.0	Almond
Almond_Low	36.946608	-120.10237	78.0	Almond
Almond_Med	36.177669	-120.20264	147.0	Almond
BAR012	38.751	-122.975	102.0	Vineyard
Ellendale	29.633321	-90.827662	2.0	Sugarcane
RIP760	36.839	-120.21	57.0	Vineyard
SLM001	38.289	-121.118	39.0	Vineyard
US-AR1	36.4267	-99.42	611.0	Planted Switchgrass
US-ARb	35.5497	-98.0402	424.0	Native tallgrass prairie
US-ARc	35.54649	-98.04	424.0	Native tallgrass prairie (burned in March 2005)
US-Aud	31.5907299999999	-110.51038	1469.0	Madrean mixed grass prairie
US-Bi1	38.0991537999999	-121.49933	-2.7	Alfalfa
US-Bi2	38.109	-121.535	-4.98	Corn
US-Bkg	44.34529	-96.83617	510.0	Native grass pasture
US-Blk	44.158	-103.65	1718.0	Ponderosa pine
US-Bo1	40.0062	-88.2904	219.0	Corn (2005, 2007) and soy rotation (2006, 2008), no-till
US-Br1	41.9749	-93.6906	313.0	Corn and soy rotation
US-Br3	41.97472	-93.69357	313.0	Corn and soy rotation
US-Ced	39.8379	-74.3791	58.0	Pitch pine prescribed burns
US-Ctn	43.95	-101.8466	744.0	Grasslands
US-Dix	39.97123	-74.43455	48.0	Oak/pine forest
US-Dk1	35.9712	-79.09338	168.0	Grass (Festuca arundinacea)
US-Dk2	35.97358	-79.10043	168.0	Mature oak-hickory forest
US-Esm	25.4379	-80.5946	1.07	Everglades peat and marl forming wetlands
US-FPe	48.3077	-105.1019	634.0	Grassland
US-FR2	29.94949	-97.99623	271.9	Mesquite Juniper forest
US-Fmf	35.1426	-111.7273	2160.0	Ponderosa pine forest
US-Fuf	35.089	-111.762	2180.0	Ponderosa pine forest, non-disturbed
US-Fwf	35.4454	-111.7718	2270.0	Grassland, after severe fire removed ponderosa pine in 1996

US-GLE	41.36653	-106.2399	3197.0	85% Engelmann spruce 15% Subalpine fir
US-Jo2	32.58494	-106.60322	1469.0	Open phreatophyte shrubland
US-KLS	38.7745	-97.5684	373.0	Wheatgrass
US-KM4	42.44225	-85.330056	288.0	Smooth brome grass
US-KS2	28.6086	-80.6715	3.0	Scrub oak, fire in 1996
US-Me5	44.43719	-121.56676	1188.0	Ponderosa pine forest, clearcut in 1978
US-Mj1	46.99475	-109.61375	1285.0	Wheat
US-Mj2	46.9957	-109.6295	1277.0	Summer fallow
US-NC2	35.803	-76.6685	5.0	Loblolly pine plantation
US-NC3	35.799	-76.656	5.0	Loblolly pine forest, planted after clearcut in 2012
US-NC4	35.7879	-75.9038	1.0	Forested wetland
US-NR1	40.0329	-105.5464	3050.0	Subalpine fir, Engelmann spruce, and lodgepole pine
US-OF1	35.737066999999	-90.0492	70.0	Rice
US-OF2	35.7406	-90.0489	70.0	Rice
US-OF4	35.734346	-90.037982	71.0	Rice
US-OF6	35.729972	-90.04033	70.0	Rice
US-Ro1	44.7143	-93.0898	260.0	Agricultural, corn and soybean rotation
US-Ro2	44.7288	-93.0888	292.0	Corn-Soybean-Kura Clover annual rotation
US-Ro4	44.6781	-93.0723	274.0	Restored prarie, Andropogon gerardii, Sorghastrum nutans, and Elymus canadensis
US-Ro5	44.691	-93.0576	283.0	Corn/soy rotation
US-Ro6	44.6946	-93.05776	282.0	Corn/soybean/clover rotation
US-SO2	33.3738	-116.6228	1394.0	Chaparral, severe fire in 2003
US-SO3	33.3771	-116.6226	1429.0	Chaparral, severe fire in 2003
US-SO4	33.3845	-116.6406	1429.0	Old-growth chaparral ecosystem
US-SP2	29.7648	-82.2448	50.0	Slash pine (Pinus elliottii) plantation, planted in Jan. 1999
US-SP3	29.75477	-82.16328	50.0	Even aged high density slash pine (Pinus elliottii) plantation.
US-SRC	31.9083	-110.8395	950.0	Greasewood
US-SRS	31.817294	-110.850801	1169.0	Mesquite savanna, herbicide applied in 2016
US-SdH	42.0693	-101.4072	1081.0	Grass pasture
US-Skr	25.362932999999	-81.07758	0.0	This is a tall (up to 20 m) mangrove forest.
US-Slt	39.9138	-74.596	30.0	Oak forest
US-Sne	38.0369	-121.7547	-5.0	Restored wetland
US-Srr	38.200556	-122.026358	8.0	Brackish tidal marsh
US-Tw2	38.1047	-121.6433	-5.0	Corn on peat soil
US-Tw3	38.1159	-121.6467	-9.0	Alfalfa
US-Twt	38.108720399999	-121.6531	-7.0	Rice
US-Var	38.4133	-120.9507	129.0	Annual grasses and forbs
US-WBW	35.95877	-84.28743	283.0	Oak/hickory broadleaf forest

US-WCr	45.8059	-90.0799	520.0	Sugar maple (Acer saccharum), basswood (Tilia americana), and yellow birch (Betula alleghaniensis).
US-xAE	35.41059	-99.05879	516.0	Grass pasture
US-xDC	47.16165	-99.10656	559.0	Prairie grasslands, mid- to tall-height
US-xDL	32.54172	-87.80389	22.0	Oak and hickory
US-xDS	28.12504	-81.4362	15.0	Native grasses and wetlands
US-xJR	32.59068	-106.84254	1329.0	Shrubland (Jornada LTER)
US-xNG	46.76972	-100.91535	578.0	Smooth Brome and Kentucky blue grass grassland
US-xRM	40.2759099999999	-105.54592	2743.0	Ponderosa pine, open canopy
US-xSL	40.4619	-103.0293	1364.0	Winter wheat, millet, and maize, no-till
US-xST	45.50894	-89.58637	481.0	Early successional, even-aged aspen stand, with some red maple and balsam fir
US-xUN	46.23388	-89.53725	518.0	Maple, aspen, birch mesic forest
US-xYE	44.95348	-110.53914	2116.0	Mosaic: pine forest with sage/grass openings (Yellowstone NR)

Supplementary Table 1C. Contacts and citations.

Site ID	Contact for sites not downloaded from AmeriFlux network	Contact email	DOI	Team member	Member role	Member institution	Member email	Site name
Almond_High	Ray Anderson	ray.anderson@usda.gov						
Almond_Low	Ray Anderson	ray.anderson@usda.gov						
Almond_Med	Ray Anderson	ray.anderson@usda.gov						
BAR012	William Kustas	bill.kustas@usda.gov						
Ellendale	Benjamin Runkle	brrunkle@uark.edu						
RIP760	William Kustas	bill.kustas@usda.gov						
SLM001	William Kustas	bill.kustas@usda.gov						
US-AR1			10.17190/AMF/1246137	Dave Billesbach	PI	University of Nebraska	dbillesbach1@unl.edu	ARM USDA UNL OSU Woodward Switchgrass 1
US-ARb			10.17190/AMF/1246025	Margaret Torn	PI	Lawrence Berkeley National Laboratory	mstorn@lbl.gov	ARM Southern Great Plains burn site-Lamont
US-ARc			10.17190/A	Margaret Torn	PI	Lawrence Berkeley	mstorn@lbl.gov	ARM Southern

			MF/12 46026			National Laboratory		Great Plains control site-Lamont
US-Aud			10.171 90/A MF/12 46028	Tilden Meyers	PI	NOAA/ARL	Tilden.Meyers@noaa.gov	Audubon Research Ranch
US-Bi1			10.171 90/A MF/14 80317	Dennis Baldocchi	PI	University of California, Berkeley	Baldocchi@berkeley.edu	Bouldin Island Alfalfa
US-Bi2			10.171 90/A MF/14 19513	Dennis Baldocchi	PI	University of California, Berkeley	baldocchi@berkeley.edu	Bouldin Island corn
US-Bkg			10.171 90/A MF/12 46040	Tilden Meyers	PI	NOAA/ARL	Tilden.Meyers@noaa.gov	Brookings
US-Blk			10.171 90/A MF/12 46031	Tilden Meyers	PI	NOAA/ARL	Tilden.Meyers@noaa.gov	Black Hills
US-Bo1			10.171 90/A MF/12 46036	Tilden Meyers	PI	NOAA/ARL	Tilden.Meyers@noaa.gov	Bondville
US-Br1			10.171 90/A MF/12 46038	John Prueger	PI	National Laboratory for Agriculture and the Environment	john.prueger@ars.usda.gov	Brooks Field Site 10-Ames
US-Br3			10.171 90/A MF/12 46039	John Prueger	PI	National Laboratory for Agriculture and the Environment	john.prueger@ars.usda.gov	Brooks Field Site 11-Ames
US-Ced			10.171 90/A MF/12 46043	Ken Clark	PI	USDA Forest Service	kennethclark@fs.fed.us	Cedar Bridge
US-Ctn			10.171 90/A MF/12 46117	Tilden Meyers	PI	NOAA/ARL	tilden.meyers@noaa.gov	Cottonwood
US-Dix			10.171 90/A MF/12 46045	Ken Clark	PI	USDA Forest Service	kennethclark@fs.fed.us	Fort Dix
US-Dk1			10.171 90/A MF/12 46046	Chris Oishi	PI	USDA Forest Service	christopher.oishi@gmail.com	Duke Forest-open field
US-Dk2			10.171 90/A MF/12 46047	A. Christopher Oishi	PI	USDA Forest Service	acoishi@fs.fed.us	Duke Forest-hardwoods
US-Esm			10.171 90/A	Gregory Starr	PI	University of Alabama	gstarr@bama.ua.edu	Everglades (short

			MF/12 46119					hydroperiod marsh)
US-FPe			10.171 90/A MF/12 46053	Tilden Meyers	PI	NOAA/AR L	Tilden.Meyers@noaa.gov	Fort Peck
US-FR2			10.171 90/A MF/12 46054	Marcy Litvak	PI	University of New Mexico	mlitvak@unm.edu	Freeman Ranch-Mesquite Juniper
US-Fmf			10.171 90/A MF/12 46050	Sabina Dore	PI	Northern Arizona University	Sabina.Dore@nau.edu	Flagstaff - Managed Forest
US-Fuf			10.171 90/A MF/12 46051	Sabina Dore	PI	Northern Arizona University	Sabina.Dore@nau.edu	Flagstaff - Unmanaged Forest
US-Fwf			10.171 90/A MF/12 46052	Sabina Dore	PI	Northern Arizona University	Sabina.Dore@nau.edu	Flagstaff - Wildfire
US-GLE			10.171 90/A MF/12 46056	Bill Massman	PI	USDA Forest Service	wmassman@fs.fed.us	GLEES
US-Jo2			10.171 90/A MF/16 17696	Enrique R. Vivoni	PI	Arizona State University	vivoni@asu.edu	Jornada Experimental Range Mixed Shrubland
US-KLS			10.171 90/A MF/14 98745	Nathaniel Brunsell	PI	Kansas University	brunsell@ku.edu	Kansas Land Institute
US-KM4			10.171 90/A MF/16 34882	G. Philip Robertson	PI	Michigan State University	robert30@msu.edu	KBS Marshall Farms Smooth Brome Grass (Ref)
US-KS2			10.171 90/A MF/12 46070	Bert Drake	PI	Smithsonian Environmental Research Center	drakeb@si.edu	Kennedy Space Center (scrub oak)
US-Me5			10.171 90/A MF/12 46079	Bev Law	PI	Oregon State University	bev.law@oregonstate.edu	Metolius-first young aged pine
US-Mj1			10.171 90/A MF/16 17715	Paul C. Stoy	PI	Montana State University	paul.stoy@montana.edu	Montana Judith Basin wheat field
US-Mj2			10.171 90/A MF/16 17716	Paul C. Stoy	PI	Montana State University	paul.stoy@montana.edu	Montana Judith Basin summer fallow field
US-NC2			10.171 90/A MF/12 46083	Asko Noormets	PI	Texas A&M University	noormets@tamu.edu	NC_Loblolly Plantation

US-NC3			10.17190/AMF/1419506	Asko Noormets	PI	Texas A&M University	noormets@tamu.edu	NC_Clearcut #3
US-NC4			10.17190/AMF/1480314	Asko Noormets	PI	Texas A&M University	noormets@tamu.edu	NC_Alligator River
US-NR1			10.17190/AMF/1246088	Peter Blanken	PI	University of Colorado	Blanken@Colorado.EDU	Niwot Ridge Forest (LTER NWT1)
US-OF1	Benjamin Runkle	brrunkle@uark.edu						
US-OF2	Benjamin Runkle	brrunkle@uark.edu						
US-OF4	Benjamin Runkle	brrunkle@uark.edu						
US-OF6	Benjamin Runkle	brrunkle@uark.edu						
US-Ro1			10.17190/AMF/1246092	John Baker	PI	USDA-ARS	john.baker@ars.usda.gov	Rosemount-G21
US-Ro2			10.17190/AMF/1418683	John Baker	PI	USDA-ARS	john.baker@ars.usda.gov	Rosemount-C7
US-Ro4			10.17190/AMF/1419507	John Baker	PI	USDA-ARS	John.Baker@ARS.USDA.GOV	Rosemount Prairie
US-Ro5			10.17190/AMF/1419508	John Baker	PI	USDA-ARS	john.baker@ars.usda.gov	Rosemount I18_South
US-Ro6			10.17190/AMF/1419509	John Baker	PI	USDA-ARS	john.baker@ars.usda.gov	Rosemount I18_North
US-SO2			10.17190/AMF/1246097	Walt Oechel	PI	San Diego State University	woechel@mail.sdsu.edu	Sky Oaks-Old Stand
US-SO3			10.17190/AMF/1246098	Walt Oechel	PI	San Diego State University	woechel@mail.sdsu.edu	Sky Oaks-Young Stand
US-SO4			10.17190/AMF/1246099	Walt Oechel	PI	San Diego State University	woechel@mail.sdsu.edu	Sky Oaks-New Stand
US-SP2			10.17190/AMF/1246101	Tim Martin	PI	University of Florida	tamartin@ufl.edu	Slashpine-Mize-clearcut-3yr,regen
US-SP3			10.17190/A	Tim Martin	PI	University of Florida	tamartin@ufl.edu	Slashpine-Donaldson-

			MF/12 46102					mid-rot-12yrs
US-SRC			10.17190/A MF/12 46127	Shirley Kurc	PI	University of Arizona	kurc@ag.arizona.edu	Santa Rita Creosote
US-SRS			10.17190/A MF/16 60351	Enrique R. Vivoni	PI	Arizona State University	vivoni@asu.edu	Santa Rita Experimental Range Mesquite Savanna
US-SdH			10.17190/A MF/12 46136	Dave Billesbach	PI	University of Nebraska	dbillesbach1@unl.edu	Nebraska SandHills Dry Valley
US-Skr			10.17190/A MF/12 46105	Sparkle Malone	PI	Pennsylvania State University	jdfuentes@psu.edu	Shark River Slough (Tower SRS-6) Everglades
US-Slt			10.17190/A MF/12 46096	Ken Clark	PI	USDA Forest Service	kennethclark@fs.fed.us	Silas Little-New Jersey
US-Sne			10.17190/A MF/14 18684	Dennis Baldocchi	PI	University of California, Berkeley	Baldocchi@berkeley.edu	Sherman Island Restored Wetland
US-Srr			10.17190/A MF/14 18685	Brian Bergamaschi	PI	USGS	bbergama@usgs.gov	Suisun marsh - Rush Ranch
US-Tw2			10.17190/A MF/12 46148	Dennis Baldocchi	PI	University of California, Berkeley	baldocchi@berkeley.edu	Twitchell Corn
US-Tw3			10.17190/A MF/12 46149	Dennis Baldocchi	PI	University of California, Berkeley	baldocchi@berkeley.edu	Twitchell Alfalfa
US-Twt			10.17190/A MF/12 46140	Dennis Baldocchi	PI	University of California, Berkeley	baldocchi@berkeley.edu	Twitchell Island
US-Var			10.17190/A MF/12 45984	Dennis Baldocchi	PI	University of California, Berkeley	Baldocchi@berkeley.edu	Vaira Ranch-Ione
US-WBW			10.17190/A MF/12 46109	Tilden Meyers	PI	NOAA/ARL	Tilden.Meyers@noaa.gov	Walker Branch Watershed
US-WCr			10.17190/A MF/12 46111	Ankur Desai	PI	University of Wisconsin	desai@aos.wisc.edu	Willow Creek
US-xAE				Cove Sturtevant	PI	NEON	csturtevant@battelleecology.org	NEON Klemme Range Research Station (OAES)

US-xDC			10.17190/AMF/1617728	Cove Sturtevant	PI	NEON	csturtevant@battelleecology.org	NEON Dakota Coteau Field School (DCFS)
US-xDL			10.17190/AMF/1579721	Cove Sturtevant	PI	NEON	csturtevant@battelleecology.org	NEON Dead Lake (DELA)
US-xDS				Cove Sturtevant	PI	NEON	csturtevant@battelleecology.org	NEON Disney Wilderness Preserve (DSNY)
US-xJR			10.17190/AMF/1617731	Cove Sturtevant	PI	NEON Program, Battelle	csturtevant@battelleecology.org	NEON Jornada LTER (JORN)
US-xNG			10.17190/AMF/1617732	Cove Sturtevant	PI	NEON	csturtevant@battelleecology.org	NEON Northern Great Plains Research Laboratory (NOGP)
US-xRM			10.17190/AMF/1579723	Cove Sturtevant	PI	NEON	csturtevant@battelleecology.org	NEON Rocky Mountain National Park, CASTNET (RMNP)
US-xSL			10.17190/AMF/1617735	Cove Sturtevant	PI	NEON	csturtevant@battelleecology.org	NEON North Sterling, CO (STER)
US-xST			10.17190/AMF/1617737	Cove Sturtevant	PI	NEON	csturtevant@battelleecology.org	NEON Steigerwaldt Land Services (STEI)
US-xUN			10.17190/AMF/1617741	Cove Sturtevant	PI	NEON	csturtevant@battelleecology.org	NEON University of Notre Dame Environmental Research Center (UNDE)
US-xYE			10.17190/AMF/1617743	Cove Sturtevant	PI	NEON Program, Battelle	csturtevant@battelleecology.org	NEON Yellowstone Northern Range (Frog Rock) (YELL)

Supplementary Table 2. Descriptive statistics of bias ratios and differences for alfalfa (ETr) and grass reference ET (ETo) and the associated variables used in their calculation. Bias ratios are shown for ETo, ETr, wind speed (u2), solar radiation (srad), and vapor pressure (ea), and bias differences are shown for minimum (tmin) and maximum (tmax) air temperatures in degree Celsius. These are grouped across all sites (full CONUS), eastern and western CONUS (based on the 100th meridian), and major climatic regions.

Variable	Group	min	max	median	mean	std
ETo	All Sites	0.77	1.49	1.11	1.11	0.08
ETo	East	0.98	1.33	1.13	1.13	0.06
ETo	West	0.77	1.49	1.09	1.09	0.09
ETo	Arid Steppe (Bsk + Bsh)	0.88	1.31	1.06	1.06	0.08
ETo	Desert (Bwh + Bwk)	0.77	1.3	1.09	1.09	0.1
ETo	Humid Continental (Dfa + Dfb)	0.89	1.26	1.12	1.11	0.06
ETo	Humid Subtropical (Cfa)	0.98	1.33	1.14	1.14	0.07
ETo	Mediterranean (Csa + Csb)	0.95	1.49	1.14	1.15	0.09

u2	All Sites	0.53	2.77	1.11	1.17	0.31
u2	East	0.71	2.44	1.13	1.19	0.29
u2	West	0.53	2.77	1.1	1.16	0.33
u2	Arid Steppe (Bsk + Bsh)	0.56	1.95	1.02	1.07	0.24
u2	Desert (Bwh + Bwk)	0.53	1.53	1.11	1.1	0.21
u2	Humid Continental (Dfa + Dfb)	0.54	2.58	1.04	1.1	0.28
u2	Humid Subtropical (Cfa)	0.82	2.44	1.21	1.28	0.32
u2	Mediterranean (Csa + Csb)	0.79	2.77	1.28	1.36	0.39
ETr	All Sites	0.73	1.66	1.14	1.14	0.11
ETr	East	0.96	1.43	1.17	1.17	0.09
ETr	West	0.73	1.66	1.11	1.11	0.12

ETr	Arid Steppe (Bsk + Bsh)	0.85	1.41	1.07	1.08	0.1
ETr	Desert (Bwh + Bwk)	0.73	1.38	1.11	1.12	0.13
ETr	Humid Continental (Dfa + Dfb)	0.85	1.37	1.15	1.14	0.08
ETr	Humid Subtropical (Cfa)	0.96	1.43	1.17	1.17	0.1
ETr	Mediterranean (Csa + Csb)	0.92	1.66	1.18	1.19	0.12
ea	All Sites	0.43	1.15	0.94	0.93	0.06
ea	East	0.86	1.13	0.95	0.95	0.05
ea	West	0.43	1.15	0.93	0.93	0.07
ea	Arid Steppe (Bsk + Bsh)	0.76	1.15	0.93	0.93	0.06
ea	Desert (Bwh + Bwk)	0.43	1.15	0.86	0.85	0.13

ea	Humid Continental (Dfa + Dfb)	0.78	1.07	0.92	0.92	0.04
ea	Humid Subtropical (Cfa)	0.86	1.13	0.97	0.97	0.04
ea	Mediterranean (Csa + Csb)	0.79	1.13	0.95	0.94	0.06
srad	All Sites	0.93	1.24	1.05	1.05	0.04
srad	East	1.02	1.18	1.07	1.07	0.03
srad	West	0.93	1.24	1.04	1.04	0.04
srad	Arid Steppe (Bsk + Bsh)	0.93	1.24	1.02	1.03	0.04
srad	Desert (Bwh + Bwk)	0.98	1.11	1.02	1.03	0.03
srad	Humid Continental (Dfa + Dfb)	0.94	1.12	1.07	1.06	0.03
srad	Humid Subtropical (Cfa)	1.01	1.18	1.06	1.07	0.03

srad	Mediterranean (Csa + Csb)	0.97	1.22	1.08	1.08	0.04
tmin	All Sites	-2.56	4.55	0.18	0.33	0.91
tmin	East	-1.71	1.61	-0.13	-0.1	0.52
tmin	West	-2.56	4.55	0.5	0.62	1.0
tmin	Arid Steppe (Bsk + Bsh)	-1.79	3.02	0.46	0.54	0.85
tmin	Desert (Bwh + Bwk)	-2.16	4.55	1.59	1.6	1.4
tmin	Humid Continental (Dfa + Dfb)	-1.71	3.0	0.16	0.19	0.7
tmin	Humid Subtropical (Cfa)	-1.46	1.61	-0.28	-0.22	0.51
tmin	Mediterranean (Csa + Csb)	-2.56	4.26	0.54	0.55	0.98
tmax	All Sites	-2.0	2.53	0.27	0.26	0.57

tmax	East	-1.82	2.53	0.36	0.35	0.43
tmax	West	-2.0	2.1	0.2	0.21	0.64
tmax	Arid Steppe (Bsk + Bsh)	-1.61	2.1	0.18	0.19	0.6
tmax	Desert (Bwh + Bwk)	-0.63	1.79	0.39	0.5	0.65
tmax	Humid Continental (Dfa + Dfb)	-2.0	1.44	0.15	0.14	0.45
tmax	Humid Subtropical (Cfa)	-1.82	2.53	0.45	0.44	0.45
tmax	Mediterranean (Csa + Csb)	-1.34	1.85	0.25	0.24	0.71

Supplementary Table 3. Monthly OpenET satellite-based ET error and bias metrics by land cover (non-croplands) for models that rely on gridded ETo. Error metrics are computed versus eddy covariance (EC) ET. Δ-values are defined as ETo-bias-corrected − uncorrected; negative values indicate a reduction due to bias correction. MBE, MAE, RMSE are in mm/month. Left column shows land cover with mean monthly √n-weighted flux tower ET in mm.

Land Cover (mean EC ET)	Model	Slope	MBE	MAE	RMSE	R^2	Δ Slope	Δ MBE	Δ MAE	Δ RMSE	Δ R^2	n Sites	n Paired months
Evergreen Forests (61.5)	Ensemble	1.21	14.27	23.49	28.56	0.62	-0.04	-2.95	-1.66	-1.77	-0.01	13	672
	eeMETRIC	1.15	8.78	25	30.97	0.54	-0.09	-6.12	-2.57	-2.92	-0.01	13	672
	SSEBop	1.22	15.58	26.20	32.07	0.52	-0.09	-6.99	-3.89	-3.81	0	13	672
	Ensemble	0.86	-2.50	18.46	23.49	0.53	-0.04	-1.95	-0.31	-0.55	0	16	593

Grasslands (41.4)	eeMETRIC	0.87	-3.37	19.51	25.34	0.58	-0.10	-4.22	-1.68	-2.17	0.01	16	593
	SSEBop	0.75	-7.93	18.61	23.06	0.56	-0.09	-3.77	-0.32	-0.82	0.02	16	593
Mixed Forests (61.2)	Ensemble	1.19	17.49	19.53	24.58	0.87	-0.06	-5.09	-4.54	-4.56	0	10	225
	eeMETRIC	1.06	6.49	18.41	25.03	0.79	-0.14	-9.36	-5.17	-6.59	0	10	225
	SSEBop	1.22	18.72	21.81	27.49	0.83	-0.15	-11.92	-10.60	-11.06	0.01	10	225
Shrublands (29.9)	Ensemble	1.02	4.88	16.66	20.80	0.44	-0.04	-1.32	-0.76	-0.86	0	24	702
	eeMETRIC	0.95	1.86	21.18	26.21	0.32	-0.12	-4.02	-2.73	-3.14	0.01	24	702
	SSEBop	0.80	-4.21	14.65	18.33	0.53	-0.10	-3.38	-1.73	-1.96	0.03	24	702
Wetlands (88.0)	Ensemble	1.07	12.71	26.01	31.41	0.76	-0.05	-5.55	-2.38	-2.64	-0.01	7	285
	eeMETRIC	1.13	16.81	32.66	38.36	0.70	-0.18	-16.70	-11.60	-13.07	0.01	7	285
	SSEBop	1.04	7.69	22.79	28.62	0.80	-0.16	-15.05	-8.73	-10.10	0	7	285

Supplementary Discussion 1

A. Computing irrigation fractions at stations

In this study, we calculate the fraction of irrigated agricultural lands (i.e., irrigated croplands) within a 4 km gridMET pixel based on two publicly available irrigation status datasets using the Google Earth Engine (GEE) APIs (Gorelick et al., 2017; Roy et al., 2025). These include IrrMapper (Ketchum et al., 2020; 2023) and the Landsat-based Irrigation Dataset (LANID, Xie et al., 2019; 2021; Martin et al., 2025).

IrrMapper relies on the GEE-based Random Forests model to generate annual maps of irrigated agriculture at 30 m spatial resolution across 11 western U.S. states for the years 1985-2024. It classifies each 30m pixel into four categories (irrigated agriculture, dryland agriculture, uncultivated land, and wetlands) based on an extensive geospatial database, Landsat imagery, and climate and terrain data. The model demonstrates high performance, achieving very high accuracy of 97.8% for binary classification (irrigated vs. non-irrigated) and strong overall accuracy (90.8%) for the four-class distinction, with the producer's accuracies for the irrigated and dryland classes being 98.9% and 96.6%, respectively. Furthermore, IrrMapper shows strong agreement with the USDA NASS Census of Agriculture at both the state (r^2=0.94) and county (r^2=0.9) levels (Ketchum et al., 2020).

LANID provides annual, 30m resolution maps charting the extent of irrigated croplands, pasture, and hay across the CONUS from 1997 to 2020 (Xie et al., 2021; Martin et al., 2025). Developed using a supervised decision tree classification on GEE, the dataset demonstrates a high overall accuracy of over 90% across all years and regions. More specifically, it shows higher accuracy in the eastern U.S. (94.4%) and NKOT (Nebraska, Kansas, Oklahoma, and Texas, 96.6%) than the 11 western states (92.8%). It also achieves a per-pixel change detection accuracy of 81% and shows strong agreement with USDA-NASS census data at state and county levels. In addition to the annual irrigation maps, LANID includes derivative products on irrigation frequency and trends and provides a crucial ground reference dataset for the eastern U.S., where such data has historically been lacking.

We used both IrrMapper and LANID to assess the effects of irrigated croplands on summertime (June, July, August or JJA) bias ratios and difference distributions, ensuring consistency in our results across these two major irrigation status datasets. The irrigation fraction classes (low, medium, high) represented in percentages in Supplementary Discussion Figure (SDF) 1 are based on manually selected low and high thresholds of 25% and 75%, respectively. We also attributed the stations as irrigated (irrigation fraction > 0) and non-irrigated (irrigation fraction = 0). The irrigation fractions for

each station were calculated by dividing the total 30m irrigated cropland area (from IrrMapper and LANID) within a 1500m buffer surrounding that station (Allen & Brockway, 1983; Allen et al., 1983; Huntington & Allen, 2009). Moreover, the irrigation fraction for each station is a composite value, calculated across all years for which data were available. For a station's specific period of record, we determine its most frequent classification from both the IrrMapper and LANID datasets, which is either '0' (non-irrigated) or '1' (irrigated). We then merge these irrigation fractions (ranging from 0 to 1) to create a single, unified dataset for our analysis. In the 11 western states, we prioritize data from IrrMapper because it has demonstrated higher accuracy in that region (Xie et al., 2021). For any given station in the West, if an IrrMapper fraction is available, we use that value; otherwise, we default to the fraction from LANID. For all stations outside of IrrMapper's spatial domain, the LANID fraction is used by default.

B. Influence of irrigation fraction on the gridMET bias ratios and differences

In Supplementary Discussion Figure 1, for a given variable (e.g., ETo), the summertime (JJA) bias ratios are calculated by dividing the gridMET value by the station value, whereas for the temperature variables, the bias difference is defined as the gridMET value minus the station value. Thus, gridMET is biased high (overestimated) when the ratio exceeds 1 or the difference is positive, unbiased if these equal 1 or 0, and biased low (underestimated) otherwise.

Our analysis using IrrMapper and LANID-derived irrigation fractions showed that ETo generally increase with decreasing irrigation fraction, particularly when considering the median (SDF 1a). We also observe increase in ETo bias when the stations are grouped by the irrigated (irrigation fraction > 0) and non-irrigated (irrigation fraction = 0) classes (SDF 1b). Stations located in low irrigated agricultural areas (i.e., irrigation fraction < 25%; SDF 1a) and non-irrigated agricultural areas (SDF 1b) displayed larger bias partially due to localized irrigation-induced humidity increases and associated cooling effects, which are not adequately captured by coarse-resolution reanalysis data. More significantly, wind speed overestimation is particularly pronounced when irrigated fraction is low and in non-irrigated areas, leading to a higher positive ETo bias. This may be because the influence of rough surface on wind speed cannot be captured by the model when the irrigation fraction is small. Conversely, stations located in regions with high irrigation fractions (> 75%) exhibited lower positive biases in ETo because the influence of irrigated agricultural fields on the regional climate is substantial enough to be captured by the reanalysis data. We also observe similar results for ETr as shown in SDF 1a and b. These results confirm that irrigation and surface roughness strongly influences local atmospheric conditions and wind speed, particularly vapor pressure and air temperature, at a scale below the resolution of gridMET data.

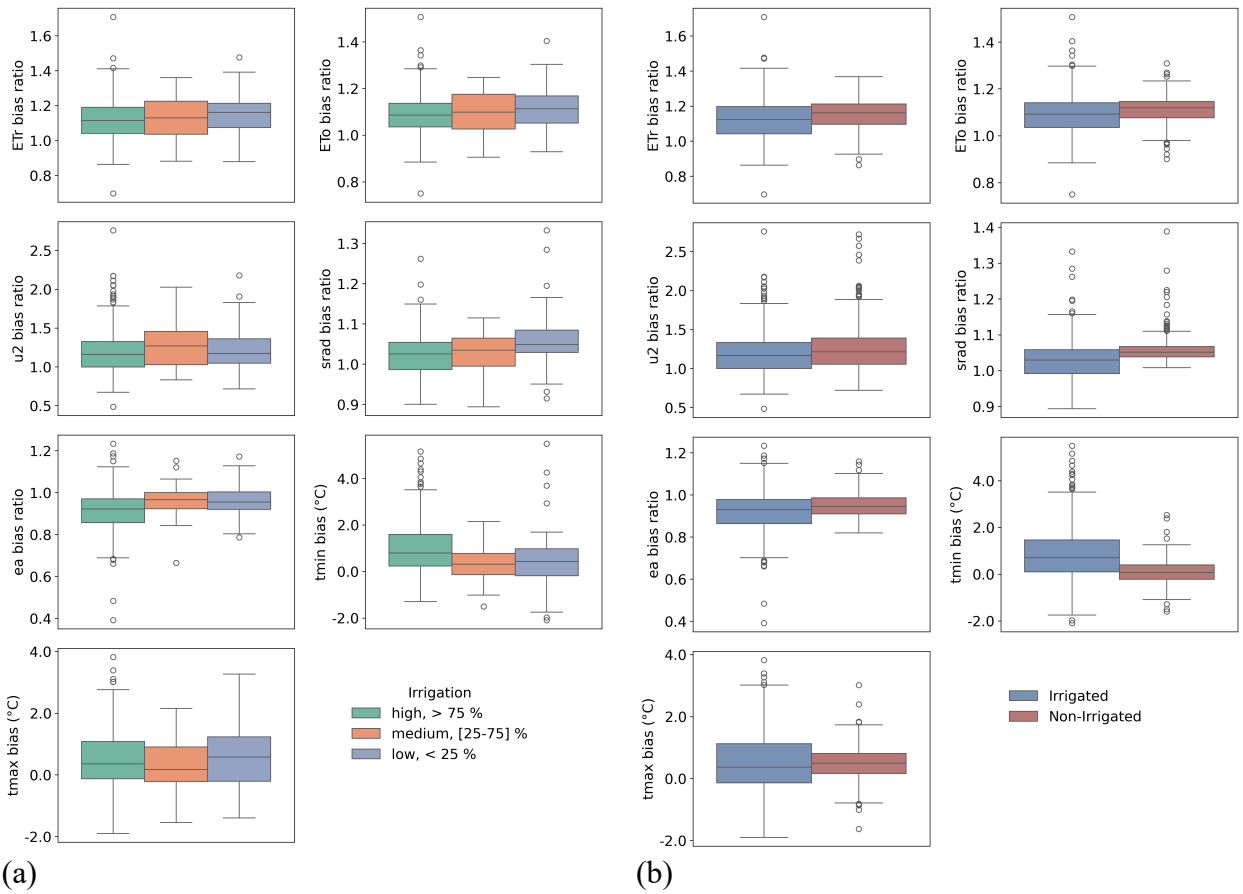

1479 **Supplementary Discussion Figure 1.** Boxplots showing the summertime (JJA) bias ratio (gridMET
1480 value divided by station value) of the alfalfa reference ET (ETr), grass reference ET (ETo), wind speed
1481 (u2), shortwave radiation (srad), vapor pressure (ea), and bias differences (gridMET value – station
1482 value) of the minimum air temperature (tmin) and maximum air temperature (tmax). The three
1483 irrigation fraction classes (low, medium, high) in (a) are based on manually selected low and high
1484 thresholds of 25% and 75%, respectively. In (b), we only show the distributions based on irrigated
1485 (irrigation fraction > 0) and non-irrigated (irrigation fraction = 0) stations. The irrigation fractions are
1486 derived from IrrMapper and LANID using the method described in Section A.

1487 **References**

1488 Allen, R. G., & Brockway, C. E. (1983). *Estimating Consumptive Irrigation Requirements for Crops in*
1489 *Idaho.* RESEARCH TECHNICAL COMPLETION REPORT, Idaho Water and Energy Resources
1490 Research Institute, University of Idaho, Moscow, Idaho. https://idwr.idaho.gov/wp-
1491 content/uploads/sites/2/publications/1983-MISC-Est-Consumptive-Use-08-1983.pdf

1492 Allen, R. G., Brockway, C. E., and Wright, J. L. 1983. Weather station siting and consumptive use
1493 estimates. *J. Water Resour. Ping, and Mgmt. Div.,* ASCE 109 (2): 134-146.

1494 Gorelick, N., Hancher, M., Dixon, M., Ilyushchenko, S., Thau, D., & Moore, R. (2017). Google Earth
1495 Engine: Planetary-scale geospatial analysis for everyone. *Remote Sensing of Environment*, *202*,
1496 18–27. https://doi.org/10.1016/j.rse.2017.06.031

1497 Huntington, J., & Allen, R. G. (2009). Evapotranspiration and Net Irrigation Water Requirements for
1498 Nevada. *World Environmental and Water Resources Congress 2009*, 1–15.
1499 https://doi.org/10.1061/41036(342)420

Huntington, J. L., Hegewisch, K. C., Daudert, B., Morton, C. G., Abatzoglou, J. T., McEvoy, D. J., & Erickson, T. (2017). Climate Engine: Cloud Computing and Visualization of Climate and Remote Sensing Data for Advanced Natural Resource Monitoring and Process Understanding. *Bulletin of the American Meteorological Society*, 98(11), 2397-2410. https://doi.org/10.1175/BAMS-D-15-00324.1

Ketchum, D., Hoylman, Z. H., Huntington, J., Brinkerhoff, D., & Jencso, K. G. (2023). Irrigation intensification impacts sustainability of streamflow in the Western United States. *Communications Earth & Environment*, *4*(1), 479. https://doi.org/10.1038/s43247-023-01152-2

Ketchum, D., Jencso, K., Maneta, M. P., Melton, F., Jones, M. O., & Huntington, J. (2020). IrrMapper: A Machine Learning Approach for High Resolution Mapping of Irrigated Agriculture Across the Western U.S. *Remote Sensing*, *12*(14), 2328. https://doi.org/10.3390/rs12142328

Martin, D. J., Niswonger, R. G., Regan, R. S., Huntington, J. L., Ott, T., Morton, C., Senay, G. B., Friedrichs, M., Melton, F. S., Haynes, J., Henson, W., Read, A., Xie, Y., Lark, T., & Rush, M. (2025). Estimating irrigation consumptive use for the conterminous United States: coupling satellite-sourced estimates of actual evapotranspiration with a national hydrologic model. *Journal of Hydrology*, *662*, 133909. https://doi.org/10.1016/j.jhydrol.2025.133909

Roy, S., Jensen, E., Majumdar, S., & Saah, A. (2025). *samapriya/awesome-gee-community-datasets: Community Catalog (3.8.0)*. https://doi.org/10.5281/zenodo.14042069

Xie, Y., Gibbs, H. K., & Lark, T. J. (2021). Landsat-based Irrigation Dataset (LANID): 30 m resolution maps of irrigation distribution, frequency, and change for the US, 1997–2017. *Earth System Science Data*, *13*(12), 5689–5710. https://doi.org/10.5194/essd-13-5689-2021

Xie, Y., Lark, T. J., Brown, J. F., & Gibbs, H. K. (2019). Mapping irrigated cropland extent across the conterminous United States at 30 m resolution using a semi-automatic training approach on Google Earth Engine. *ISPRS Journal of Photogrammetry and Remote Sensing*, *155*, 136–149. https://doi.org/10.1016/j.isprsjprs.2019.07.005